Error Estimation and Adaptivity in Strain Localisation Problems with Softening Materials

M. Arroyo
P. Díez
A. Huerta

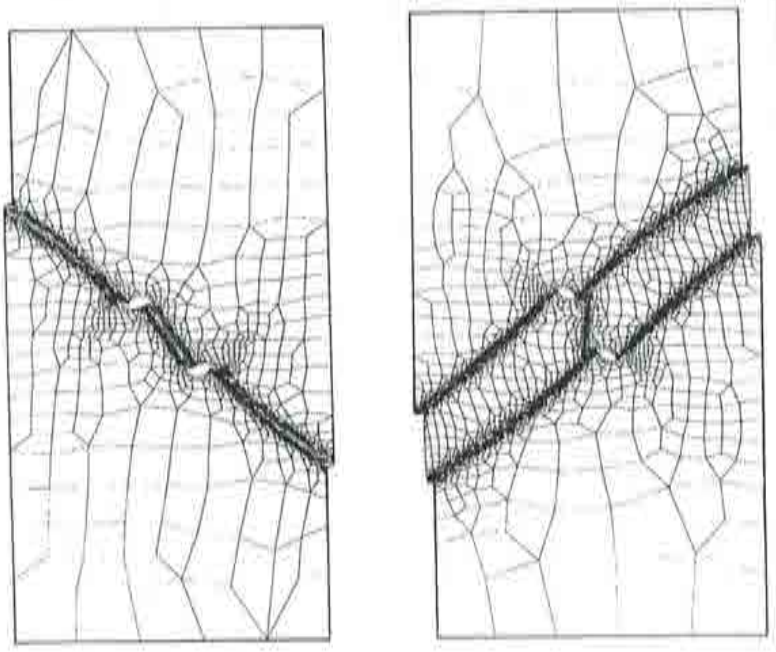

Monograph CIMNE Nº 40, October 1997

Error Estimation and Adaptivity in Stain Localisation Problems with Softening Materials

M. Arroyo
P. Díez
A. Huerta

E.T.S. d'Enginyers de Camins, Canals i Ports de Barcelona
Universitat Politècnica de Catalunya

Monograph CIMNE Nº 40, October 1997

International Center for Numerical Methods in Engineering
Gran Capitán s/n, 08034 Barcelona, Spain

The cover designed by: Jordi Pallí

First published, May 1997

Edited by:
International Center for Numerical Methods in Engineering
C/ Gran Capitán, s/n
08034 Barcelona, Spain

ISBN: 84-89925-05-4
Deposito Legal: B-45288-97

Summary

The study and prediction of failure is one of the most challenging issues of mechanical and structural engineering. In this context, an accurate analysis of strain localisation, which typically triggers failure in many softening materials such as steel or concrete, is of great interest. The classical limit-state methods used to study localisation phenomena are insufficient, and the finite element method appears as a proper analysis tool.

Unfortunately, the numerical simulation of strain localisation in continuum mechanics has to face two important difficulties: the need of a mathematically consistent constitutive model on one side, and of a cost-effective computational strategy capable of capturing the multi-scale nature of localisation problems on the other side. Several formulations have appeared to overcome the first challenge, usually known as regularisation techniques or localisation limiters. On the other hand, adaptivity appears as the natural solution to the computational difficulty.

In the present work, an adaptive remeshing procedure based on a residual type error estimator is presented in the context of quasi-static localisation problems with softening materials. Two well-known localisation limiters have been used: rate dependence has been used to regularise J_2 softening plasticity (via Perzyna viscoplasticity) presenting shear band localisation, and the Mazars damage model with nonlocal regularisation has been applied to simulate fracture localisation. These constitutive models simulate steel and concrete respectively.

Numerical examples show the good performance of the presented procedure, that captures accurately and cost-effectively the micro-scale of strain localisation problems. Furthermore, this error estimator driven adaptive procedure constitutes an objective alternative to the usual approaches that are based on error indicators.

Several topics of interest are also dealt with throughout the work, such as the analysis of the shear band width in quasi-static two-dimensional problems with Perzyna viscoplasticity, the influence of pollution errors in the adaptive process, or the use of error estimation analysis to deduce or test error indicators.

Contents

Chapter 1

INTRODUCTION

1.1 Motivation

The study and prediction of failure is one of the most challenging issues of mechanical and structural engineering. While the linear analysis of solids and structures is well-known, the nonlinear response in advanced stages, which is of great practical interest, presents important difficulties. In particular, certain materials exhibit a softening behaviour, that is a negative slope in the experimentally measured load-displacement curve, when they are brought to advanced inelastic stages, and show a very particular failure mode: strain localisation (see [5], [6], [24], [16], [33], [30]). In these materials, failure is triggered by a very intense deformation occurring in a small part of the solid, while the rest of the solid remains almost in the elastic regime. In fact, strain softening is neither necessary nor sufficient to obtain strain localisation; for instance, localisation can occur as a consequence of a non-associative flow rule (see [25]). Despite this, softening and strain localisation are terms very often related in the literature, as the references given above show (see also [26]).

Two different types of strain localisation can be distinguished, mode-I and mode-II localisation (see [30]). Mode-I corresponds to fractures (high tensile strains localised in a narrow region), that brittle materials such as concrete and rocks present when brought to failure. Mode-II localisation appears when the frictional properties of the material are more critical than the cohesive ones, and is commonly known as shear banding, since high shear strains are mobilised in a narrow band. This localisation mode is typical of metals, soils and polymers.

Despite the prediction of localisation phenomena encountered with such softening materials is extremely important in failure analysis, accurate calculations are rarely found in practical engineering applications. Indeed, the classical limit-state theory does not predict the localisation pattern and only provides bounds of the ultimate carrying load. In addition, this theory does not supply information about the deformations reached in failure. Thus, numerical methods, and in particular the Finite Element Method, seem an appropriate tool to study accurately the inception of localisation and the post-localisation stages leading to failure.

The numerical simulation of strain localisation in continuum mechanics has to face two important difficulties ([9], [24], [19]). The first one is of theoretical nature, and is related to the need of a mathematically consistent constitutive model; when classical rate independent local models are used, the governing equations change of type at the inception of localisation in the localised region, and consequently do not have proper boundary conditions. Thus, the mathematical problem becomes ill-posed. This unproper constitutive modelling leads to unrealistic results (failure takes place without energy dissipation) and has severe numerical consequences: the numerical solution is pathologically mesh dependent. This difficulty is usually overcome using the so-called regularisation techniques, that restore the well-posedness of the problem introducing an internal length into the equations.

The second important difficulty that arises in the numerical simulation of strain localisation stems from the fact that these problems have two scales: the localised region (microscale) is typically very narrow in comparison to the whole body dimensions (macroscale), and very large variations of the material variables take place in this small zone. Therefore, the localised zone requires a very rich discretisation in order to describe properly the phenomenon and the deformation field. Unfortunately, since the localisation shape and structure are not known a priori, a prohibitive computational effort is needed to capture the microscale using a uniform fine mesh. Thus, an efficient computational strategy is needed in order to capture accurately the microscale of the problem with cost-effectiveness. In this context, adaptivity appears as the natural solution.

1.2 State of the art

According to what has been said in the previous paragraphs, the two main challenges of numerical simulation of strain localisation are

- A mathematically consistent constitutive model, in agreement with the mechanical behaviour (strain softening)
- A cost-effective computational strategy capturing the microscale of the localisation problem

The first subject has been widely studied, and many references dealing with regularisation techniques can be found. On the contrary, less work has been done on the second one, for which adaptivity seems to be the most natural and encouraging solution.

Regularisation techniques

In the study of localisation in solids, different approaches have been devised to overcome the difficulties encountered in its analysis. One possible approach is to consider the limit problem, and consequently, accept discontinuities of the displacement field across some surfaces (strong discontinuity approach). As a matter of fact, discontinuities, understood in a distributional sense, emanate from classical perfect plasticity (see [29]). Another possible

approach is to regularise the problem precluding any discontinuity in the displacement field. The present work focuses on the latter approach.

Many regularisation techniques or localisation limiters have been proposed to eliminate the undesirable mesh dependence of the numerical solution when classical softening rate independent local plasticity is used (see [10] for a review). Some ad-hoc solutions take material parameters, such as the softening modulus or the energy dissipation, dependent on the element size. Nevertheless, most of the localisation limiters act at the constitutive level, and can be seen as enhanced or enriched continua. They introduce explicitly or implicitly an internal length scale into the problem. These techniques keep the type of the governing equations unchanged (hyperbolic in the transient case and elliptic in the static case) and the numerical solutions suffer no longer from mesh sensitivity. The internal length scale and its relation with the localisation zone dimensions has been widely studied and is an important feature of strain localisation problems.

One possibility to obtain a well-posed problem is the use of Cosserat micropolar continuum, which adds degrees of freedom corresponding to rotations (see [30]). Models including spacial derivatives of the state variables, such as the gradient of the internal variable in the yield function, or introducing additional higher order terms in the strain expression (see [13]) also lead to well-posed problems and mesh objective numerical results.

In particular, the present work focuses on viscoplastic regularisation (see [13], [16], [30]), used in combination with J_2 plasticity (leading to Mode-II localisation). The constitutive model introduces a material rate dependence, which implicitly defines an internal length scale. This localisation limiter has been successfully used to regularise transient problems ([16], [6], [33], [30], [9]), and quasi-static problems (see [16], [36], [5]). The internal length scale and the shear band width in transient problems have been widely studied, whereas little is known about the scaling of the shear band in quasi-static two dimensional problems ([16] and [5] analyse the shear band width only in one dimensional problems).

Nonlocal regularisation (see [27], [23]) is also treated in this work, combined with Mazars damage model, which simulates brittle materials presenting Mode-I localisation. This nonlocal formulation consists on averaging certain state variables in a neighbourhood of every point.

Adaptivity applied to strain localisation problems

In the adaptive procedures, the discretisation is successively adapted to the solution according to some information about the error, in the aim of reaching an accurate approximation with an optimal computational cost. This procedures are nowadays considered to be almost unavoidable in any complete Finite Element analysis.

Whereas adaptivity has been widely developed in linear elasticity and some nonlinear problems, less experience is available on adaptivity applied to strain localisation ([19]). Nevertheless, several references on this topic have appeared in the recent years: remeshing procedures are used in [39], [20] and [37] in the context of static strain localisation problems, while [6], [9] and [19] apply refinement procedures to transient problems. In [24] an ALE formulation, which can be seen as a remeshing tool, is used in transient problems.

However, none of these authors use adaptivity based on a posteriori error estimation; they all use error indicators, which are cheap but often lack theoretical foundations and are based on heuristic assumptions. As a matter of fact, most of the existing standard error estimators can only be used in elliptic problems, and the transient problem is hyperbolic. On the other hand, in [39], [20] and [37], where static problems are treated, no regularisation technique has been used, and consequently, the governing equations lose the ellipticity in certain zones at the inception of localisation, and a standard error estimator cannot be used either. Apart from this, the fact that some popular error estimators have a weak theoretical background in nonlinear problems can also explain the lack of experience in error estimation analysis for localisation problems.

1.3 Scope and objectives

In this study, attention is restricted to adaptive remeshing based on error estimation in localisation problems. That is, the goal is to provide an objective alternative to the usual adaptive procedures based on error indicators. Since the error estimation requires elliptic problems, the work focuses on quasi-static regularised problems: Perzyna softening viscoplasticity is used to model a metal presenting shear bands, and Mazars nonlocal model to simulate concrete, which is bound to show fractures when brought to failure.

Apart from this general goal, the present work has other partial objectives summarised below

- Present a general and efficient residual type error estimator, able to capture pollution errors and applicable to general nonlinear problems
- Study in detail Perzyna viscoplasticity behaviour, and its regularising effect in quasi-static problems, focusing on the shear band width
- Perform adaptivity based on error estimation in problems regularised via Perzyna viscoplasticity, presenting a computationally efficient approach that answers objectively to the basic issues of adaptivity
- Investigate the influence of considering the pollution errors in the adaptive process
- Present the error estimator driven adaptive procedure as a powerful tool to investigate error indicators
- Illustrate the great benefits and the suitability of the adaptive procedure in complex localisation problems, capturing the microscale with cost-effectiveness
- Perform adaptivity based on error estimation in Mode-I localisation problems using Mazars damage model and nonlocal regularisation

1.4 Outline of the work

Chapter 2 presents a general and effective residual type error estimator by Díez (1996) (see [8]), in the context of mechanical problems. This a posteriori error estimator leans on a solid mathematical background, captures the pollution errors and is applicable to nonlinear problems. This chapter pays a special attention to the computational aspects involved in the implementation of the estimator.

In chapter 3, viscoplastic regularisation using Perzyna model is analysed in problems presenting shear banding, and mesh objective numerical results are obtained. The inception of localisation and the post-localisation stages are also studied in detail. Finally, the influence of several parameters on the shear band width is investigated.

In chapter 4, once the adaptive procedure is presented, adaptive remeshing based on error estimation is performed in problems regularised via Perzyna viscoplasticity. Several numerical examples show that this procedure answers objectively to the fundamental questions of where to put the elements and how many elements are needed to obtain accurate numerical solutions. Furthermore, this objective approach can be very useful to deduce or test error indicators, that constitute a cheap, but often not rigorous, alternative to error estimation. The influence of the pollution errors on the adaptive process is also investigated. Finally, more complex and realistic examples are presented, showing that the adaptive procedure is a computational strategy that captures accurately and cost-effectively the microscale of the problem and the a priori unknown shear band pattern. As a matter of fact, a non-adaptive Finite Element analysis of these examples providing good accuracy requires an enormous computational effort, becoming prohibitive in practical engineering calculations.

The concluding remarks are presented in chapter 5, as well as the future developments.

In appendix A, Perzyna constitutive model is formulated and its qualitative behaviour studied in detail. Some relevant aspects, like its limit behaviour and the viscous overstress that appear, are also dealt with. The implementation of the model is validated with some simple tests.

Finally, appendix B illustrates the use of the adaptive procedure to localisation problems with nonlocal regularisation. Mazars nonlocal damage model is presented, and adaptivity is performed in a fracture localisation problem.

Chapter 2

ERROR ESTIMATION AND ADAPTIVITY

This chapter reviews error estimation, linked to adaptative procedures, in the aim of applying these techniques to nonlinear problems in chapter 4. A detailed discussion on error estimation in general or remeshing strategies is beyond the scope of this chapter. Nevertheless, the error estimator employed in this work is described in quite detail, including some computational aspects of interest.

In section 2.1, error estimation in Finite Element analysis is introduced in the context of adaptative procedures. These techniques are outlined, focusing on a particular remeshing strategy, h remeshing.

Then, in section 2.2, the concept of error estimator is defined and the most important error estimator families are presented, reviewing their principal characteristics.

Section 2.3 presents an efficient and general residual type error estimator, in the context of mechanical linear problems. This estimator avoids the calculation of flux jumps, which is the main drawback of usual residual type estimators. The generalisation to the nonlinear case occupies section 2.4.

Finally, the pollution errors estimation and the computational aspects of the estimator are developed in sections 2.5 and 2.6.

2.1 Introduction

Motivation

The practical problems encountered in engineering are frequently related with the calculation of certain magnitudes of interest in real situations. To achieve these calculations, three conceptual steps can be distinguished. Firstly the real situation is identified to a physical model. This physical model leads to a mathematical problem that needs to be solved, exactly if possible, and approximately in most cases.

Obviously, this process introduces errors in every step, ranging from our deficient perception of reality to the simplifications made to formulate the mathematical problem. Avoiding these errors seems difficult, and, what is more, unreasonable when the marginal cost of accuracy becomes too high. Nevertheless, a knowledge of the errors we are assuming is desirable, and even necessary. In the present work, only the errors made solving the mathematical problem are treated.

In civil engineering, the mathematical problem that appears is very often a Partial Differential Equation, which can be solved analytically only in very particular situations. Nowadays, the most popular method to approximate the solution of these problems is the finite element method.

Using a discretisation of the domain, the finite element method transforms the differential equations into an algebraic system of equations, introducing a first source of errors into the solution, the discretisation errors. The accuracy of the discretisation is ruled by both the geometry of the mesh (element size) and the degree of the interpolation. This system of equations is then solved numerically. This step brings new errors, such as round-off errors. Nevertheless, these errors are negligible in front of the discretisation errors.

In the recent years, much work has been done in order to develop procedures that control the accuracy of the finite element method, by means of setting the discretisation errors to a prescribed level with a reasonable cost. These techniques are known as adaptative procedures, and error estimation is an essential part of them.

Adaptative procedures based on error estimation

As it has been said, the finite element method approximates a continuous problem into a discrete one. The process of discretisation leads to a problem which is easy to solve, but introduces discretisation errors. The goal of adaptative procedures is to obtain a solution with a prescribed accuracy, using an optimal discretisation to minimize the computational cost.

So, for a given discretisation, an approximate solution is found. The next step is to estimate the error using an a posteriori error estimator. If the error is acceptable, the current approximation is kept. On the contrary, if it is not, the information about the error is used to build a new discretisation adapted to the solution in an optimal manner, according to a remeshing strategy. This process is carried out until an acceptable solution is obtained.

Remeshing strategies are based on a priori error estimators. A general expression for a priori error estimators is

$$\|e\| \leq Ch^m, \tag{2.1}$$

where $\|e\|$ is a measure of the error, h the characteristic size of the mesh, C an unknown constant and m is directly related to the degree of the interpolation of the approximation p. This expression is obtained from the theoretical analysis of the method, and is useless to estimate the error as long as C is not known. However, it makes clear that the error can be reduced either reducing the element size h, or increasing the degree of the interpolation p.

One possibility is then to adapt the element size over the domain according to the error estimation. The element size is reduced where it is needed, and increased where the actual accuracy is higher than the prescribed one. Two different ways of remeshing based on the element size can be distinguished, h remeshing and r remeshing. In h remeshing, a brand new mesh is generated once the error has been estimated, and a new calculation is carried out on the new discretisation. If a powerful mesh generator is available, this remeshing is very simple. On the other hand, r remeshing maintains the topology of the mesh, and only changes the position of the nodes to modify the element size over the domain. Therefore, the information related with the connectivity of the mesh is identical in every step of the adaptative process. However, since the number of degrees of freedom does not change, it is not possible to guarantee a prescribed accuracy in all the cases.

Another possibility of changing the discretisation is to use different interpolation functions. Then, the mesh geometry is kept and the new degrees of freedom correspond to higher degree polynomials used to interpolate. This is known as p remeshing, and it is usually combined with h remeshing. However, the implementation of this kind of remeshing is difficult and requires the use of hierarchic interpolation.

h remeshing based on error estimation

In this work, h remeshing is used. It lies in three basic tools, a mesh generator, a standard finite element code and an error estimator. In the present work, the quadrilateral mesh generator developed by Sarrate (1996) (see [28]) is used. This mesh generator supplies excellent unstructured meshes, both ensuring the prescribed element size and the regularity of the elements. The finite element code used is CASTEM 2000, an object oriented code especially well suited to develop new procedures. Finally, the error estimator employed is a residual type estimator by Díez (1996) (see [8]), described in the following sections. The remeshing process based on error estimation is described in detail below.

Basically, the remeshing procedure answers in an objective way the questions of where to remesh, and how much remeshing is needed. Firstly, the error of the solution in a given discretisation is estimated. Then, the adaptive procedure requires a remeshing criterion in order to generate the input for the mesh generator. The error estimator furnishes local measures of the error in each element, that is, $\|e\|_k$ for $k = 1, \ldots$ This set of numbers describes the spatial distribution of the error. The input of a mesh generator is a distribution of desired element size in the computational domain. Generally, this is described by the desired element size in each element of the current mesh, that is, $\hat{h}_k$ for $k = 1, \ldots$ Thus, a remeshing criterion is required to translate $\|e\|_k$ into $\hat{h}_k$.

Different remeshing criteria have been defined (see [34], [18], [14], [8]) leading to quite different optimal meshes. This is because the underlying optimality criteria are different. In fact, all these remeshing criteria tend to equidistribute the error in some sense (absolute error, relative error, specific error). The choice of the error function that has to be uniform is related with the underlying optimality criterion.

Figure 2.1 provides illustration of the adaptive procedure used here. The crucial role of the error estimator in the procedure is evident from the figure.

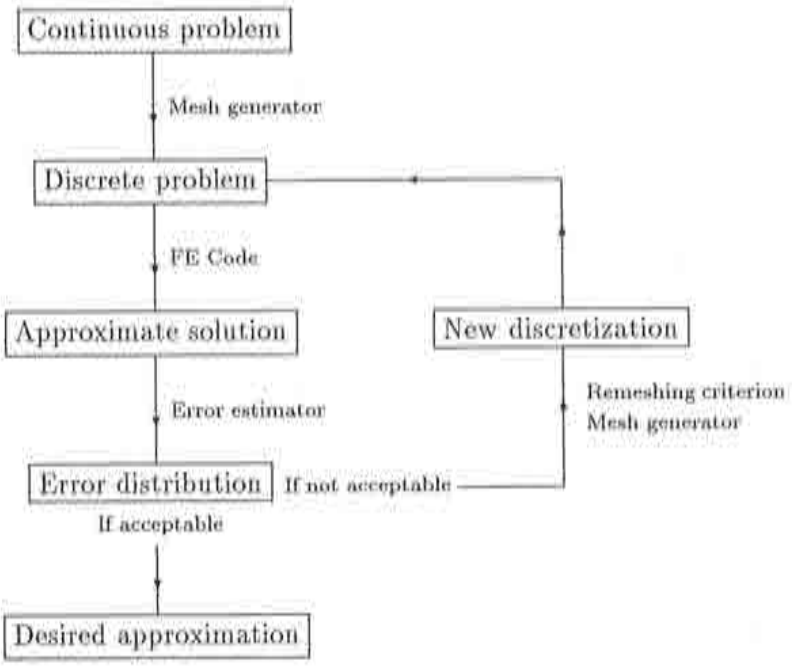

Figure 2.1: Adaptive procedure based on error estimation

2.2 Classification of error estimators

As it has been shown, the error estimation is a key feature in the adaptative procedures. First of all, what is meant by an error estimation should be clear. There is a first distinction between a priori estimators and a posteriori estimators. The former are derived from theoretical analysis of the finite element method to obtain the convergence results of the method, but are useless to estimate the error of a given approximation (see equation 2.1). This work deals with the latter, which have the practical applications described in the previous section.

On the other hand, there is another distinction between the error estimators and the error indicators. While the mathematicians consider that an error estimator approximating a certain norm of the error $\|e\|$ should behave like a norm equivalent to $\|\cdot\|$, engineers have a wider definition of error estimators. They talk of error indicators when a qualitative information of the error is given, and of error estimators when a particular norm of the error is approximated.

The error indicators usually involve straightforward computations. Therefore, they constitute a cheap alternative to error estimation in an adaptative remeshing process, where several estimations are usually needed. However, error indicators usually lean on heuristic

assumptions, and can lead to bad meshes. In addition, they supply information about where the elements must be, but not how many elements are needed, in other words, qualitative information.

The following sections deal with a posteriori error estimators in the engineering sense. Before the main two families of error estimators, the flux projection estimators (see [35] and [38]) and the residual type estimators (see [2], [1], [3]) are presented, it is worth enunciating the desirable properties of an error estimator, in order to judge them fairly. These properties can be summarised as follows

- Good performance, so that the estimated error approximates well the exact error.
- Simplicity, in the sense of a natural integration in a standard FE code.
- Theoretical basis and a solid mathematical background.
- Generality, so that it can be used in a wide range of situations.
- Computational economy.

Flux projection error estimators

These estimators compare the flux of the approximate solution (in mechanics, the discontinuous stress field) with a smoothed flux. It seems obvious that the smoothed solution is better than the original one. Therefore, the error in fluxes can be estimated. This estimator is simple and shows a good performance in many cases.

From the theoretical point of view, the estimator requires the superconvergent properties of certain points that are used as sample points to smooth the solution. Nevertheless, superconvergence is not assured in general, and the estimator lacks theoretical basis in most cases. In addition, the error can only be measured with norms that can be expressed in terms of fluxes. Moreover, in nonlinear problems, even if superconvergent properties are assured, this kind of error estimator does not have theoretical basis.

Thus, flux projection estimators are simple and robust, but apply only in particular cases and often lack of theoretical basis.

Residual type error estimators

These estimators solve local problems in which the residual is a source term. Although the general idea is very simple, the detailed definition of a residual type estimator encounters a major difficulty. The boundary conditions of these local problems need to be approximated from the flux jumps. To do this, elementary equilibrium conditions are imposed. At the end, the estimation becomes an annoying and expensive task. Because of this, these estimators do not perform well and are not very popular in commercial codes, despite their strong theoretical basis and wide generality.

The error estimator by Díez (1996) maintains the theoretical basis and the generality of the estimators of this kind avoiding the approximation of the local boundary conditions

from the flux jumps. An efficient and low-cost estimation results, that can be applied in a wide range of situations, such as nonlinear problems or meshes involving different kinds of elements.

This error estimator is presented in sections 2.3, 2.4 and 2.5 in the environment of mechanical problems, although it can be used for any boundary value elliptic problem. For this reason, the general mathematical formulation is maintained making it easy to generalise the estimator to other kind of problems.

2.3 Error estimation for linear problems

2.3.1 The error equation: a residual problem

The governing equations of the mechanical problem are presented below. It is a second order Partial Differential Equation, and represents the strong form of the problem. Depending on the constitutive model, that is the relation between strains and stresses, and the strain-displacement relation, the problem is linear or not. On the other hand, the problem is elliptic for a wide range of constitutive models, and therefore the error estimation can be used in these cases. The unknown is a displacement field u defined in the domain Ω that verifies

$$\begin{cases} \nabla \cdot \boldsymbol{\sigma}(u) + b = 0 & \text{in } \Omega \\ u = g_d & \text{on } \Gamma_d \\ \boldsymbol{\sigma}(u) \cdot n = g_n & \text{on } \Gamma_n \end{cases} \tag{2.2}$$

where $\boldsymbol{\sigma}(u)$ stands for the stress tensor associated with the displacements u, b is the body force term and g_d and g_n are the prescribed values of Dirichlet and Neumann boundary conditions respectively. In equation 2.2, the stress tensor $\boldsymbol{\sigma}(u)$ plays the role of the flux in a general problem.

By means of the Virtual Work Principle or any other variational principle, a weak form of the problem can be formulated. Thus, the solution to the problem posed in equation 2.2 can also be characterized as the solution of a weak problem. The solution u that has to be approximated lies in a space $\mathcal{V}$ that accounts for the Dirichlet boundary conditions, and verifies the following integral equation

$$a(u, v) = l(v) \text{ for all } v \in \mathcal{V}, \tag{2.3}$$

where the forms $a(\cdot, \cdot)$ and $l(\cdot)$ are defined in $\mathcal{V} \times \mathcal{V}$ and $\mathcal{V}$, respectively, and can be expressed as

$$a(u, v) = \int_\Omega \boldsymbol{\sigma}(u) : \boldsymbol{\varepsilon}(v)\, d\Omega \quad \text{and} \quad l(v) = \int_\Omega b \cdot v\, d\Omega + \int_{\Gamma_n} g_d \cdot v\, d\Gamma. \tag{2.4}$$

In particular, linear elasticity leads to linear self-adjoint elliptic problems, and consequently to bilinear symmetric positive definite forms, hence, scalar products. In this case, $\boldsymbol{\sigma}(\cdot)$ and $\boldsymbol{\varepsilon}(\cdot)$ (see equation 2.4) are linear functions of their arguments.

The Galerkin finite element method provides an approximation u_h to u, lying in a finite-dimensional space $\mathcal{V}_h \subset \mathcal{V}$ and verifying

$$a(u_h, v_h) = l(v_h) \text{ for all } v_h \in \mathcal{V}_h. \tag{2.5}$$

In linear problems, equation 2.5 leads to the linear system of equations

$$\mathbf{K}_h \mathbf{u}_h = \mathbf{f}_h^{\text{ext}}, \tag{2.6}$$

where $\mathbf{K}_h$ is the stiffness matrix, $\mathbf{f}_h^{\text{ext}}$ is the external force term and the unknown $\mathbf{u}_h$ is the vector of nodal displacements of u_h. The matrix $\mathbf{K}_h$ is the discrete version of the form $a(\cdot,\cdot)$ and the vector $\mathbf{f}_h^{\text{ext}}$ discretizes $l(\cdot)$. In linear elasticity, $\mathbf{K}_h$ is a symmetric positive definite matrix, and owing to this, a scalar product in the space $\mathcal{V}_h$.

In more physical terms, equation 2.6 can also be expressed as a balance between internal and external nodal forces

$$\mathbf{f}_h^{\text{int}}(\mathbf{u}_h) = \mathbf{f}_h^{\text{ext}}; \tag{2.7}$$

$\mathbf{f}_h^{\text{int}}(\mathbf{u}_h)$ can be seen as the vector discretization of $a(u_h, \cdot)$ in $\mathcal{V}_h$.

The finite-dimensional space $\mathcal{V}_h$ is generated by a finite element mesh of characteristic size h. If $a(\cdot,\cdot)$ is a scalar product, u_h can be seen as the projection of u on $\mathcal{V}_h$ (following the orthogonality defined by $a(\cdot,\cdot)$). In this case, the error $e := u - u_h$ is orthogonal to $\mathcal{V}_h$. This error can also be caracterised in terms of a weak problem, rearranging equation 2.3 and using the bilinearity of the form $a(\cdot,\cdot)$. Thus, the error e is the element in $\mathcal{V}$ that verifies

$$a(e, v) = l(v) - a(u_h, v) \text{ for all } v \in \mathcal{V}. \tag{2.8}$$

Note that the right hand side of equation 2.8 is a residual term which accounts for the non-verification of equation 2.3.

As previously said, the objective of this error estimator is to provide both a global value of the error and its spatial distribution. So, if an approximation of the error is found in a subspace of $\mathcal{V}$, a norm to measure it must be defined. One of the most popular options is to use the energy norm, induced by the scalar product $a(\cdot,\cdot)$

$$\|e\| := [a(e, e)]^{1/2}. \tag{2.9}$$

This is because $\|\cdot\|$ has a precise physical meaning and can be easily restricted in order to obtain associated local norms. In addition, this norm can be easily computed discretely using the stiffness matix, the matrix of the scalar product, for a certain discretisation. In the following, the restiction of $\|\cdot\|$ to the element Ω_k ($k = 1, 2, \ldots$) of the mesh is denoted by $\|\cdot\|_k$. The value of $\|e\|_k$ in each element must be estimated in order to describe the spatial distribution of e.

2.3.2 The reference error

The error e is the unknown of the residual problem defined by equation 2.8. Of course, it is as difficult to solve this problem as the original one (see equation 2.3). In other words, if

it was possible to obtain the exact error, the exact solution would be found. Therefore, the only attainable goal is to obtain an approximation to e, say $e_{\tilde{h}}$. This approximation to the error can be easily defined from a new approximation to u, say $u_{\tilde{h}}$. Indeed, let $u_{\tilde{h}}$ be a finite element approximation associated with a finer mesh of characteristic size $\tilde{h}$ ($\tilde{h} << h$). Then, $u_{\tilde{h}}$ is much more precise than u_h and, therefore, $e_{\tilde{h}} := u_{\tilde{h}} - u_h$ is a good approximation of e. This is formally shown in [17] as a consequence of the a priori convergence analysis of the finite element method.

In fact, computing $u_{\tilde{h}}$ and then obtaining $e_{\tilde{h}}$ is equivalent to directly solving the error equation 2.8 using the finer mesh. Denoting by $\mathcal{V}_{\tilde{h}}$ the interpolation space associated with this finer mesh, $e_{\tilde{h}}$ is the element of $\mathcal{V}_{\tilde{h}}$ that verifies

$$a(e_{\tilde{h}}, v_{\tilde{h}}) = l(v_{\tilde{h}}) - a(u_h, v_{\tilde{h}}) \text{ for all } v_{\tilde{h}} \in \mathcal{V}_{\tilde{h}}. \tag{2.10}$$

The approximation $e_{\tilde{h}}$ can be taken as a reference error. That is, instead of the original goal of computing e, the goal is switched to approximating $e_{\tilde{h}}$. Therefore, the refined mesh of characteristic size $\tilde{h}$ discretizing the whole domain Ω is denoted as the reference mesh.

Note that, since Galerkin finite elements are used again, solving equation 2.10 is equivalent to projecting the error e on $\mathcal{V}_{\tilde{h}}$. Assuming that the original projection space $\mathcal{V}_h$ is included in the new space $\mathcal{V}_{\tilde{h}}$, it is obvious that to obtain a nonzero approximation to e, the new space must be "bigger" than $\mathcal{V}_h$ (recall that e is orthogonal to $\mathcal{V}_h$). That is, $\mathcal{V}_{\tilde{h}}$ must be associated with a richer interpolation. This new space can be constructed either reducing the mesh size (as it has been presented, $\tilde{h} << h$) or increasing the degree of the interpolation polynomials (p refinement).

Figure 2.2 shows a graphic illustration of the meaning of the reference error and its relation with the residual. A variation of this figure provides a good understanding for the nonlinear case. The left hand side term of equation 2.6 is associated with the internal forces defined in the coarse mesh characterised by h: $\mathbf{f}_h^{\text{int}} = \mathbf{K}_h \mathbf{u}_h$. Internal forces are also defined in the reference mesh: $\mathbf{f}_{\tilde{h}}^{\text{int}} = \mathbf{K}_{\tilde{h}} \mathbf{u}_{\tilde{h}}$. Recall that the right hand side term of equation 2.6 is associated with the external forces: the external force vector discretized in the coarse computational mesh is denoted by $\mathbf{f}_h^{\text{ext}}$ and the equivalent in the finer reference mesh is denoted by $\mathbf{f}_{\tilde{h}}^{\text{ext}}$. Thus, solving the initial problem is equivalent to finding the value of u_h that makes $\mathbf{f}_h^{\text{int}}(u_h) = \mathbf{f}_h^{\text{ext}}$ (intersection of upper sloped line and the lower horizontal line). The reference solution $u_{\tilde{h}}$ is computed in the same fashion. This is represented by the intersection of lower sloped line and upper horizontal line. (Note that the coarse mesh leads to a stiffer problem than the finer one). Figure 2.2 shows that the reference error $e_{\tilde{h}}$ and the residual, defined as

$$\mathbf{r}_{\tilde{h}}(\mathbf{u}_h) := \mathbf{f}_{\tilde{h}}^{\text{int}}(u_h) - \mathbf{f}_{\tilde{h}}^{\text{ext}}, \tag{2.11}$$

are related in terms of the stiffness matrix in the reference mesh, $\mathbf{K}_{\tilde{h}}$. In fact, equation 2.10 leads to the linear system of equations

$$\mathbf{K}_{\tilde{h}} \mathbf{e}_{\tilde{h}} = -\mathbf{r}_{\tilde{h}}(\mathbf{u}_h), \tag{2.12}$$

where $\mathbf{e}_{\tilde{h}}$ is the vector of nodal displacements of the reference error $e_{\tilde{h}}$. This expression shows clearly that the residual can be seen as the internal forces associated to the reference

error

$$\mathbf{f}_h^{\text{int}}(\mathbf{e}_{\bar{h}}) = -\mathbf{r}_{\bar{h}}(\mathbf{u}_h). \tag{2.13}$$

In more general terms, this residual is the column vector resulting from discretizing the residual form $a(u_h, \cdot) - l(\cdot)$ (see equation 2.10) in $\mathcal{V}_{\bar{h}}$.

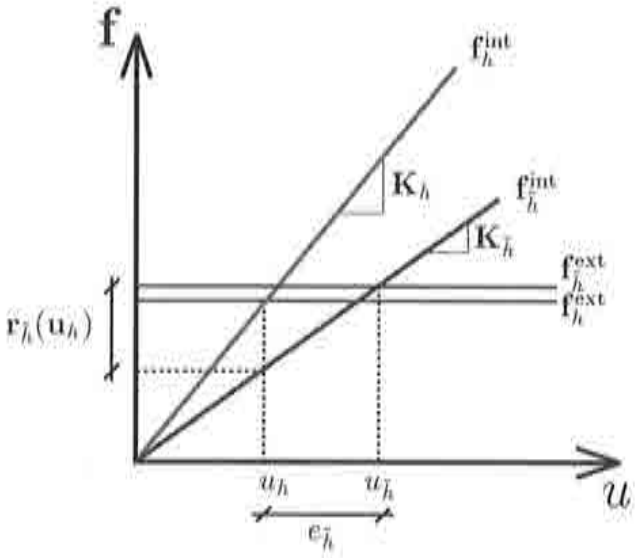

Figure 2.2: Graphic interpretation of reference error in linear problems

Nevertheless, the standard computation of $e_{\bar{h}}$ must be avoided due to its prohibitive computational cost. In effect, the refined mesh generating $\mathcal{V}_{\bar{h}}$ has a number of degrees of freedom much greater than the original mesh and, therefore, the cost of computing $e_{\bar{h}}$ is much larger than the cost of computing u_h.

In the remainder of this section a method for approximating $e_{\bar{h}}$ by low cost local computations is presented. This method is splitted in two phases. First, a simple residual problem is solved inside each element and an interior estimate is obtained. Second, a new family of simple problems is considered and the interior estimate is complemented adding a new contribution. The first phase is called interior estimation and the second one is called patch estimation.

2.3.3 Interior estimation

In order to avoid unaffordable computations, the error estimation must be based on the resolution of local problems. This is standard in residual type error estimators. On the other hand, the set of elements Ω_k is the natural partition of the domain. Thus, it is natural to solve local problems element by element.

Following this rationale, a reference mesh is constructed by the assembly of submeshes discretizing each element. These elementary submeshes are built from a discretization of the reference element mapped into the elements of the actual mesh (see figure 2.3). Proceeding in this way, the original projection space $\mathcal{V}_h$ is included in the space $\mathcal{V}_{\tilde{h}}$ associated to the reference mesh.

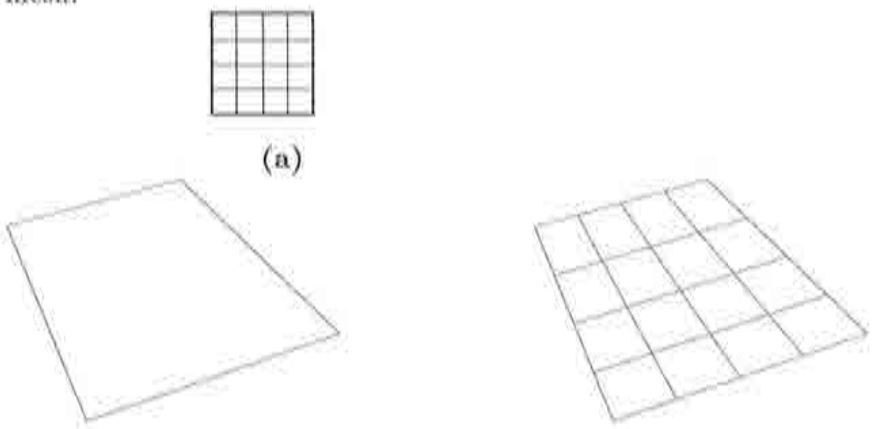

Figure 2.3: **(a)**, reference submesh mapped into **(b)**, an element, to get **(c)**, an elementary submesh

Then, the elementary submeshes can be used to solve the error equation 2.8 on each element Ω_k of the original mesh. However, the solution of such problems requires proper boundary conditions for the error. Most of residual type error estimators (see [3], [1], [12]), solve equation 2.8 prescribing the flux around each element Ω_k, that is, solving pure Neumann problems. The prescribed values of error fluxes are found splitting the jump of the fluxes of u_h across the element edges. The computation of the flux jumps across the edges is expensive. The splitting procedure usually balances the fluxes around the element and, therefore, is generally involved.

In this work, the elementary problems are solved in a straightforward manner imposing homogeneous Dirichlet conditions for the error, along the boundary of each element Ω_k (see [8]). That is, equation 2.8 is solved at element level and the error is prescribed to zero in all the boundary nodes of the elementary submesh. This is the simplest choice for these local boundary conditions. This discrete local problem leads to a system of equations

$$\mathbf{K}_k^e \, \epsilon_k = -\mathbf{r}_k^e, \tag{2.14}$$

where $\mathbf{K}_k^e$ is the stiffness matrix resulting of discretizing $a(\cdot,\cdot)$ in the elementary submesh of Ω_k, and $\mathbf{r}_k^e$ the the residual $\mathbf{r}_{\tilde{h}}(\mathbf{u}_h)$ (see equation 2.13) restricted to the elementary submesh. The vector of nodal displacements ϵ_k represents a function ε_k interpolated in the elementary submesh discretizing Ω_k. The function ε_k is taken as an approximation to $e_{\tilde{h}}$ inside Ω_k but

has been forced to vanish along the boundary of Ω_k. The local energy norm of the interior estimate ε_k can be directly computed as

$$\|\varepsilon_k\|^2 = a(\varepsilon_k, \varepsilon_k) = \boldsymbol{\varepsilon}_k^T \mathbf{K}_k^e \boldsymbol{\varepsilon}_k = -\boldsymbol{\varepsilon}_k^T \mathbf{r}_k^e. \tag{2.15}$$

Note that the squared norm of the error is simply computed as the scalar product of two vectors, the estimated displacement error and the force residual. Moreover, since ε_k has its support in Ω_k, local and global norms are equal: $\|\varepsilon_k\| = \|\varepsilon_k\|_k$.

Once the elementary problems are solved, the local interior estimates can be assembled to build up a global estimate ε taking values in the whole domain Ω,

$$\varepsilon = \sum_k \varepsilon_k. \tag{2.16}$$

Note that the interior estimates associated with different elements are orthogonal since they have disjoint supports. Therefore, Pythagoras theorem holds and the norm of ε can be easily computed as

$$\|\varepsilon\|^2 = \sum_k \|\varepsilon_k\|^2. \tag{2.17}$$

Both local and global interior estimates are projections of e (and $e_{\tilde{h}}$) on a subspace included in $\mathcal{V}_{\tilde{h}}$. The inclusion in $\mathcal{V}_{\tilde{h}}$ is verified because the element boundary degrees of freedom are ignored, according to the homogeneous Dirichlet boundary condition, which also preserves global continuity. Consequently the norms of the interior estimates are lower bounds of the actual and reference errors:

$$\|\varepsilon\| \leq \|e_{\tilde{h}}\| \leq \|e\| \quad \text{and} \quad \|\varepsilon_k\|_k = \|\varepsilon\|_k \leq \|e_{\tilde{h}}\|_k \leq \|e\|_k. \tag{2.18}$$

The choice of the artificial boundary condition may imply that $\|\varepsilon\| << \|e\|$. This is a consequence of forcing the approximation ε to be zero along the boundaries of the elements, in the so-called hidden points. Since the reference error $e_{\tilde{h}}$ can take nonzero values in all these points, ε may be a poor approximation to $e_{\tilde{h}}$. In other words, interior residuals are considered but the information contained in the flux jumps is ignored.

2.3.4 Patch estimation and complete estimate

Once the interior estimate is computed, it is necessary to add the contribution of the flux jumps, that is, to improve the error estimation by adding nonzero values in the element boundaries. This can be done following the same idea of the interior estimation, precluding the direct computation of flux jumps and avoiding the flux splitting procedure.

The interior estimate is based on solving local problems in the elements. This has been done because using the finite element method, elements (Ω_k, $k = 1, 2, \ldots$) are the natural partition of the domain Ω. But other partitions can also be used. Let us consider a new family of disjoint subdomains (Λ_l, $l = 1, 2, \ldots$) covering Ω. Each one of these subdomains Λ_l overlaps a few number of elements. Moreover, these subdomains include the boundaries

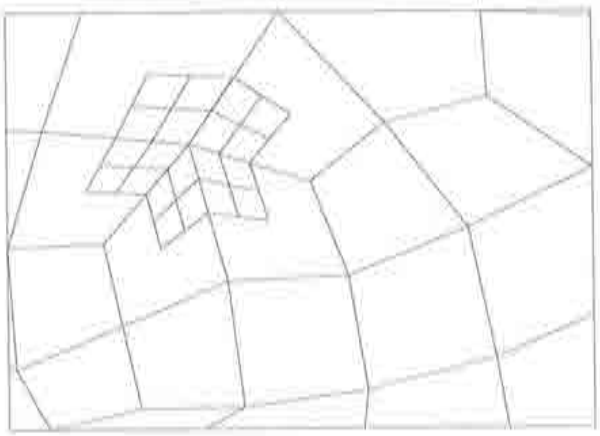

Figure 2.4: Patch submesh centered in a node of the computational mesh

of the elements. In order to simplify the exposition, in the following, the subdomains Λ_l are called patches. Using the elementary submeshes of figure 2.3, the most natural choice for patch subdomains is to associate them with the nodes of the mesh: each patch is associated with a node and includes a fourth of every element sharing the node(see figure 2.4 for an illustration).

The idea is to use this new partition to define new local problems for the error and to solve them. Local boundary conditions are imposed in the same fashion as in the previous phase (interior estimate). A new approximation to the error is obtained. This new approximation takes nonzero values in the boundary of the elements, where the interior estimate ε vanishes. Thus, the number of hidden points is drastically reduced. In fact, there are still a few. For instance, if the choice for the patches is the one shown in figure 2.4, the error estimation in the centre of the element edges is forced to zero.

In order to solve these problems each patch Λ_l must be discretized by a patch submesh. The discretization of equation 2.8 using this patch submesh leads to a system of equations analogous to equation 2.14:

$$\mathbf{K}_l^p \, \boldsymbol{\eta}_l = \mathbf{r}_l^p, \tag{2.19}$$

where $\boldsymbol{\eta}_l$ is nodal value vector representing the patch estimate η_l. Since patches cover the edges of the elements, the vector $\mathbf{r}_l^p$, which is the restriction of the residual $\mathbf{r}_{f_h}(\mathbf{u}_h)$ in equation 2.13 to the patch submesh, accounts for the residual associated with the flux jumps.

Using the patch estimate η_l, local and global estimates can be computed following equations analogous to 2.15 and 2.17. This is because patches are disjoint subdomains and therefore, the patch estimates are mutually orthogonal, exactly as interior estimates. In addition, a patch estimate η can be defined over the whole domain assembling the local estimates, similarly to what is shown in equation 2.16. However, if an element Ω_k and a patch Λ_l overlap, the associated interior estimate ε_k and patch estimate η_l, are not

orthogonal. That means that if the contributions of these two estimates are added, the lower bound properties of equation 2.18 are lost. In order to preclude this problem, each patch estimate η_l is forced to be orthogonal (according to $a(\cdot,\cdot)$) to the global interior estimate ε. That is, the linear condition

$$a(\eta_l, \varepsilon) = 0 \tag{2.20}$$

must be added to the linear system of equations (2.19). Of course, this condition can be expressed locally in the patch submesh, and takes the form

$$\boldsymbol{\eta}_l^T \underbrace{\mathbf{K}_l^p \, \boldsymbol{\varepsilon}_l}_{-\mathbf{r}_{l,\varepsilon}^p} = 0, \tag{2.21}$$

where $\boldsymbol{\varepsilon}_l$ is the restriction of ε to the patch submesh. As it can be seen, this condition is equivalent to forcing to zero the scalar product between the patch estimate $\boldsymbol{\eta}_l$ and the residual $\mathbf{r}_{l,\varepsilon}^p$ associated to the interior estimate ε. This residual can be seen as the restriction to the patch submesh of the internal forces associated to ε

$$\mathbf{f}_{\bar{h}}^{\text{int}}(\varepsilon) = -\mathbf{r}_{\varepsilon}. \tag{2.22}$$

Note that $\mathbf{r}_{l,\varepsilon}^p$ is different to the residual $\mathbf{r}_l^p$ of equation 2.19, which is a restriction of the internal forces associated to the actual reference error $e_{\bar{h}}$, and not to the estimate ε. In fact, $\mathbf{r}_{l,\varepsilon}^p$ accounts for the reactions caused by the artificial boundary conditions of zero error imposed in the element boundaries during the interior estimation of ε.

The linear condition can be implemented using the Lagrange multipliers technique (see [36]) and modifying the system of equations (2.19). Therefore, a complete estimate based on local computations can be simply defined as $e_{\bar{h}} = \varepsilon + \eta$, and thanks to the orthogonality of ε and η, its norm can be easily computed from the interior and the patch estimation

$$\|e_{\bar{h}}\|^2 = \|\varepsilon\|^2 + \|\eta\|^2. \tag{2.23}$$

Of course, this equation is also verified at the element level, and the lower bound properties hold for the complete estimate $e_{\bar{h}}$ too

$$\|e_{\bar{h}}\| \leq \|e_{\bar{h}}^{\star}\| \leq \|e\| \quad \text{and} \quad \|e_{\bar{h}}\|_k = \sqrt{\|\varepsilon\|_k^2 + \|\eta\|_k^2} \leq \|e_{\bar{h}}^{\star}\|_k \leq \|e\|_k. \tag{2.24}$$

In practice, the computation of the norm of η restricted to Ω_k is not natural, since it involves several patches. However, the goal of the estimator is to obtain an elementary error distribution. For this reason, the norm of the patch estimate η_l corresponding to the patch Λ_l can be equidistributed in the overlapping elements, loosing the lower bound properties at the local level, but simplifying the computations.

2.4 Error estimation for nonlinear problems

The error equation 2.8 is obtained from equation 2.3 using the linearity of $a(\cdot,\cdot)$, that is, it is assumed that

$$a(e + u_h, v) = a(e, v) + a(u_h, v). \tag{2.25}$$

Nevertheless, the original error equation is

$$a(e + u_h, v) = l(v) \text{ for all } v \in \mathcal{V}, \tag{2.26}$$

and, if the problem is nonlinear, equation 2.25 does not hold and, consequently, the error does not verify equation 2.8. However, equation 2.26 still holds, and the reference error can be characterised as the solution of the following discrete nonlinear problem

$$a(e_{\bar{h}} + u_h, v_{\bar{h}}) = l(v_{\bar{h}}) \text{ for all } v_{\bar{h}} \in \mathcal{V}_{\bar{h}}. \tag{2.27}$$

This equation can be expressed as a balance between internal and external nodal forces

$$\mathbf{f}_{\bar{h}}^{\text{int}}(\mathbf{u}_h + \mathbf{e}_{\bar{h}}) = \mathbf{f}_{\bar{h}}^{\text{ext}}. \tag{2.28}$$

This is a general nonlinear equation and must be solved using any standard nonlinear solver. In fact, this problem is equivalent to finding the reference solution $u_{\bar{h}}$ (recall that $u_{\bar{h}} = u_h + e_{\bar{h}}$). However, here, the unknown $e_{\bar{h}}$ is small compared with $u_{\bar{h}}$, and u_h can be taken as a fairly good initial approximation to $u_{\bar{h}}$. Consequently, this nonlinear problem is much easier than the original one.

Following the idea of figure 2.2, figure 2.5 illustrates how the initial stress method is used to solve the problem of equation 2.28. In this case internal forces are nonlinear and therefore $\mathbf{u}_h$ and $\mathbf{u}_{\bar{h}}$ are found intersecting the respective external force lines (horizontal) with the lines representing the internal force versus the displacement (which are not straight lines because of the nonlinearity). During the whole iteration process, the "slope" (iteration matrix) is kept constant. Due to the tolerance in the convergence of the nonlinear solver, the reference error $\mathbf{e}_{\bar{h}}$ and the estimated error are slightly different .

The main idea of the generalisation of the error estimator to nonlinear cases is to reproduce the same structure of the linear case with a different equation for the error. Thus, in this case the previous idea is used again, and the estimation of the error is splitted in two steps. Firstly, elementary problems are solved with zero error boundary conditions, and an interior estimate is computed. Secondly, the restriction of equation 2.26 to every patch is solved. In this case, the orthogonality condition between the patch estimate and the interior estimate cannot be expressed in terms of the stiffness matrix as in equation 2.21. Nevertheless, it can still be expressed as

$$\boldsymbol{\eta}_l^T \ \mathbf{r}_{l,\varepsilon}^p = 0, \tag{2.29}$$

being $\mathbf{r}_{l,\varepsilon}^p$ the restriction to the patch of the internal forces associated to the interior estimate.

Here, the energy cannot be measured using a standard norm related with the problem. However, following the idea of the previous case, an energetic quantity is defined that allows to measure the error. Recall that the discrete expression of the local error norm given in equation 2.15 is the scalar product of the displacement error vector and the residual force vector

$$\|\boldsymbol{\varepsilon}_k\|^2 = -\boldsymbol{\varepsilon}_k^T \mathbf{r}_k^e \text{ and } \|\boldsymbol{\eta}_l\|^2 = -\boldsymbol{\eta}_l^T \mathbf{r}_l^p. \tag{2.30}$$

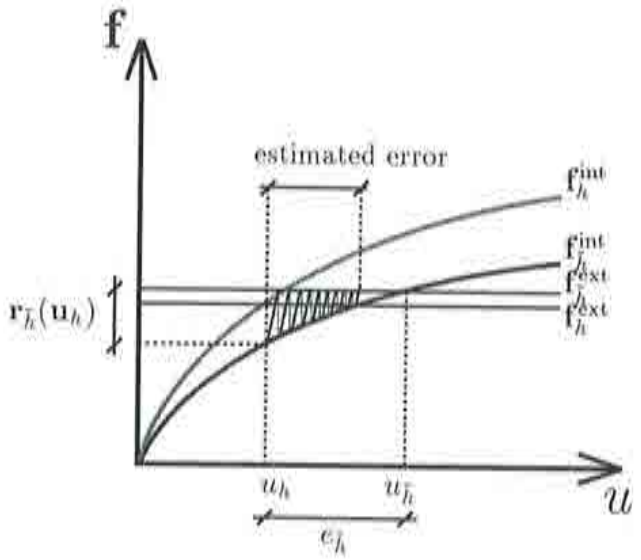

Figure 2.5: Graphic interpretation of reference error in nonlinear problems and fully nonlinear error estimation

Note that, since $\mathbf{r}_{l,\varepsilon}^p \neq \mathbf{r}_l^p$, the norm of $\boldsymbol{\eta}_l$ is not zero (see equation 2.29). This expression is general and can also be used in the nonlinear case.

This error estimator for nonlinear problems can be applied to mechanical problems in which Mazars nonlocal damage model is used. This is detailed in appendix B.

2.4.1 Tangent estimation

The error is assumed to be small compared with the solution. This stands also for the reference error, that is, $\|e_{\bar{h}}\| << \|u_h\|$. Under this assumption, the nonlinear problems should converge easily. Moreover, if this assumption is true, the nonlinearity of the first argument of $a(\cdot,\cdot)$ can be properly approximated using a tangent expansion around u_h (see [7])

$$a(e+u_h, v) \approx a(u_h, v) + a_T(u_h; e, v). \tag{2.31}$$

where $a_T(u_h;\cdot,\cdot)$ is the linear approximation to $a(\cdot,\cdot)$ around u_h. Replacing equation 2.31 in equation 2.26, a new error equation is found

$$a_T(u_h; e, v) = l(v) - a(u_h, v) \text{ for all } v \in \mathcal{V}. \tag{2.32}$$

Note that equation 2.32 is linear, which allows to characterize the reference error $e_{\bar{h}}$ as the solution of a linear problem

$$a_T(u_h; e_{\bar{h}}, v_{\bar{h}}) = l(v_{\bar{h}}) - a(u_h, v_{\bar{h}}) \text{ for all } v_{\bar{h}} \in \mathcal{V}_{\bar{h}}, \tag{2.33}$$

which is analogous to equation 2.10. Therefore, the reference error can be obtained solving the following linear system

$$\mathbf{K}_{\bar{r},\bar{h}}\ \mathbf{e}_{\bar{h}} = -\mathbf{r}_{\bar{h}}(\mathbf{u}_h) = \mathbf{f}_{\bar{h}}^{\text{ext}} - \mathbf{f}_{\bar{h}}^{\text{int}}(u_h), \tag{2.34}$$

where $\mathbf{K}_{\bar{r},\bar{h}}$ is the tangent matrix associated with the finer reference mesh. Again, this equation is linear, and has exactly the same structure of equation 2.12.

Following the idea of the graphic illustration of figures 2.2 and 2.5, figure 2.6 shows how the nonlinear case can be treated using a tangent approximation. The reference error is approximated using a tangent approximation of the curve representing the behaviour associated with the finer mesh.

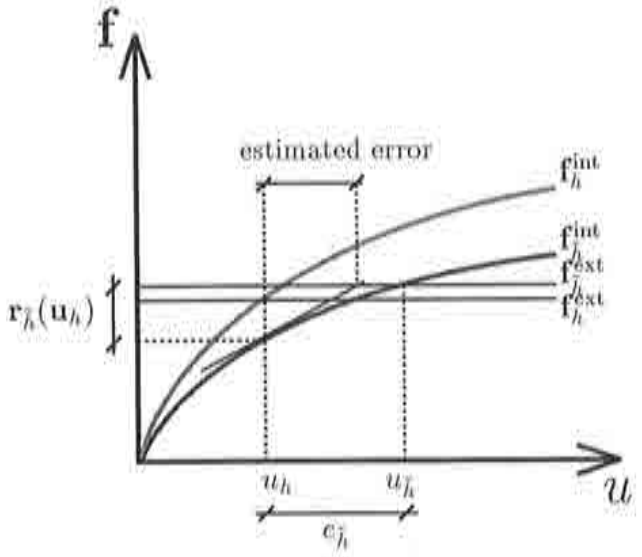

Figure 2.6: Graphic interpretation of reference error in nonlinear problems and error estimation using tangent approximation

Again, the computation of $e_{\bar{h}}$ solving the linear system of equations 2.34 is unaffordable, and the reference error is approximated using local computations. Therefore, the philosophy of the linear approximation can be fully respected, splitting the approximation in two phases, the interior estimation and the patch estimation. Thus, the computation involves small and linear local problems with trivial boundary conditions and the nonlinear generalisation inherits all the properties of the linear counterpart.

It is worth noting that, in the patch estimation phase, the orthogonality condition of equation 2.20 must be replaced by its tangent version

$$a_r(u_h; \eta_l, \varepsilon) = 0 \quad \text{or} \quad \boldsymbol{\eta}_l^T\ \mathbf{K}_{r,l}^p\ \boldsymbol{\epsilon}_l = 0, \tag{2.35}$$

being ε_l the restriction of ε to the patch Λ_l. In fact, this equation is a particular case of equation 2.29.

Once interior and patch estimates are computed, they must be measured and added. Thus, a nonlinear energy norm must be defined. If the tangent form $a_T(u_h;\cdot,\cdot)$ is symmetric positive definite, which holds for elliptic self-adjoint problems, the reference error $e_{\bar{h}}$ computed using equation 2.33 is the projection of the actual error e on $\mathcal{V}_{\bar{h}}$ following the scalar product $a_T(u_h;\cdot,\cdot)$. Moreover, assuming that, for small enough displacements, the behaviour of the system is linear and it is ruled by $a_T(u_h;\cdot,\cdot)$, the norm induced by $a_T(u_h;\cdot,\cdot)$ is analogous to the linear energy norm defined in equation 2.9. Thus, the norm induced by $a_T(u_h;\cdot,\cdot)$ is taken to measure the error.

This tangent version of the nonlinear error estimator can be used in problems with Perzyna softening viscoplasticity, as it is justified in section 3.3.

2.5 Evaluation of the pollution error (global estimation)

2.5.1 Linear case

Until now, the method presented approximates a reference error $e_{\bar{h}}$, defined from a refined mesh. Since the solution of the global problem in the refined mesh is unaffordable, the error is approximated solving local problems. Nevertheless, the errors transmitted from one zone of the domain to another cannot be taken into account by using purely local computations. Therefore, the so-called pollution errors are not detected by the error estimator.

Much attention is being paid to the pollution errors (see [32]), caused by singularities of the problem that 'pollute' the solution in the rest of the domain. In the current section, a strategy to capture the error missed by the local computations is presented. This method uses one global calculation with the original mesh, and leans on the fact that the local error estimator not only provides measures of the error, but also the error as a function (or vector of nodal displacements).

Characterisation of the global error

The previous sections describe a method to approximate the error e of a finite element solution u_h, defined in an interpolation space $\mathcal{V}_h$. To do this, a reference mesh generating a richer interpolation space $\mathcal{V}_{\bar{h}}$ is considered. The error of the solution in this reference mesh $u_{\bar{h}}$ is assumed to be negligible, and the estimated error is then an approximation of the reference error defined as $e_{\bar{h}} = u_{\bar{h}} - u_h$. An estimate e_L is then obtained from local computations, and consequently contains only local information.

The global error is defined as the part of the reference error $e_{\bar{h}}$ that the local estimate e_L fails to capture; $e_G := e_{\bar{h}} - e_L$. Since e_L is a projection of $e_{\bar{h}}$ on a subspace of the reference space $\mathcal{V}_{\bar{h}}$, e_L and e_G are orthogonal according to $a(\cdot,\cdot)$, and the following expression holds

$$\|e_{\bar{h}}\|^2 = \|e_L\|^2 + \|e_G\|^2. \tag{2.36}$$

According to equation 2.10 and using the linearity of the first argument of $a(\cdot,\cdot)$ and the definition of the global error, e_G can be characterised as the only element of $\mathcal{V}_{\bar{h}}$ that verifies

$$a(e_G, v_{\bar{h}}) = l(v_{\bar{h}}) - a(u_h, v_{\bar{h}}) - a(e_L, v_{\bar{h}}) \text{ for all } v_{\bar{h}} \in \mathcal{V}_{\bar{h}}. \tag{2.37}$$

Again, the resolution of equation 2.37 is unaffordable, as it is a global problem in the reference discretisation. Nevertheless, this equation can provide a simplified problem in order to approximate e_G.

Approximation of the global error

In the previous cases in which a global problem in the reference mesh was encountered, the excessive computational cost was precluded solving local problems. This cannot be done in this case, as long as global information about the error is required. Equation 2.37 allows to project e_G on any subspace of $\mathcal{V}_{\bar{h}}$, in particular on $\mathcal{V}_h$. By doing so, a low cost global problem is obtained and can be used to approximate the global error e_G.

Let e_G^* be the projection of e_G on $\mathcal{V}_h$, and consequently, an approximation of e_G. The approximated global error e_G^* is the only element of $\mathcal{V}_h$ that verifies the integral equation

$$a(e_G^*, v_h) = l(v_h) - a(u_h, v_h) - a(e_L, v_h) \text{ for all } v_h \in \mathcal{V}_h. \tag{2.38}$$

Note that this projection on the original space cannot be used to approximate the reference error $e_{\bar{h}}$, which is orthogonal to $\mathcal{V}_h$, that is

$$a(e_{\bar{h}}, v_h) = l(v_h) - a(u_h, v_h) = 0 \text{ for all } v_h \in \mathcal{V}_h. \tag{2.39}$$

So, according to equations 2.38 and 2.39, e_G^* can be characterised as the only element of $\mathcal{V}_h$ that verifies

$$a(e_G^*, v_h) = -a(e_L, v_h) \text{ for all } v_h \in \mathcal{V}_h. \tag{2.40}$$

In practical terms, e_G^* is identified to the vector of nodal displacements $\mathbf{e}_G^*$ in the computational mesh. Thus, equation 2.40 is equivalent to the linear system of equations

$$\mathbf{K}_h \mathbf{e}_G^* = -\mathbf{f}_L, \tag{2.41}$$

where $\mathbf{K}_h$ is the stiffness matrix associated to the computational mesh, which has already been used to compute u_h. The force term $\mathbf{f}_L$ is associated to $a(e_L, v_h)$, and its computation shows technical difficulties that are discussed in section 2.6.

Once $\mathbf{f}_L$ is obtained, the system can be solved without additional cost provided that $\mathbf{K}_h$ has been factorised to solve the original problem. Furthermore, since e_G^* is a projection of e_G, according to equation 2.36 a lower bound property of the global approximation holds

$$\|e_L\|^2 + \|e_G^*\|^2 \leq \|e_{\bar{h}}\|^2. \tag{2.42}$$

The contribution of e_G^* can also be accounted for locally, approximating the squared local norm of the reference error by $\|e_L\|_k^2 + \|e_G^*\|_k^2$. Nevertheless, this local estimate may loose the lower bound property, as long as the restrictions to an element of the patch estimation η and of e_G^* are not orthogonal in general.

2.5.2 Nonlinear case

The main ideas of the pollution error estimation in linear problems can be easily extended to the nonlinear case. If the first argument of $a(\cdot,\cdot)$ is nonlinear, equation 2.37 is not valid, and a nonlinear problem characterizes the global error

$$a(u_h + e_G + e_L, v_{\bar{h}}) = l(v_{\bar{h}}) \text{ for all } v_{\bar{h}} \in \mathcal{V}_{\bar{h}}. \tag{2.43}$$

Again, due to the cost of this problem (it is expressed in the reference mesh), this equation is approximated projecting e_G in the space $\mathcal{V}_h$. Therefore, the problem actually solved is

$$a(u_h + e_G^* + e_L, v_h) = l(v_h) \text{ for all } v_h \in \mathcal{V}_h. \tag{2.44}$$

This nonlinear problem is much easier to solve than the original problem as long as the error e_G is small in front of u_h. Therefore, $u_h + e_L$ can be taken as a good initial approximation.

As before, if a tangent approximation of the nonlinear problem is available, the nonlinear problem of equation 2.44 can be precluded solving the linear system

$$a_T(u_h; e_G^*, v_h) = -a_T(u_h; e_L, v_h) \text{ for all } v_h \in \mathcal{V}_h, \tag{2.45}$$

which is analogous to equation 2.40. Therefore, the global error e_G can be obtained solving a linear system of equations involving the tangent stiffness matrix, which may have been already factorised, depending on the nonlinear solver employed.

2.6 Computational aspects

In this section, several aspects related with the residual problems solved in the interior, the patch and the global estimation are discussed. The main difficulty that appears is that computations involving functions interpolated in the coarse mesh and functions interpolated in the fine mesh must be carried out. For instance, $\mathbf{f}_{\bar{h}}^{\text{int}}(u_h)$ involves both the reference mesh ($\bar{h}$) and the coarse mesh (u_h). Therefore, functions in one discretization must be expressed in the other one.

Firstly, the computational aspects related to the local problems (interior and patch estimation) are developed, distinguishing the linear and the nonlinear cases. Then, the difficulties encountered in the global estimation are presented for the linear and the nonlinear cases in a unified way.

2.6.1 Solution of the local problems

Linear case

As it has been seen in the linear estimation, the interior and patch estimates are computed solving local problems in which the source term is the residual $\mathbf{r}_{\bar{h}}(\mathbf{u}_h)$ restricted to the element ($\mathbf{r}_k^e$) or patch ($\mathbf{r}_l^p$) submesh (see equations 2.14 and 2.19). Recall that $\mathbf{r}_{\bar{h}}(\mathbf{u}_h)$ is the

discretisation of the residual form $a(u_h, \cdot) - l(\cdot)$ in the reference mesh, and can be expressed as

$$\mathbf{r}_{\tilde{h}}(\mathbf{u}_h) = \mathbf{f}_{\tilde{h}}^{\text{int}}(u_h) - \mathbf{f}_{\tilde{h}}^{\text{ext}}. \tag{2.46}$$

While the computation of $\mathbf{f}_{\tilde{h}}^{\text{ext}}$ is absolutely standard, $\mathbf{f}_{\tilde{h}}^{\text{int}}(u_h)$ is much more difficult to compute; the internal forces associated to a solution in the coarse mesh must be expressed as nodal forces in the fine mesh.

In this section, the shape functions that form a base of $\mathcal{V}_h$ are denoted as $N_i, i = 1, ..., n$, and those corresponding to the reference mesh, $\tilde{h}$, as $\tilde{N}_j, j = 1, ..., \tilde{n}$. Note that any element of these spaces can be expressed as a linear combination of the corresponding shape functions. On the other hand, the shape fuctions of the coarse mesh can be expressed in terms of the shape fuctions of the reference mesh as follows

$$N_i = \sum_{j}^{\tilde{n}} n_{ij} \tilde{N}_j \text{ for } j = 1, ..., n, \tag{2.47}$$

and a transformation matrix can be defined

$$\mathbf{N} = [n_{ij}], \tag{2.48}$$

being n_{ij} the value of N_i in the node associated to $\tilde{N}_j$.

In this case, according to equations 2.10 and 2.11, the k-th component of $\mathbf{f}_{\tilde{h}}^{\text{int}}(u_h)$ takes the form

$$(\mathbf{f}_{\tilde{h}}^{\text{int}}(u_h))_k = a(u_h, \tilde{N}_k). \tag{2.49}$$

This computation is not straightforward because u_h belongs to $\mathcal{V}_h$ and $\tilde{N}_k$ to $\mathcal{V}_{\tilde{h}}$. Making use of the bilinearity of $a(\cdot, \cdot)$, and expressing u_h in the base of $\mathcal{V}_h$ ($u_h = \sum_i^n \alpha_i N_i$) and N_i in the base of $\mathcal{V}_{\tilde{h}}$, this equation can be rewritten as

$$(\mathbf{f}_{\tilde{h}}^{\text{int}}(u_h))_k = a(\sum_{i}^{n} \alpha_i N_i, \tilde{N}_k) = \sum_{i}^{n} \alpha_i a(N_i, \tilde{N}_k) = \sum_{i}^{n} \sum_{j}^{\tilde{n}} \alpha_i n_{ij} a(\tilde{N}_j, \tilde{N}_k). \tag{2.50}$$

Since $a(\tilde{N}_j, \tilde{N}_k) = \{\mathbf{K}_{\tilde{h}}\}_{jk}$ and $\mathbf{K}_{\tilde{h}}$ is assumed symmetric, this equation can be easily expressed in matrix form, obtaining a compact expression for $\mathbf{f}_{\tilde{h}}^{\text{int}}(u_h)$

$$\mathbf{f}_{\tilde{h}}^{\text{int}}(u_h) = \mathbf{K}_{\tilde{h}} \ \mathbf{N}^T \ u_h. \tag{2.51}$$

Of course, since the reference mesh may have an excessive number of degrees of freedom, the storage of $\mathbf{N}$ and of $\mathbf{K}_{\tilde{h}}$ may be unreasonable. In addition, since the local stiffness matrices $\mathbf{K}_k^e$ must be computed in the interior estimation, computing $\mathbf{K}_{\tilde{h}}$ apart is redundant. Thus, the calculation of $\mathbf{f}_{\tilde{h}}^{\text{int}}(u_h)$ must be done element by element during the interior estimation, interpolating u_h in the elementary submesh to compute $\mathbf{r}_k^e$ locally. Then, the interpolated displacements in each element submesh must be assembled to obtain a global interpolation of u_h in the reference mesh. Therefore, in the patch estimation, $\mathbf{r}_l^p$ can be easily computed from the local stiffness matrix and from the restriction of the assembled displacement vector to the patch submesh. Thus, u_h is interpolated in the reference mesh once, during the interior estimation, and stored to be used in the patch estimation.

Nonlinear case

In this case, a general nonlinear problem must be solved (see equation 2.28). In usual nonlinear models, the nonlinearity is controlled by the so-called internal variables (equivalent viscoplastic strain in Perzyna model and damage in Mazars model) that are expressed in the same points that the stresses. As it has been said, the global nonlinear problem is approximated by computations in local submeshes. The difficulty here is that the initial approximation for the nonlinear problem is u_h, which is expressed in the coarse mesh. In fact, what is really needed as an initial approximation of the nonlinear local problem are the stresses $\boldsymbol{\sigma}_h$ and the internal variables d_h associated to u_h, expressed in the reference mesh. Again, these variables can be extended to the reference mesh element by element during the interior estimation, and assembled and stored to be used later in the patch estimation.

Note that, as long as the base points of $\boldsymbol{\sigma}_h$ and d_h are interior to the element (typically, the Gauss points), these variables are expressed in interior points of the local submesh in which they must be extended. Therefore, the values of $\boldsymbol{\sigma}_h$ and d_h must be extrapolated in the outer elements of the submesh. This can lead to violations of the constitutive model or to meaningless values that must be corrected accordingly. For instance, in elastoplastic models, the extrapolated stresses can be higher than the original values of $\boldsymbol{\sigma}_h$ and go outside the yield surface, which is forbidden by the constitutive model. In this case, these values can be corrected and sent back to the yield surface. The extrapolation of the internal variables also needs corrections, depending on the constitutive model. For example, the damage variable of Mazars model must take values between zero and one, which can be violated as a result of the extrapolation. Therefore, if values greater that one are obtained, they are set to one. The process is analogous when negative values are found.

Finally, it is worth noting that to measure the error in the nonlinear estimation the local residuals are still needed (see equation 2.30). These local residuals are the restriction of $\mathbf{r}_{\bar{h}}(\mathbf{u}_h)$ to the local submeshes. As it has been said, the difficulty of computing these residuals stems from the computation of $\mathbf{f}_h^{\text{int}}(u_h)$. In this case, owing to the fact that the stresses $\boldsymbol{\sigma}_h$ have already been expressed in the local submeshes to solve the local problems, the internal forces in the fine mesh associated to the solution u_h can be easily computed integrating $\boldsymbol{\sigma}_h$ into equivalent nodal forces of the local submesh.

Storage or recalculation ?

According to what has been said in this section, information lying on the coarse computational mesh must be translated to the fine reference mesh, in order to compute some terms in the estimation. This transfer of information requires a computational effort.

On the other hand, the information expressed in the reference mesh is needed twice, firstly in the interior estimation and later in the patch estimation. Therefore, a first idea pointed out in the previous paragraphs is to translate the information of the coarse mesh into the fine mesh once, during the interior estimation, then store it, and use it later for the patch estimation. Nevertheless, when very large problems are attempted, the memory requirements of storing several variables in the reference mesh may turn out to be unafford-

able. In this case, the transfer of variables should be done twice, firstly element by element in the interior estimation, and then for every patch, without any storage.

Thus, the choice between one single calculation and a large storage, or local storage but two calculations is a matter of memory and CPU availability.

2.6.2 Computation of the source term in global estimation

The computation of the vector $\mathbf{f}_L$ also involves technical difficulties. Recall that $\mathbf{f}_L$ results from discretizing the form $a(e_L, \cdot)$ in the space $\mathcal{V}_h$. Again, since e_L belongs to $\mathcal{V}_h$, this computation is not straightforward. In this case, the k-th component of $\mathbf{f}_L$ is of the form

$$(\mathbf{f}_L)_k = a(e_L, N_k), \tag{2.52}$$

which can be written, using equation 2.47 and the linearity of the second argument of $a(\cdot, \cdot)$ (even in nonlinear problems), as

$$(\mathbf{f}_L)_k = a(e_L, \sum_j^{\tilde{n}} n_{kj} \tilde{N}_j) = \sum_j^{\tilde{n}} n_{kj} a(e_L, \tilde{N}_j). \tag{2.53}$$

Rewritting in matrix form, the following equation is obtained

$$\mathbf{f}_L = \mathbf{N} \mathbf{f}_h^{\text{int}}(e_L). \tag{2.54}$$

The computation of $\mathbf{f}_h^{\text{int}}(e_L)$ does not present difficulties as long as it is expressed in the same discretization that e_L. Again, this equation is formally interesting, but not very practical as long as global computations involving the reference mesh are required. In this case, there is also a local way of computing; each component of $\mathbf{f}_L$ involves only one node of the coarse mesh, and consequently the elements sharing this node. Therefore, $\mathbf{f}_L$ can be computed component by component using local computations involving a few elements. However, since one element has more than one node, this local computation forces to recalculate, with an additional computational effort.

Chapter 3

VISCOPLASTIC REGULARISATION

The current chapter presents the use of Perzyna viscoplasticity in the aim of obtaining a regular quasi-static problem presenting strain localisation with a softening material. To do this, several numerical examples are presented and analysed.

Section 3.1 illustrates the need of a well-posed problem, reviewing some relevant aspects of viscoplastic regularisation. Then, the governing equations are presented, and the numerical reference example is described in section 3.2. Section 3.3 describes and analyses the strain localisation phenomenon under quasi-static conditions, studying its inception and further evolution. The well-posedness of the problem has its numerical translation in mesh objective approximated solutions, which is shown in section 3.4. Finally, section 3.5 deals with the shear band width and the influence of several parameters.

3.1 Introduction

Rate independent softening plasticity: an ill-posed problem

As it has been said in chapter 1, the numerical simulation of strain localisation caused by softening fails when classical rate independent models are used, leading to ill-posed boundary or initial value problems. In the localised zones, there is a change of type in the govening equations: in the quasi-static case they lose ellipticity and in dynamics they change from hyperbolic to elliptic. Therefore, they do not have proper boundary conditions in these zones and the uniqueness of the solution is lost. Thus, the localisation size or band width, which is a very important physical feature in localisation problems, is inherently not unique; infinite bifurcation modes exist with arbitrarily narrow localised zones (see [16]).

The numerical consequences of these mathematical problems are severe. In the first place, the numerical solution of the ill-posed problem is unstable and requires a great computational effort (see [16]). Moreover, the solution found is not reliable, since a different mesh would give different results: the solution is pathologically mesh dependent. As the

mathematical problem has not unique solution, the numerical method switches to the solution presenting narrower band that the discretisation can describe. In other words, the band width (the solution) is set by the mesh size. Other important features of the solution, such as the energy dissipation or the global stiffness, also depend on the mesh. In certain problems, completely different shear bands are obtained depending on the elements orientation (see [39]). Of course, the results are meaningless, resulting from an inherently bad constitutive modelling.

Figure 3.1 illustrates the mesh dependence of the numerical results. A certain strain localisation problem (described later) of imposed displacement is modelled using classical rate independent J_2 plasticity with a softening modulus of one hundredth of the elastic Young modulus. The computations are carried out for two different meshes. It can be noticed that the shear band is as narrow as the mesh allows it; the finer mesh (b) shows a narrower band and its reaction-displacement relation drops faster than the one of example (a). Thus, the global stiffness and the energy dissipation during failure (the area comprised under the nonlinear branch of the curve), which are important physical features of the problem, are mesh dependent. On the other hand, due to the numerical instability referred to in the previous paragraph, example (b) diverges very soon.

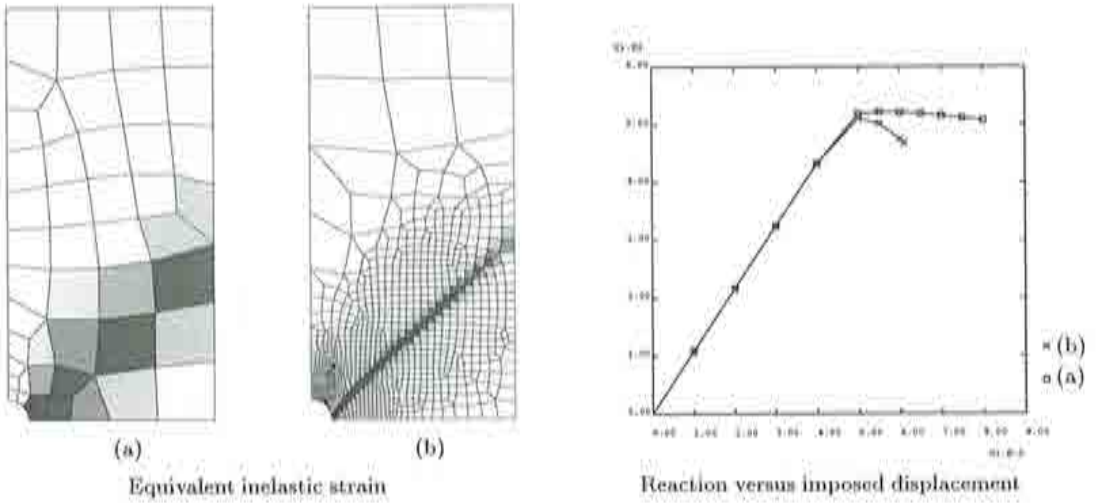

Figure 3.1: Mesh dependence of rate independent softening plasticity

Of course, this unproper modelling makes it impossible to perform adaptivity, as long as a change in the discretisation leads to a different solution. In addition, as the mesh is refined, the errors in the band increase unboundly. To make things worse, as the boundary value problem looses ellipticity, usual error estimators, and in particular the estimator presented in chapter 2, cannot be used.

Viscoplastic regularisation

Several localisation limiters or regularisation techniques have been proposed to remedy this undesirable situation, among which is the regularisation via viscoplasticity. It is well known that the introduction of rate dependence into the constitutive model preserves the well-posedness of the problem once strain localisation has occurred, maintaining the type of the governing equations unchanged (see [16], [13], [33]).

In static problems with rate independent nonlinear models, the resulting nonlinear system is solved by means of an incremental iterative method, in which the loading process is parametrized by a pseudotime. This pseudotime is physically meaningless and a change of its units does not alter the result. On the contrary, in rate dependent models, this parameter has a physical meaning. Therefore, despite the fact that when inertial forces are neglected with rate dependent solids time does not appear explicitly in the momentum balance, it is still an independent variable because it is present in the constitutive relations. Thus, it is more proper to talk of quasi-static loading conditions rather than static loading conditions.

Many authors use the viscous effects to regularise fully transient problems and maintain the governing equations hyperbolic ([16], [6], [33], [30], [9]). The results obtained are mesh objective, with finite band widths. When it comes to quasi-statics, owing to the fact that the quasi-static problem is simply a dynamic problem in which inertia terms are below the threshold of computational accuracy, viscoplasticity is still a sound regularisation technique. From a physical point of view, since the viscous effects are still present, the viscoplastic quasi-static problem is regular as well. Indeed, viscoplastic regularisation has also been used to regularise quasi-static problems (see [16], [36], [5]).

In the current work, the Perzyna viscoplastic model (see [22]) has been used to obtain a regular quasi-static problem with softening. Other authors have also used this localisation limiter (see [33] and [30]). This model, formulated and studied in detail in appendix A, decomposes the strain into its elastic and inelastic part, as in usual plasticity, and uses the Von Mises yield function. An internal variable or equivalent viscoplastic strain that controls the plastification is also defined, which rules the softening behaviour; the yield stress is reduced as the internal variable increases. At this stage, the model is identical to rate independent plasticity. However, the flow rules are different, and in viscoplasticity the stress states can be outside the yield function as there is no consistency condition. Thus, a viscous overstress caused by the strain rate appears, carrying part of the load.

Note that, as long as J_2 plasticity is considered, the material plastifies depending on the deviatoric stress tensor. Therefore, the frictional properties are more critical than the cohesive ones and Mode-II localisation (shear banding) is more likely to appear. In fact, J_2 plasticity is usually used to model metals, such as steel, in which failure is often preceded by shear band localisation. Nevertheless, viscous effects can also be used to regularise constitutive models that lead to fracture localisation, such as damage models (see [23]).

Length scale

The use of localisation limiters is associated with the introduction of an internal legth scale, also called intrinsic characteristic length, into the problem (see [24], [5], [13], etc). This internal length scales the problem, bounding the minimum shear band width. In the viscoplastic models, the internal length does not appear explicitly in the formulation. This internal length and its relation with the band width has been widely studied, specially in transient problems.

In the dynamic case, things seem to be quite clear. The characteristic length can be deduced from a dimensional analysis of the governing equations ([16]), and depends only on material parameters. This internal length is related with the size of the localised region. A theoretical analysis of the spatial propagation and attenuation of waves in the softening region provides a precise expression for the internal length scale in terms of material parameters (see [30] and [33]). This expression is contrasted successfully by numerical experiments, and allows to predict the shear band witdh with precision. A simple physical interpretation to the fact that the band width can be expressed in terms of the material can be made. In dynamic problems, localisation is triggered by the reflection and propagation of stress waves in the solid traveling at a celerity which depends on the material. When two stress waves meet and the yield stress is reached, localization occurs mobilising the viscous effects. These effects, that obviously depend on the material, can be seen as a time delay in the response of the material. Thus, combining the wave celerity and the time of response of the viscoplastic material, the internal length appears naturally.

On the contrary, the internal length scale in quasi-static case is not so evident, and does not seem to depend uniquely on material parameters as in the dynamic case. In fact, the mechanism triggering localization in dynamics described above does not rule the quasi-static response. In section 3.3, the quasi-static case is analysed in detail. According to [5], a length scale does not emanate from the governing differential equations for the quasi-static response of a viscoplastic material, which does not possess a parameter of the dimension of length. Nevertheless, the problem has a characteristic length that emanates from the whole boundary value problem (equations, domain and boundary conditions) and the results obtained under quasi-static loading conditions are also mesh objective.

Imperfection size

Very often, in academical problems with regular domains, localisation is triggered by heterogeneities or imperfections in the geometry or the material, specially in the quasi-static case. In one or two dimensional dynamic problems, these imperfections are not necessary to obtain strain localisation, which can be simply caused by wave propagation phenomena (see [30], [16], [24], [33]). On the contrary, in one dimensional quasi-static homogeneous problems, an imperfection is needed to trigger localisation. For one dimensional quasi-static solutions, several authors maintain that the size of the imperfection sets the width of the shear band, and is the governing length scale of the problem (see [16], [5]).

In two dimensional problems, the concept of imperfection has not so much sense as a

geometric non-regularity, such as sharp boundaries (see [39]), can be enough to lead to a non-homogeneous state that ends up in strain localisation. Nevertheless, imperfections are still used very often to trigger localisation in regular domains, introducing a variation of the material characteristics (see [6] and [33]) or simply geometric defaults in the specimen (see [37]).

Despite this intensive use of imperfections in two dimensional problems, little attention has been given to its influence in the solution. However, [33] studies the interaction between the material length scale and the imperfection size in dynamics. Its conclusions are discussed later in section 3.5. Note that in dynamics the material length scale is well-known. Unfortunately, the quasi-static multi-dimensional case is not so crystal clear and no references have been found on the internal length scale and the influence of imperfections.

3.2 Problem statement

3.2.1 Governing equations

Incremental boundary value problem

Considering quasi-static loading conditions means that the inertial forces caused by accelerations are neglected in front of other forces. Nevertheless, the problem is not purely static as long as the material response depends on strain rates. Recall that with rate dependent materials, the loading process is parametrised by the physical time. Therefore, in essence, the quasi-static problem is an initial value problem. However, neglecting the inertial forces simplifies the equations, and, similarly to a rate independent case, the problem can be formulated as a boundary value problem at every instant, or an incremental boundary value problem.

Thus, the governing equations presented are those of the static case, which must be verified at every instant of the loading process. Apart from that, the fact that the load is parametrized by the physical time in the incremental iterative process must be taken into account. So, the unknown of the problem is the displacement field u defined in the domain Ω verifying

$$\begin{cases} \nabla \cdot \boldsymbol{\sigma}(u) + b &= 0 & \text{in } \Omega \\ u &= g_d & \text{on } \Gamma_d \\ \boldsymbol{\sigma}(u) \cdot n &= g_n & \text{on } \Gamma_n \end{cases} \tag{3.1}$$

where $\boldsymbol{\sigma}(u)$ is the stress tensor associated with the displacements u, b the body force term and g_d and g_n the prescribed values of Dirichlet and Neumann boundary conditions respectively. The first equation represents the quasi-static equilibrium neglecting the inertial forces $\rho\ddot{u}$. Here, no the body forces are considered, that is $b = 0$. The incremental boundary value problem can be formulated rewriting the equations 3.1 in terms of rate quantities and starting from an equilibrated initial configuration.

Constitutive model

The constitutive model describes the material behaviour, relating strains and stresses. As it has been said, the model considered here, Perzyna viscoplasticity, provides a proper modelling of the quasi-static problem, reproducing the softening behaviour that leads to strain localisation, and being mathematically consistent. Thus, the boundary value problem, or incremental boundary value problem, is well posed and has unique solution, that is, the incremental equilibrium equations remain elliptic (see [16]). According to this, the tangent form of the weak problem (see chapter 2) is symmetric positive definite. This property is very important because it justifies the use of the error estimator for nonlinear problems in its tangent version. Moreover, since the model is formulated in terms of rate quantities (see appendix A), the tangent stiffness matrix is easily obtained at every instant.

Large strains

It is important to point out that large strains have been taken into account. In shear band localisation problems, where very high shear strains are reached, important rotations take place and the inclusion of this effect can be crucial to model properly the phenomenon. Large strains are represented by the rate-of-deformation tensor, which is additively decomposed into an elastic part and a viscoplastic part. The elastic rate of deformation is related, by means of an hypoelastic constitutive law, to the Truesdell objective stress rate (see [31]). The viscoplastic rate-of-deformation is given by the equations of Perzyna viscoplasticity. For the numerical time-integration, the midpoint algorithm proposed in [25] is employed.

3.2.2 Description of the reference example

The example presented in figure 3.2 reproduces the compression of a plane strain rectangular specimen. In order to induce the strain localisation in such a regular specimen, imperfections must be introduced to avoid an homogeneous solution. As it has been said before, these imperfections can be introduced by geometric heterogeneities. Here, the specimen is weakened by a circular opening in its centre. Consequently, the problem has two axes of symmetry, which allow to study only one fourth of the specimen. The computational domain is also shown in the figure.

In this example, as well as in other similar examples presented along the work, the load is applied imposing a displacement at the top of the specimen of $2\,\delta$, which results in δ for the computational domain (see figure 3.2). As long as the material is rate dependent, the velocity at which the displacement is imposed is relevant. Here, this velocity is considered constant, that is $\delta = v \cdot t$. The resulting boundary conditions for the problem that is actually solved in the computational domain are shown in the figure: half of the total displacement is imposed at the upper boundary, homogeneous Dirichlet conditions in the x and y directions are imposed in the vertical and the horizontal axes of symmetry respectively, and the rest of the boundary has homogeneous Neumann conditions (free boundary).

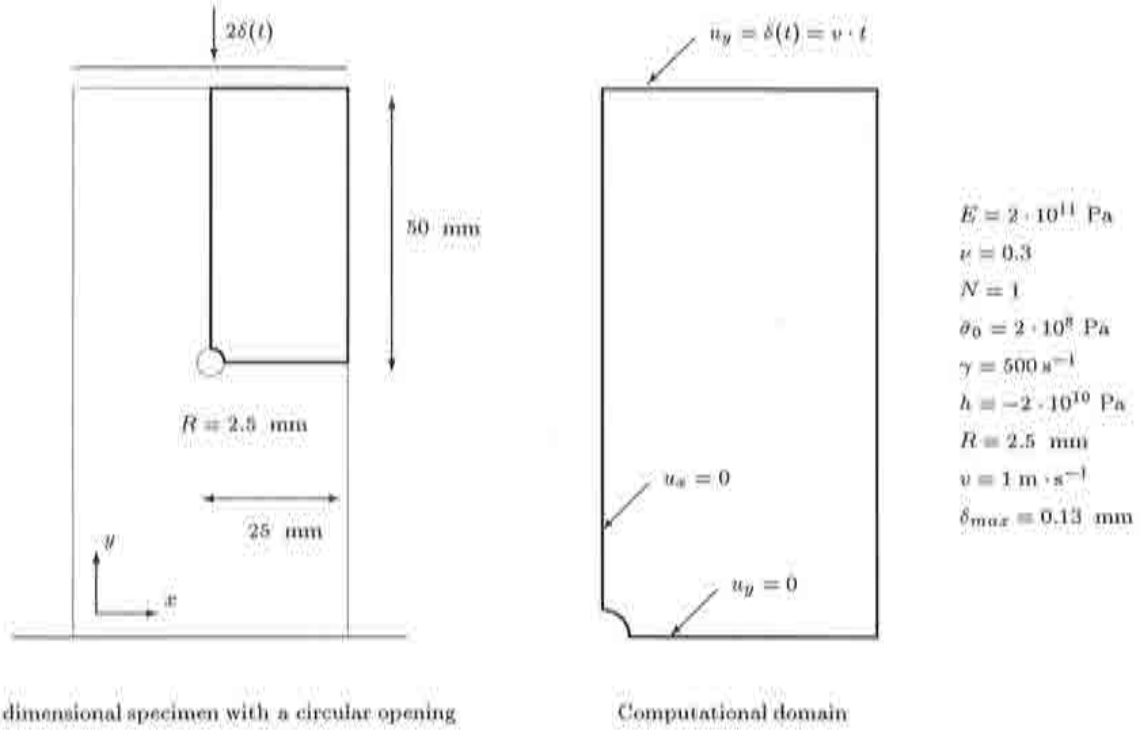

Figure 3.2: Description of the example

The nonlinear algebraic system, resulting from the discretisation of the equations presented above in the computational domain, is approximated with an updated Lagrangian finite element formulation, using quadrilateral eight-noded elements and reduced integration (four Gauss points).

The geometric description of the specimen is given in the figure. The only dimension that changes in the following examples is the imperfection size R. The loading conditions are characterised by the imposed displacement rate v, and by the maximum displacement reached δ_{max}. The material parameters E, ν, N, $\bar{\sigma}_0$, γ and h define the constitutive model, and are detailed and studied in appendix A. It is worth noting that the parameter h is the hardening/softening parameter, depending on its sign. A negative value, like in this case, models the softening behaviour.

The values of these parameters shown in figure 3.2 define the reference example, that allows to compare the results with other parameter sets. These material parameters simulate a steel.

3.3 Strain localisation with a softening material

In the current section, the approximate solution of the reference problem is presented in order to illustrate the softening and strain localisation phenomena (figure 3.3). This solution is also analysed by means of profiles across the shear band (figures 3.4 and 3.5), providing a physical understanding of the inception of localisation, and the post-localisation stage.

Figure 3.3 illustrates qualitatively the solution of the reference example. The curve represents the reaction at the top of the specimen (in fact, only half of the reaction corresponding to the computational domain is computed) versus the displacement imposed, and shows clearly the global softening behaviour of the post-localisation response. Note that, despite the softening parameter (one tenth of E) is much more pronounced here than in the rate independent examples (see section 3.1), no numerical stability problems are encountered. This observation agrees with the conclusions of [16], according to which the stability problems of the rate independent approach to strain softening are eliminated by the inclusion of rate dependency. The solution has been extended to the whole domain to show the shear banding phenomenon understandingly in the specimens of figure 3.3. The deformed mesh shows how the deformation concentrates in shear bands, and the equivalent inelastic strain (κ) contours delimitate clearly the plastified material in a localised zone. Note that the band width is clearly finite, even if the mesh would allow narrower bands. In the following examples, the same scale has been used to represent the inelastic strain contours.

Figure 3.4 shows profiles of the inelastic strain across the shear band at several moments of the load process, describing the evolution of this variable as the shear band develops. In the first stages, the inelastic strain distribution is very smooth, and does not concentrate clearly over a certain domain. However, as it grows, it becomes clear that the band width is set at the initial stages; no matter how much the inelastic strain grows, it does so over a localised zone. Note that when very high inelastic strains are reached, the elastic strains become negligible in front of the former, that are almost equal to the total strains. Therefore, the profiles of the total strain are very similar to those plotted in the figure, and, in effect, this is a strain localisation problem. On the other hand, it is worth noting that the computed inelastic strain is a discountinous field as long as it is expressed in the Gauss points. However, the profiles plotted here are of a smoothed field, and consequently continuous. In fact, the interelementary jumps are relevant, for instance, in the context of interpolation errors. These aspects are discussed in chapter 4, in reference to the error indicators.

The figure also shows the location of the lines (A-A') and (B-B') along which the profiles are represented in the figures.

In order to study the inception of localisation, the evolution of the Von Mises equivalent stress and yield stress is represented in figure 3.5 at six load stages. The Von Mises equivalent stress is a scalar variable that represents the stress state of the material, as long as J_2 plasticity is considered. Recall that the softening behaviour makes that, as the material plasitifies, the yield stress decreases. When very high inelastic strains are reached, the

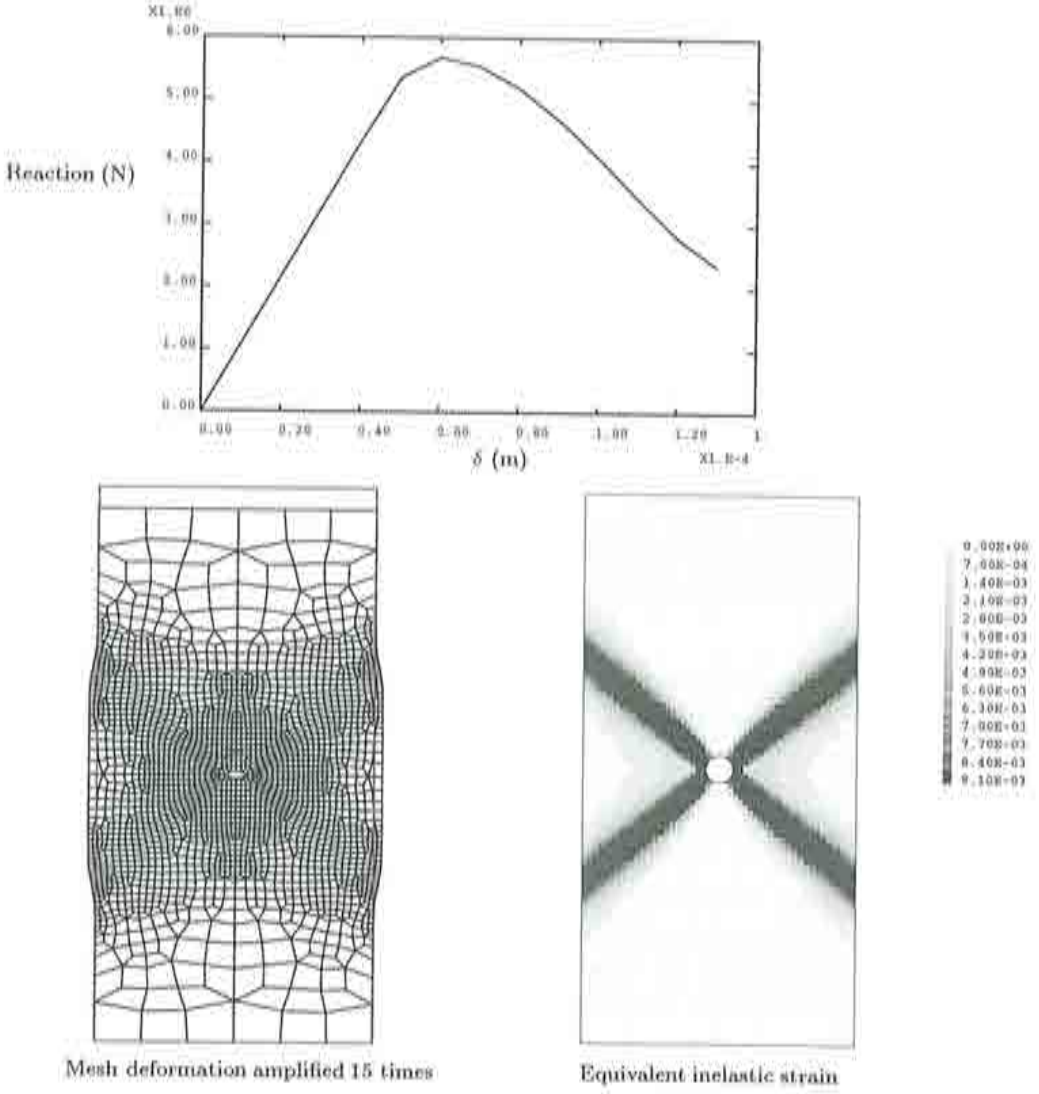

Figure 3.3: General results: softening and shear banding

yield stress can become zero, so that the material only offers a residual resistance due to the viscous overstress (see section A.4). This residual resistence does not exist with rate independent materials.

Recall also that the difference between the Von Mises stress and the yield stress defines the yield function f (see section A.1). The yield function controls the inelastic flow, that takes place only when f is positive (the solid line is above the dashed line). The positive value of f, say the distance between the two curves when the solid one is above the dashed one, represents the viscous overstress due to the strain rate. The inelastic strain rate grows with f, which tends to relax with time (the stress state tends to go back to the yield surface).

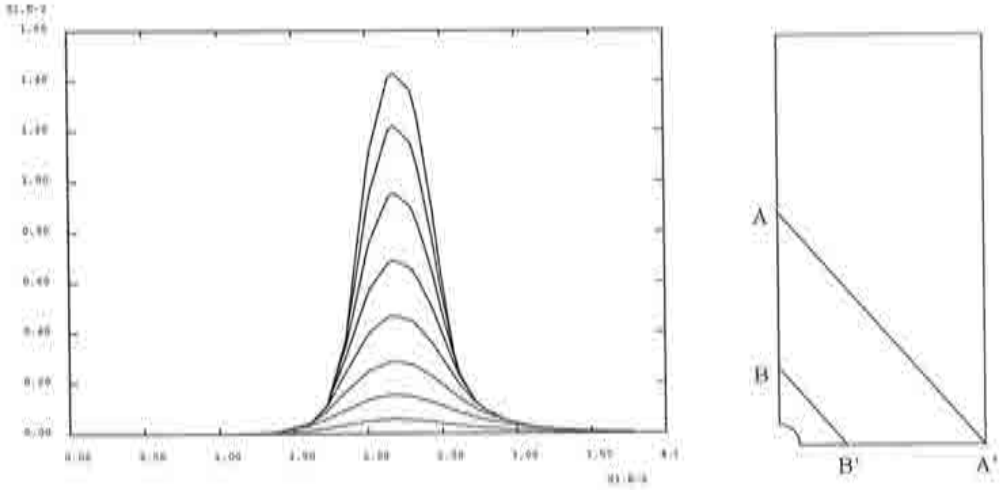

Figure 3.4: Evolution of the profile of the equivalent inelastic strain across the shear band along the normal direction (A-A')

See section A.3 for illustration.

Once these basic properties of Perzyna viscoplasticity have been reviewed, the succession of plots in figure 3.5 can be analysed. The first stage, with $\delta = 0.04$ mm, is still in the elastic domain, as long as the Von Mises stress is below the yield stress. Nevertheless, an initial perturbation due to the imperfection can be observed: the Von Mises stress is slightly higher in the centre of the profile. Therefore, as the load grows ($\delta = 0.06$ mm), this part enters the inelastic domain in the first place, and the inelastic flow results in a decrease of the yield stress (strain softening) in this zone. The viscous overstress can be observed clearly from this moment on. Then, this zone becomes weaker and consequently takes the main part of the imposed deformation. But owing to the strain softening behaviour, this new deformation weakens even more this region that will deform more and more. Thus, strain localisation is unchained. This process is smoothed by the viscous effects, which allow that the Von Mises stress decreases with a certain delay with respect to the yield stress (on the contrary, in rate independent plasticity, the Von Mises stress cannot be higher than the yield stress). All this can be observed in the following plots, reaching a point in which a part of the shear band is fully yielded (the yield stress is zero) and resists only because of the viscous overstress. As a matter of fact, a nearly uniform viscous flow takes place at this zone.

Note that in the process, the Von Mises stress decreases and tends to be uniform across the shear band. It is clear that this localisation phenomenon is associated with intense strains, and not with stress variations. In the decrease of the Von Mises stress, the solid line leaves part of the dashed line above it. This means that these zones in which f becomes negative are no longer flowing, and the yield stress remains unchanged. Thus, the shear band width cannot grow as the shear band develops, and remains bounded. Thus, the observation made in reference to figure 3.4, that the shear band width is set at the initial

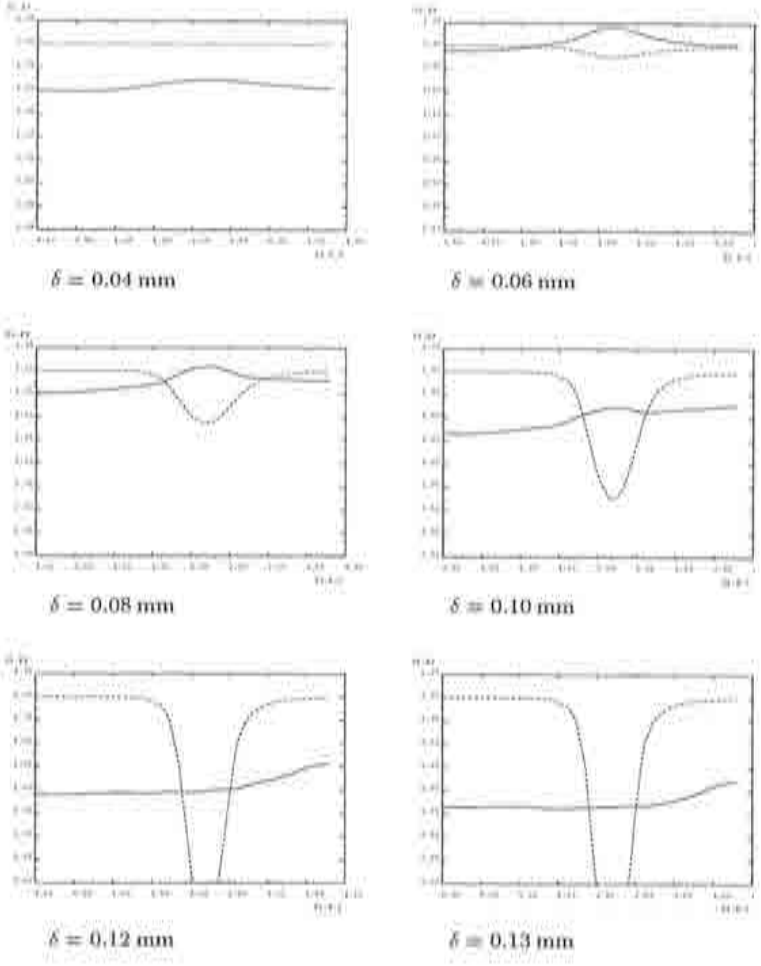

Figure 3.5: Evolution of the Von Mises equivalent stress (solid line) and the yield stress (dashed line) in the loading process

stages of the process, is confirmed here.

Finally, figure 3.6 provides a simple scheme of the failure mechanism, distinguishing two rigid parts, with almost no deformation, a the shear band, which absorbs all the imposed displacement with an intense shear deformation. A reaction-displacement curve of a loading process carried out until $\delta = 0.19$ mm is also shown. It is clear that, at very advanced stages, the specimen offers a constant residual resitance due only to the viscous effects, as long as the central part of the band is totally yielded.

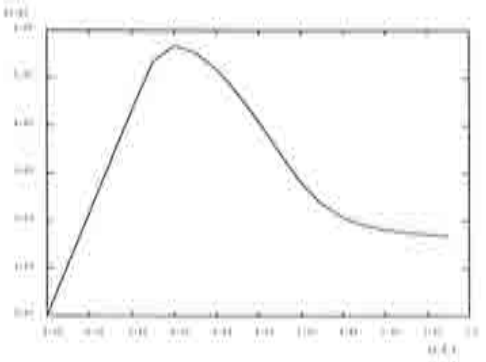

Reaction versus imposed displacement

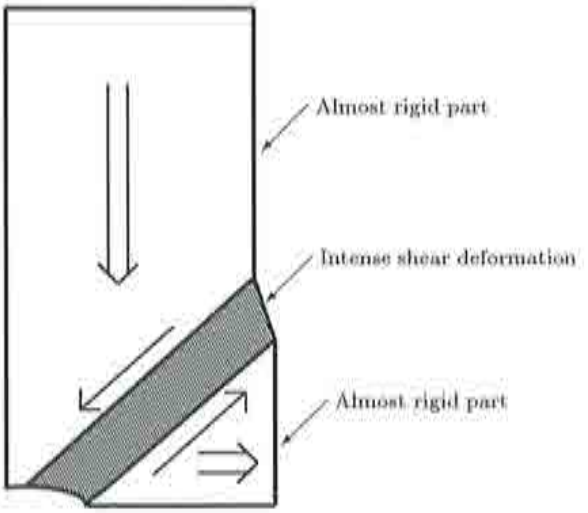

Figure 3.6: Reaction-displacement curve with $\delta_{max} = 0.19$ mm, and scheme of the shear band phenomenon

3.4 Mesh objectivity

To study the mesh independence of the viscoplastic solution, the reference example has been solved with different meshes. Figure 3.7 shows how the numerical solution of a well-posed problem leads to mesh objective results. Thus, the uniqueness of the solution of the boundary value problem allows to perform a remeshing process, as long as the approximated solution with different meshes is the same, except for the discretisation errors.

This figure shows the results obtained with three different meshes, (a), (b) and (c), whith different element sizes. The contour plots of the equivalent inelastic strain show that the band width is independent of the mesh size. Mesh (a) is too coarse to capture accurately the shear band, while the results of meshes (b) and (c) are very similar.

It is obvious from the curve representing the reaction versus the imposed displacement that, again, the results are not pathologically mesh sensitive; even if mesh (a) leads to slightly different results, as soon as the mesh is fine enough to describe the shear band pattern correctly, the reasonable mesh sensitivity due to too coarse meshes disappears. Thus, this is not the undesirable mesh dependence that is encountered when the numerical approximation of an ill-posed problem is attempted, but a natural mesh dependence caused by a too poor discretisation (note that the points defining these curves do not represent the loading steps, which are smaller).

The profiles of the inelastic strain across the shear band illustrate the same idea. The profiles are taken along the normal direction to the shear band (A-A') (see figure 3.4). Again, the approximations corresponding to meshes (b) and (c) match almost exactly, whereas mesh (a) is insufficient to assess accurately the shear band, even if the results are reasonable.

Finally, a physical magnitude that is often considerd when mesh sensitivity is studied is the energy consumption, which can be defined as the work done over the whole domain in the loading process

$$W_{int} = \int_{\Omega} \left(\int_{t_0}^{t_1} \boldsymbol{\sigma} : \dot{\boldsymbol{\varepsilon}} dt \right) d\Omega. \tag{3.2}$$

Table 3.1 shows that the energy consumption with mesh (a) is a little bit higher than the one computed with the other two meshes, that practically coincide. In rate independent softening plasticity, as the mesh is refined, the energy consumption decreases, and at the limit, failure takes place without energy consumption ([24]). Here, on the contrary, this magnitude is mesh objective.

mesh	elements	W_{int} (J)
(a)	110	492.55
(b)	580	489.28
(c)	1206	489.12

Table 3.1: Energy consumption

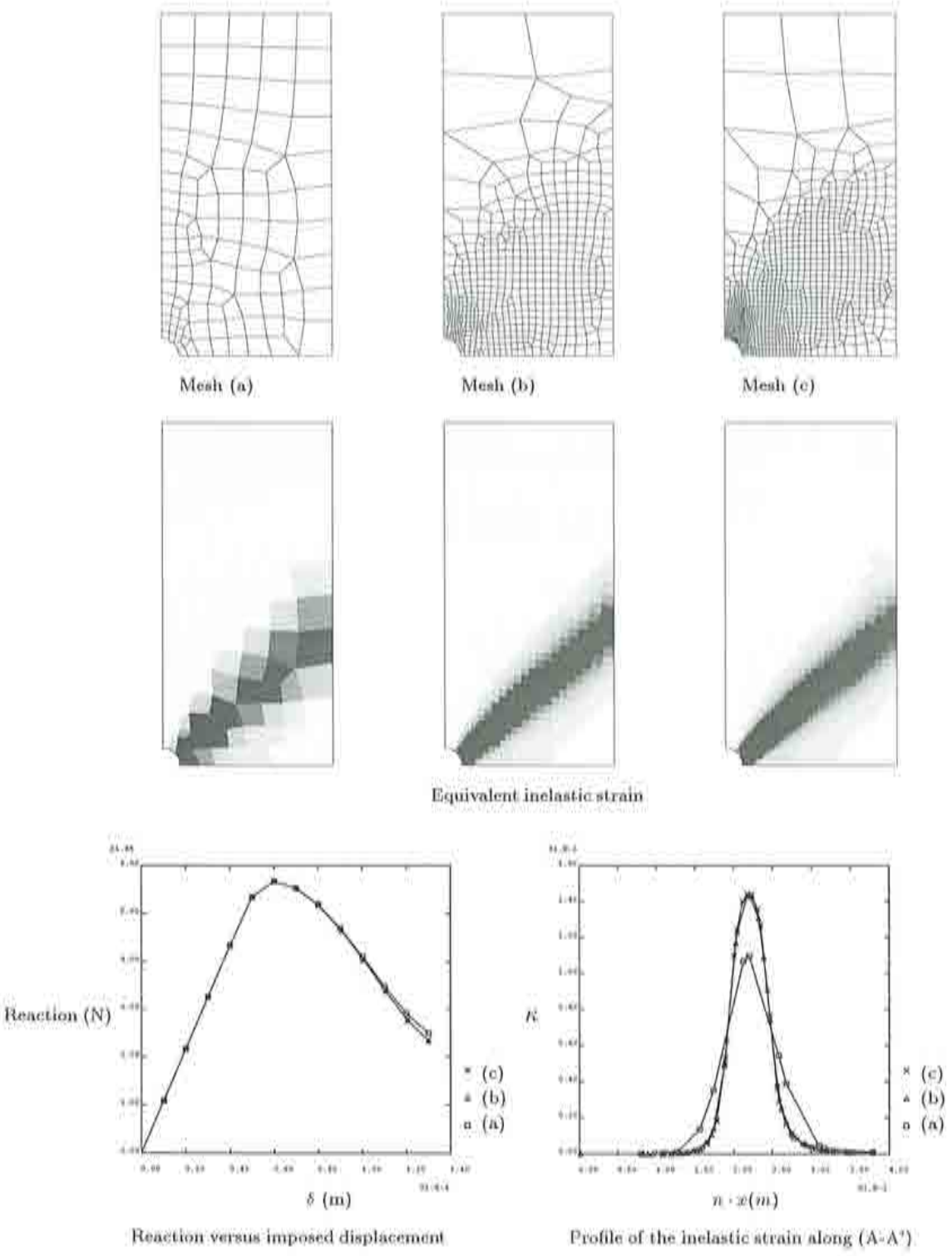

Figure 3.7: Mesh objective results for the reference example

3.5 Influence of several parameters on the band width

The current section analyses the influence of several parameters on the solution, focusing on the band width. As it has been said, the shear band width or the scale of the localised area is a very important feature in this kind of problems. In this section, there are several references to conclusions reached in the appendix A, specially when the influence of the rate effects and of the parameter of Perzyna model N is discussed.

3.5.1 Influence of the imperfection size

As it has been said, the imperfections, often used to trigger localisation, seem to affect the band width in certain cases. According to [33], which deals with this topic in transient two dimensional problems, the influence of the imperfection size can be summarised saying that

- The imperfection size dominates the width of the shear band when the material length scale is larger than the imperfect zone.
- The material length scale equals the width of the shear band if the imperfection size is larger.
- The influence of the imperfection decreases when the shear band is some distance away from the imperfect zone.

As it is shown in the following, these results are also found in the quasi-static case. Here, the reference problem is compared with two analogous problems with different imperfection sizes, $2R$ and $\frac{R}{2}$. The results are presented in figure 3.8. The examlpe with $\frac{R}{2}$ is also presented in a further loading stage ($\delta = 0.19$ mm).

A first glance at the inelastic strain contours seem to indicate that there is an influence of the imperfection size near the imperfection, when it is small; example (b), with a large imperfection, exhibits a shear band of constant width, while in the other examples the band becomes narrower near the opening. This effect is slight in the reference example (a), and much more evident in the specimen with a small opening. On the other hand, the shear band of example (c) is not as developped as the ones of examples (a) and (b). This is because this specimen is not as weak as the others, and the shear band develops later. Example (d) shows how further imposed displacements lead to a developped shear band.

These conclusions are in agreement with the profiles of the inelastic strain along (A-A') and (B-B') represented for examples (a), (b) and (c). The profile along (A-A'), far away from the imperfection, shows that the band width is the same for the three examples with different imperfection sizes. Recall that the localisation size is set in the initial stages of the localisation process (see section 3.3), and consequently the value of the maximum inelastic strain does not affect the band width. On the contrary, the profiles along (B-B') show that near the opening, the band width of example (c) is clearly narrower than the one of the other examples.

The shear band width of example (b), which is uniform and not affected by the large imperfection, can be considered as the material length scale that sets the band width. However, the shear band width is also affected by the imperfection size when the imperfection is smaller than the material length scale and near to it. Thus, according to these results, the conclusions reached by [33] for the dynamic case apply also in the quasi-static case.

On the contrary, the results presented show that certain conclusions of [16] and [5] for the one dimensional quasi-static case do not hold in two dimensions. These authors report that the imperfection size scales the band width and is the characteristic length scale of the problem, in the one dimensional quasi-static case. Here, the shear band is not set by the imperfection size, which is not the problem length scale. The imperfection just affects the band width in certain cases.

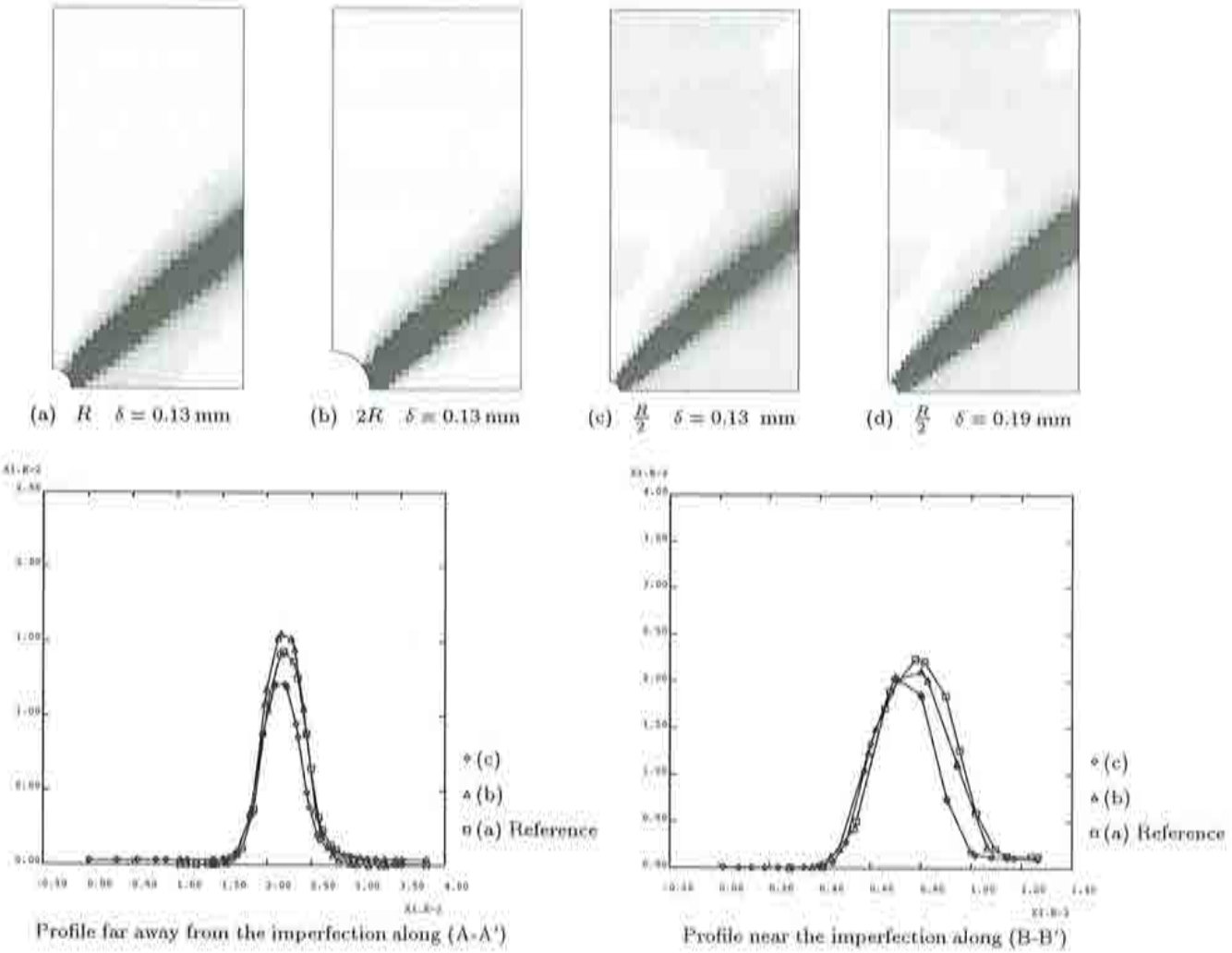

Figure 3.8: Influence of the imperfection size: contours and profiles of the inelastic strain

3.5.2 Influence of the rate effects

The behaviour of Perzyna model when the rate effects are increased or decreased is studied in detail in section A.3. One of the conclusions pointed out is that the rate effects can be enhanced either increasing the loading velocity or decreasing the parameter γ. At the end of section A.2, this parameter is seen as a fluidity parameter. Thus, decreasing γ means enhancing the viscosity effects. In this case, the influence of γ has been studied, but similar results are obtained varying v.

Another relevant aspect pointed out in section A.3 is that the rate independent solid emerges as a limit of the rate dependent solid when rate effects are limited, for instance, increasing γ. Despite this, the rate independent limit is a singular one, and numerical stability problems due to the softening behaviour are observed as this limit is reached. These numerical problems that arise for slightly rate dependent solids are also described by [16].

Figure 3.9 presents the results obtained for the reference example (a) ($\gamma = 500\ s^{-1}$) and those obtained for example (b), in which the rate effects are limited ($\gamma = 5000\ s^{-1}$) and for example (c), in which they are enhanced ($\gamma = 50\ s^{-1}$). It is clear that example (b) tends to the rate independent problem: the band width is narrower than that of the reference example, the residual reaction due to viscous effects is very mild and failure takes place with almost zero energy dissipation (the reaction-displacement curve drops almost to zero very sharply). Nevertheless, the problem is regular, and the results are mesh objective. However, if γ is increased more and more, the band width tends to zero but being finite, and the mesh dependence associated to the coarseness of the mesh becomes increasingly pathological. Thus, the ill-posed problem is reached as a singular limit of well-posed problems.

When rate effects are enhanced (example (c)), the band width becomes so large that it affects the whole specimen. Therefore, the concept of localisation loses its sense and the yielded region spreads all over the domain. That is why the profile of the inelastic strain shows an almost uniform distribution. On the other hand, as the viscous overstress is larger, the maximum reaction obtained is also larger, and the softening branch of the reaction-displacement curve starts later. These results are also found at the constitutive level in section A.3, where the elastic model is found as a limit of viscoplasticity when rate effects are enhanced.

3.5.3 Influence of the parameter N

In the previous section, narrow shear bands have been related to mild rate effects, that is, to a slight regularising effect. However, in the numerical simulation of a real experiment with a certain material, it may be necessary to obtain a narrow shear band, keeping the problem well-posed. The parameter N, an exponent in the viscoplastic flow rule, can be the solution to sharpen localisation maintaining the viscous overstress that regularise the problem.

Section A.5 studies the influence of N at the constitutive level. In order to obtain comparable parameter sets varying N, γ is also modified to get similar viscous overstress.

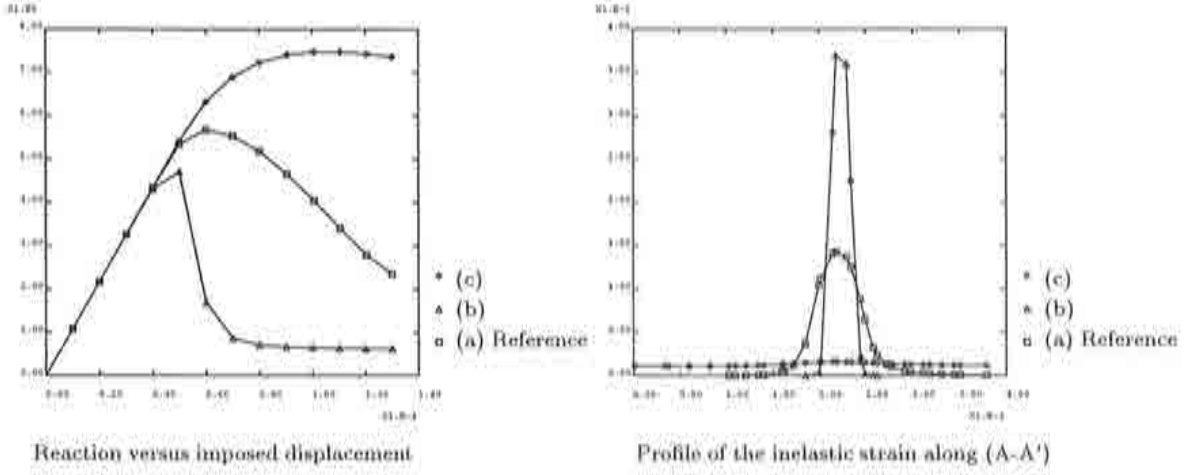

Figure 3.9: Influence of the rate effects

The effect of increasing N keeping the overstress equal to the reference example, is that the transition between the elastic branch and the softening branch is much sharper (see figure A.8). Apart from that, the overstress takes more time to relax than in the reference example.

In this case, the reference example is compared to an example in which $N = 3$ and $\gamma = 17000\ s^{-1}$. The value of γ has been fitted to obtain a similar residual reaction when the shear band is fully yielded. Figure 3.6 shows that this residual reaction is about $1.7 \cdot 10^6$ N for the reference example, and the same value is obtained for the new example (see reaction-displacement curve in figure 3.10). Thus, the regularising effect is maintained. Figure

3.10 shows that the band of example (b) is narrower and, according to the profile of the inelastic strain, much sharper than the reference one. This is obviously related with the observation made in section A.5 reported in the previous paragraph. On the other hand, the global softening behaviour is much more pronounced, although the constitutive softening parameter is the same. Finally, the profile of the Von Mises stress and the yield stress at the end of the process ($\delta = 0.13$ mm), compared to the same plot for the reference example (see figure 3.5), shows that the narrow shear band is much sharper. It also confirms that the overstress relaxes more slowly when N is increased, since the final Von Mises stress distribution is not as uniform as in the reference example.

To sum up, the parameter N, combined with γ, allows to obtain narrow shear bands without decreasing the viscous effects that regularise the problem.

3.6 Concluding remarks

The present chapter has illustrated the necessity of a proper modelling of strain localisation due to material softening, as long as the classical rate independent models lead to meaningless mesh dependent solutions. It has also been shown that Perzyna softening viscoplasticity provides well posed localisation problems in the quasi-static case, that can be solved numerically obtaining mesh objective results. The inception and evolution of the strain localisation phenomenon has also been analysed in detail.

Finally, section 3.5 has showed how the shear band width is affected by several parameters: the imperfection size, the rate effects (γ or v) and the exponent N combined with γ. The influence of the orientation angle of the band has not been studied, but it easy to understand that also affects its width: if the same specimen is brought to failure with imperfections leading to a different band orientation, its width is necessarily different as the shear deformation that it needs to absorb to provide a kinematically admissible failure mechanism depends on the angle.

Despite the qualitative influence of these factors has been studied, the shear band width itself has not been defined nor determined. As a matter of fact, it seems difficult to obtain a simple expression for it, like in dynamics, as long as it depends on parameters of the particular experiment, such as the loading velocity or the band orientation. Thus, in quasi-statics, the internal length emanates from the boundary value problem (governing equations, domain and boundary conditions), and, in particular, it depends strongly on the loading velocity.

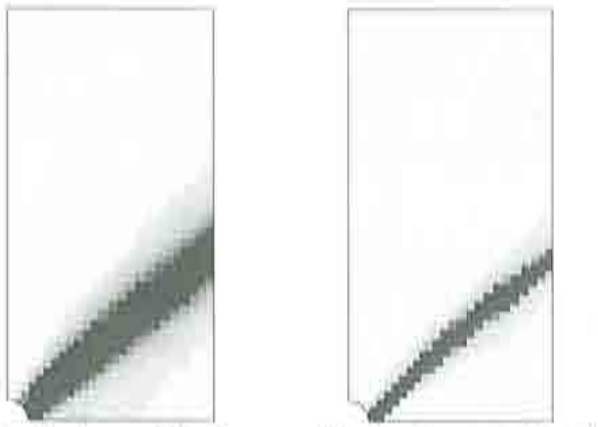

(a) $N = 1 \quad \gamma = 500\ s^{-1}$ (b) $N = 3 \quad \gamma = 17000\ s^{-1}$

Equivalent inelastic strain

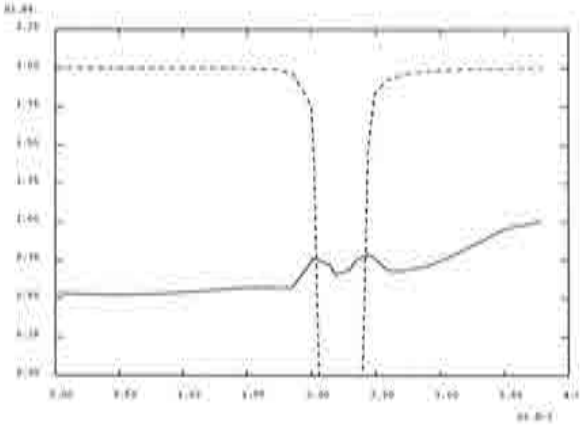

Von Mises stress (solid) and yield stress along (A-A')

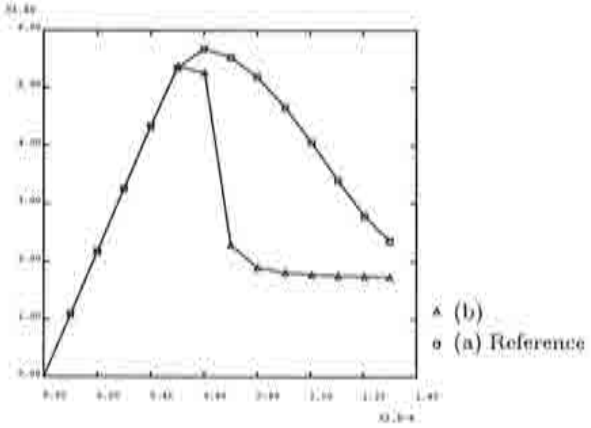

Reaction versus imposed displacement

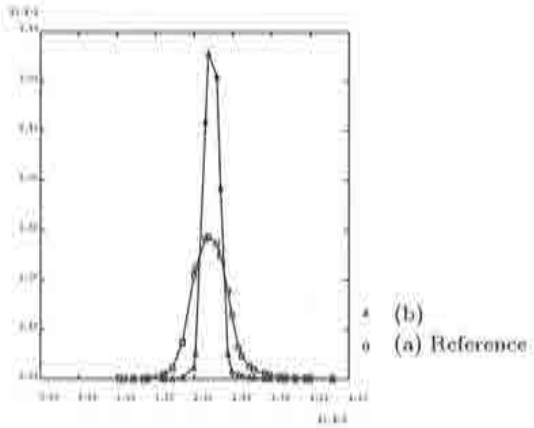

Profile of the inelastic strain along (A-A')

Figure 3.10: Influence of the parameter N

Chapter 4

ADAPTIVITY IN SHEAR BAND LOCALISATION PROBLEMS

In the present chapter, adaptivity based on error estimation is performed in strain localisation problems regularised via viscoplasticity. As it has been said in chapter 3, viscoplasticity provides well-posed problems, whose numerical approximation does not suffer from mesh dependence. It has also been justified that the error estimator for nonlinear problems presented in chapter 2 can be used in such regular problems. Therefore, an adaptive procedure can be used in order to solve the computational difficulties that localisation problems present, that is, the assessment with an affordable cost of the two scales of the problem and the uncertainty in the location of the localisation zone.

Section 4.1 presents the adaptive strategy used in this work, defining clearly the concepts of acceptability criterion and mesh optimality criterion. Then, in section 4.2, several remeshing processes are performed in order to illustrate the performance of the adaptive strategy, that provides objective information about where to put the elements, and how many elements are needed. The influence of the pollution errors is also discussed, as well as the possibility of deducing or testing error indicators using the error estimation. Finally, section 4.2 illustrates the enormous benefits of the adaptive procedure when more complex problems are considered, capturing accurately and cost-effectively the two scales of the problem and the shear band pattern, which is unpredictable a priori.

4.1 Adaptive strategy

4.1.1 Remeshing based on error estimation

As it has been pointed out in section 2.1, the present work performs an h-adaptive procedure based on error estimation. The error estimator presented in chapter 2 accounts for the non-verification of the governing equations, and consequently the procedure presented constitutes an objective analysis. Thus, this approach is not based on heuristic assumptions like other adaptive procedures based on error indicators. The goal of the adaptive remesh-

ing is to obtain a solution of prescribed accuracy with an optimal cost. The concepts of accuracy and optimality are precised later. Figure 2.1 represents schematically the adaptive procedure.

Recall from chapter 1 that there are several adaptive procedures that can be applied to nonlinear problems. Some of them update the discretisation several times (or even every time step) along the process according to some error indicator, such as ALE ([24]), or the mesh refinement procedures presented in [6], [19] and [9]. In these procedures, the successive meshes are built up from the previous ones, either changing the node location, or by element fissions or fusions. This approach seems to be specially well suited for history dependent processes, as long as the mesh is adapted parallely to the time integration. However, important difficulties arise in the transfer of state variables from one mesh to the following one during the loading process. This transfer is generally involved and costly, although ALE solves it naturally. For this reason, the refinement procedures use almost structured meshes, simplifying the refinement and transfer of variables. On the other hand, as long as an ALE procedure does not alter the number of degrees of freedom of the discretisation, it cannot ensure a prescribed accuracy in general.

Other authors suggest procedures in which the domain is remeshed at the end of the loading process, which is recalculated from scratch ([39]). In the present work, the finite element analysis is carried out incrementally to a prescribed load stage for every mesh. Then, the error is estimated. If the solution is considered acceptable according to an acceptability criterion, the adaptive procedure stops. On the contrary, if the acceptability criterion is not verified, the error distribution is used to obtain a desired element size distribution according to an optimality criterion. This element size distribution is the input for the mesh generator to obtain a brand new mesh, and the problem is recalculated. It may be argued that this is not the optimal approach as long as the problem is history dependent and must be recalculated form scratch several times (see [19]). Nevertheless, this procedure avoids the transfer of the state variables, and, as it is shown later, is able to capture phenomena that took place at some point of the history, before the moment when the error is estimated.

4.1.2 Acceptability and optimality criteria

A deep discussion on the existing remeshing strategies is beyond the scope of this work. Several references ([34], [18], [14] and [8]) deal with this topic, the last one presenting them in a unified way. Nevertheless, before the remeshing procedure described above is performed, what is meant here by an acceptable solution (acceptability criterion) and an optimal mesh (optimality criterion) must be clear.

An approximate solution u_h is considered to be acceptable if the norm of the associated error is lower than a specified value. Usually, this specified value is defined as a certain fraction of the norm of the solution, that is, the relative error is prescribed. Thus, the acceptability condition can be expressed as

$$\|e\| \leq \eta \, \|u\|, \tag{4.1}$$

where u is the exact solution, η the maximum relative error, and the error is defined as

$e := u - u_h$. Note that the solution is considered acceptable if the global accuracy is below a certain limit, but no requirements on the local accuracy over the domain are imposed. Thus, a local acceptability criterion based on a prescribed local accuracy can be defined. However, this local condition is too restrictive and leads to meshes of too many elements. Nevertheless, this idea of local accuracy is used by the Local Optimality criterion presented below.

The mesh optimality criteria are usually based on the equidistribution of some measure of the error in the elements of the new mesh. In [18] for instance, this error quantity is the density of error, that is, the error divided by the measure of the element. In this work, the two optimality criteria presented below are used.

Li-Bettess optimality criterion (LB)

According to this optimality criterion (see [14]), the error distribution is uniform in the optimal mesh. Thus, if $\hat{\cdot}$ refers to the new mesh, the quantity that must be set uniform over the new mesh is $\|\hat{e}\|_{\hat{k}}$. Combining this optimality criterion with the acceptability criterion, a distribution of the desired element size $\hat{h}_k$ over the actual mesh can be obtained, providing the input for the mesh generator.

In [14], the authors prove theoretically that this optimality criterion leads to meshes with the minimum number of elements, satisfying an acceptability criterion like the one in equation 4.1. Therefore, acceptable meshes based on this criterion are better, from the computational point of view, than any other acceptable mesh based on another optimality criterion.

Local Optimality criterion (LO)

In numerical analysis, the accuracy of an approximation is related to the relative error. In fact, the acceptability criterion specifies a maximum relative error of the approximation in global terms. However, the Li-Bettess optimality criterion uniformises the distribution of an absolute error. Therefore, a different optimality criterion based on the local relative error can be defined (see [8]). Thus, the optimal mesh can be considered to be that of uniform relative error distribution, that is, uniform accuracy distribution. The Local Optimality criterion tries to set

$$\|\hat{e}\|_{\hat{k}} = \eta_L \|u\|_{\hat{k}} \tag{4.2}$$

in all the elements, being η_L the prescribed relative error. Note that, as long as equation 4.2 is an optimality criterion, it is expressed in terms of an equality and not an inequality.

However, if equation 4.2 is used as the optimality criterion, numerical problems arise where the local norm of the solution is close to zero. This is the usual drawback of relative errors (see [11]). The standard solution of this kind of problem is to add an absolute component to the local measure of the solution. Thus, the optimal mesh can be that in which

$$\|\hat{e}\|_{\hat{k}}^2 = \eta_L^2 \|u\|_{\hat{k}}^2 + \eta_A^2 \frac{\|u\|^2 \Omega_{\hat{k}}}{\Omega} \tag{4.3}$$

in all the elements, being Ω_k and Ω the element and the domain measures respectively. The coefficients η_L and η_A weigh the relative influence of the local and the absolute component of the norm of u. These coefficients must verify $\eta = \sqrt{\eta_L^2 + \eta_A^2}$ in order to have comparable optimality and acceptability criteria. Here, the η_L and η_A have been chosen so that $\frac{\eta_A}{\eta_L} = 0.75$. With this choice, the Local Optimality criterion can be rewritten as follows

$$\frac{\|\hat{e}\|_k}{\sqrt{\|u\|_k^2 + (0.75)^2 \frac{\|u\|^2 \Omega_k}{\Omega}}} = \eta_L = \frac{\eta}{\sqrt{1 + 0.75^2}}. \tag{4.4}$$

See [8] for more details.

4.1.3 Energetic quantities

All these criteria are formulated in terms of norms of the error and of the solution. The norm of the solution is needed to evaluate the accuracy comparing it to the norm of the error. As it is shown in chapter 2, the error estimator for nonlinear problems in its tangent version provides measures of the estimated error using the tangent energy norm, that is, $\|e\|^2 = a_T(u_h; e, e)$. Recall that this norm can be restricted to each element, obtaining the elementary distribution of the estimated error that is needed in the remeshing procedure. This tangent norm can be used because the error is assumed to be small in front of u_h.

To measure the solution with a comparable norm, an energetic quantity is considered generalising the energy norm of the solution in linear problems. In the linear case, the energy norm of the solution $\|u\|$ can be related to the work done by the internal forces as follows

$$\|u\|^2 = 2\, W_{int} = 2 \int_\Omega \left(\int_{\varepsilon_i}^{\varepsilon_f} \boldsymbol{\sigma} : d\boldsymbol{\varepsilon} \right) d\Omega. \tag{4.5}$$

Therefore, extending this measure of the solution to the nonlinear case, the global and the local norms of the solution adopted in this work are defined as follows

$$\|u\|^2 = 2 \int_\Omega \left(\int_{\varepsilon_i}^{\varepsilon_f} \boldsymbol{\sigma} : d\boldsymbol{\varepsilon} \right) d\Omega \quad \text{and} \quad \|u\|_k^2 = 2 \int_{\Omega_k} \left(\int_{\varepsilon_i}^{\varepsilon_f} \boldsymbol{\sigma} : d\boldsymbol{\varepsilon} \right) d\Omega_k. \tag{4.6}$$

In the following sections, remeshing processes are presented for the Li-Bettess and the Local Optimality criteria. The global acceptability criterion is defined in terms of a prescribed global accuracy. For instance, a prescribed accuracy of 1% means that $\|e\| \leq 0.01\, \|u\|$. Of course, since e and u are unknown, this expression is evaluated using the estimated error and the approximate solution.

4.2 Example 1: Single opening

In this section, several remeshing processes are shown for the reference problem described in section 3.2. Recall the shear band localisation and the mesh objective results for that problem that allow to perform a remeshing process (see figures 3.3 and 3.7). One example using different material parameters ($N = 3$ and $\gamma = 17000\ s^{-1}$) is also considered to obtain narrower shear bands (see figure 3.10). In following examples, different optimality criteria have been used, and the pollution errors (see section 2.5) have been taken into account in some of them. The main goal here is to answer in an objective way to the crucial issues of adaptivity: where to put the elements, and how many elements are needed. Apart from this, the section deals with the relevance of pollution errors in adaptive procedures for localisation problems. Finally, the objective approach used in this work, based on error estimation, is presented as a powerful tool to test the suitability and performance of existing error indicators, which often lack theoretical basis.

4.2.1 Remeshing process with LB criterion and pollution errors

Here, an approximate solution has been considered to be acceptable if the global norm of the error is below the 0.5% of the norm of the solution, defined as it is shown in equation 4.6. A mesh is considered to be optimal acording to the Li-Bettess optimality criterion (uniformity of absolute error in the elements). The pollution errors are taken into account in the error estimation.

It is expectable to find large errors near the localised zone, where the intense deformation takes place, and consequently concentrate the elements in that zone by means of the adaptive procedure. However, this is an heuristic assumption, that seems reasonable but leans on assumptions that may not be exact. On the contrary, the remeshing strategy based on error estimation presented here answers objectively to the question of where the elements must concentrate.

Figure 4.1 shows the successive computational meshes and the absolute estimated error distribution in each of them. To represent the elementary error distribution, a unique scale of greys has been used in all the cases, according to which dark grey represents large errors and bright grey small errors.

The solution obtained for mesh 0 is far from being acceptable, as the global accuracy is 4.07%. The error distribution shows that the error is very large in the lower and right part of the specimen, and the next mesh is created accordingly. Nevertheless, mesh 0 is too coarse to provide precise information for the remeshing, and the resulting mesh, mesh 1, is still unacceptable. Thus, adaptive remeshing is an iterative process that meets its end after several steps. The error associated to mesh 1 is still too high, but has been reduced considerably. The error distribution in this mesh, which presents quite uniform element sizes around the shear band, shows an interesting aspect: the error concentrates on two bands that seem to cover the edges of the strain localisation zone. Consequently, mesh 2 shows a concentration of elements along these two bands. Note that the error distribution is much more uniform for this mesh; recall that the optimality criterion used tends to

equidistribute the absolute error all over the elements. However, a global accuracy of 0.56% is still unacceptable and a new mesh is generated. Until now, the successive meshes have had an increasing number of elements. However, mesh 3 has 647 elements whereas mesh 2 has 713. Despite this reduction, the solution obtained with mesh 3 is acceptable: the global accuracy of the solution is of 0.48%, below the prescribed limit of 0.5%. Thus it can be seen that the adaptive procedure allows to use cheaper meshes to obtain more accurate results, putting smaller elements where they are needed and larger elements where the error is small.

Although mesh 3 is acceptable, a further mesh has been generated in order to illustrate the computational optimality of Li-Bettess criterion. The global error with mesh 4 is slightly higher than the previous one, but still below the prescribed limit. In addition, mesh 4 has less elements (601) than mesh 3, and shows a more uniform error distribution. Therefore, mesh 4 is better than mesh 3 from the computational point of view, both meshes being acceptable. If the remeshing process was repeated several times with Li-Bettess criterion, the resulting mesh would converge to the optimal-cost acceptable mesh, with uniform error distribution.

Thus, this remeshing process provides objective information of where the elements must concentrate. In this case, the mesh must be finer along the edges of the shear band, which is not obvious a priori. In fact, no references on adaptive remeshing in strain localisation problems showing this results have been found. For instance, in [6], a refinement procedure based on error indicators is applied to transient localisation problems regularised via viscoplasticity. In the examples presented in [6], the error indicator distribution seems to be constant in the localised zone. Consequently, the refined meshes do not concentrate elements along the edges of the shear band, and the element size is uniform over the localised zone.

But, should the elements concentrate along the shear band edges in any circumstance? To answer this question, another example has been considered. In section 3.5, a new parameter set comparable to the reference example is presented. This new parameter set, characterised by the material parameters $N = 3$ and $\gamma = 17000\ s^{-1}$, shows narrower shear bands, but the viscous effects are not reduced (see figure 3.10). A remeshing process using Li-Bettess criterion and considering pollution errors is presented for this example, prescribing a global accuracy of 2%. The initial mesh is mesh 0 in figure 4.1.

Figure 4.2 illustrates firstly the numerical solution for this parameter set. The mesh deformation amplified 20 times and the contours of the equivalent inelastic strain extended to the whole domain show understandingly the failure mechanism and the shear band pattern in this case. Then the succession of meshes is presented, ending up in mesh 4. This mesh provides a global accuracy of 1.9%, below the prescribed limit, and is consequently acceptable. Note that it is difficult to distinguish the element concentration along the borders of the shear band in the final mesh. This concentration is not even noticeable in mesh 3, which would be acceptable if the prescribed accuracy was of 2.5%. Thus, when the band is narrow or the solution desired is not too accurate, the two bands of element concentration can be missed. In any case, the procedure provides an objective analysis that tells where to

remesh. Obviously, the resulting mesh depends on the level of accuracy prescribed by the user.

Finally, it is also worth mentioning that in this example, the prescribed accuracy (2%) is much lower than in the previous one (0.5%). Despite this, the final mesh here has considerably more elements (842) than the final mesh for the reference example (601). Thus, it seems that the narrow band is more difficult to capture properly. This can be expected in advance, since a narrower band is also associated to a sharper solution with very high gradients of the state variables (see the inelastic strain profiles in figure 4.2), and consequently, requires a richer interpolation.

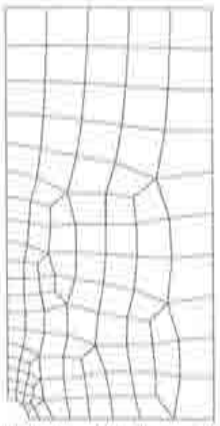


Mesh 0; 110 elements; global accuracy: 4.07%

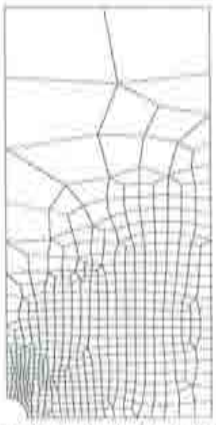


Mesh 1; 580 elements; global accuracy: 1.08%

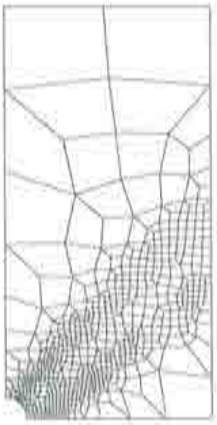
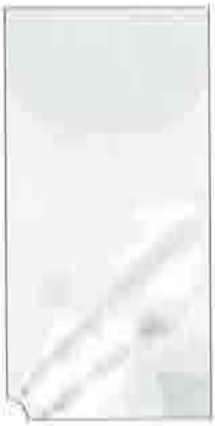

Mesh 2; 713 elements; global accuracy: 0.56%

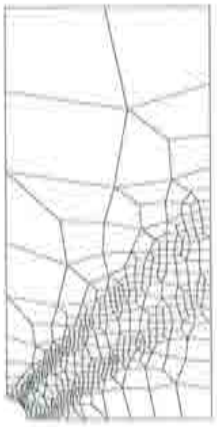


Mesh 3; 647 elements; global accuracy: 0.48%

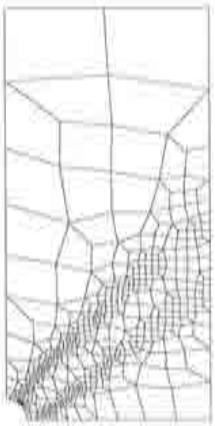

Mesh 4; 601 elements; global accuracy: 0.49%

Figure 4.1: Remeshing process using Li-Bettess and considering pollution errors for a prescribed accuracy of 0.5%: succession of meshes and estimated error distributions

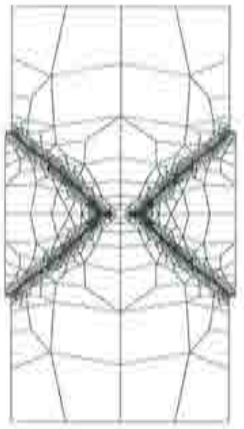

Mesh deformation amplified 20 times

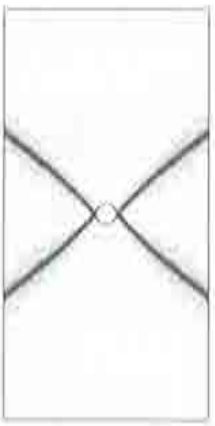

Equivalent inelastic strain

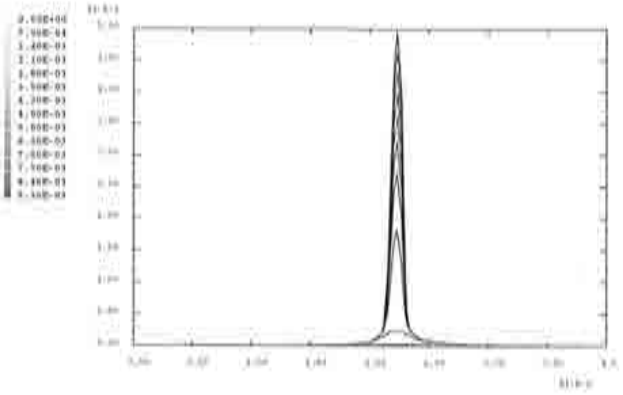

Evolution of the inelastic strain across the shear band

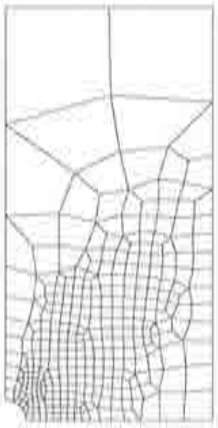

Mesh 1
333 elements
Global accuracy: 3.47%

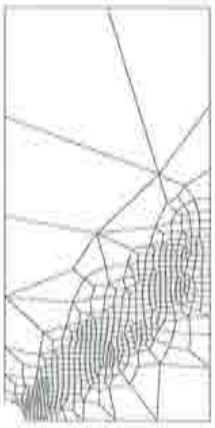

Mesh 2
574 elements
Global accuracy: 2.79%

Mesh 3
680 elements
Global accuracy: 2.42%

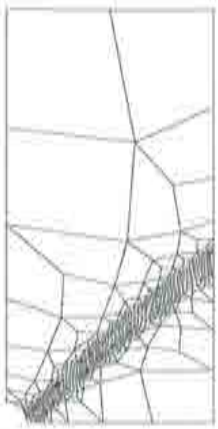

Mesh 4
842 elements
Global accuracy: 1.90%

Figure 4.2: Numerical solution for the example with $N = 3$ and $\gamma = 17000\ s^{-1}$ and remeshing process with Li-Bettess and pollution errors for a prescribed accuracy of 2%

4.2.2 Remeshing process with LO criterion and pollution errors

The remeshing process carried out above for the reference example can also be done using the local optimality criterion, that tends to uniformise the accuracy distribution all over the mesh. Here, the same acceptability criterion has been adopted (prescribed global accuracy of 0.5%) and pollution errors have also been considered.

Figure 4.3 shows the succession of meshes and distributions of the quantity

$$\frac{\|e\|_k}{\sqrt{\|u\|_k^2 + (0.75)^2 \frac{\|u\|^2 \Omega_k}{\Omega}}}. \tag{4.7}$$

This quantity is a relative error modified to prevent numerical problems when the solution is very small, and should be uniform and equal to η_u over the whole domain (see equation 4.4). Therefore, this quantity is representative of the accuracy. Figure 4.3 shows also the final mesh obtained with Li-Bettess optimality criterion and its accuracy distribution, in order to compare the two optimality criteria.

The first thing that strikes the attention is that in this case, an acceptable solution is obtained in the third mesh, whereas Li-Bettess needs five meshes. In addition, the global accuracy in the final mesh (0.25%) is far below the prescribed limit (0.5%). Thus is seems that the Local Optimality criteria is more restrictive than the global acceptability condition. As before, the figure shows clearly that the quantity that is aimed to be uniform, here, the accuracy, tends to uniformity in the remeshing process. In addition, the figure shows that the accuracy distribution in the final mesh obtained with the Li-Bettess criterion, which uniformises the absolute error, is not as uniform as that in LO mesh 2. Indeed, the Li-Bettess final mesh leads to a poor accuracy near the opening.

Note that the final meshes with the two optimality criteria concentrate the elements along the edges of the shear band. In plain words, both remeshing processes put the elements in the same place. Thus, the qualitative issue of where to remesh is readily answered. The important issue here is of quantitative nature; how many elements are needed? Obviously, this depends on the prescribed global accuracy. This aspect has been discussed briefly with regard to figure 4.2. However, the most relevant aspect is that, for a given global prescribed accuracy, depending on the optimality criterion used the relative mesh density over the domain is completely different. For instance, the final mesh for LO criterion has bigger elements than the LB mesh at the top of the specimen and in the bottom right corner, where the solution is small. In the right side of the band, the element sizes are comparable, whereas near the opening, where the norm of the solution (internal work) is very large, the LO mesh has considerably smaller elements.

Thus, the quantitative information about how many elements are needed in every part of the domain is also furnished objectively by the adaptive procedure presented; the precise element size distribution depends of what the user considers an acceptable solution and what he or she expects from the optimal mesh, either an optimal-cost solution with uniform error distribution, or a solution of uniform relative error.

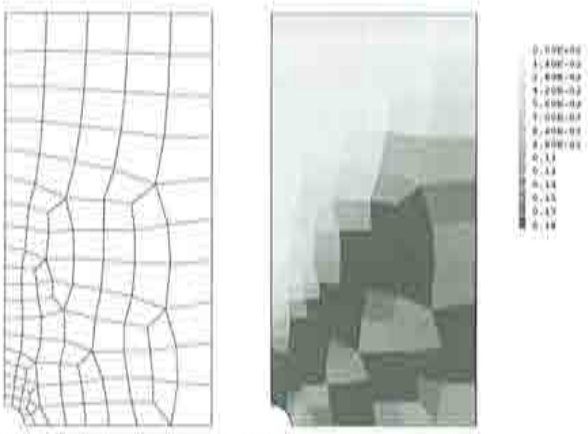

Mesh 0; 110 elements; global accuracy: 4.07%

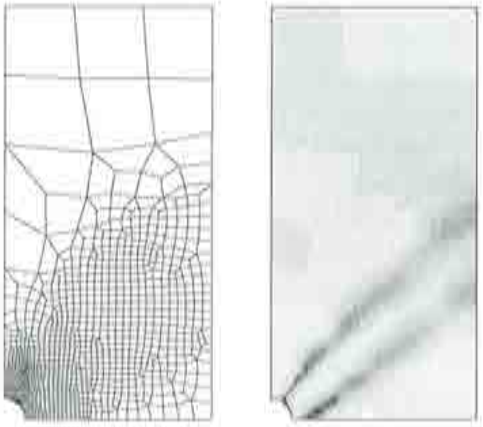

Mesh 1; 1206 elements; global accuracy: 0.64%

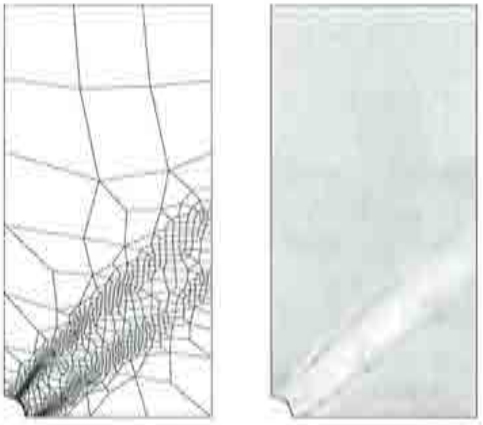

Mesh 2; 1977 elements; global accuracy: 0.25%

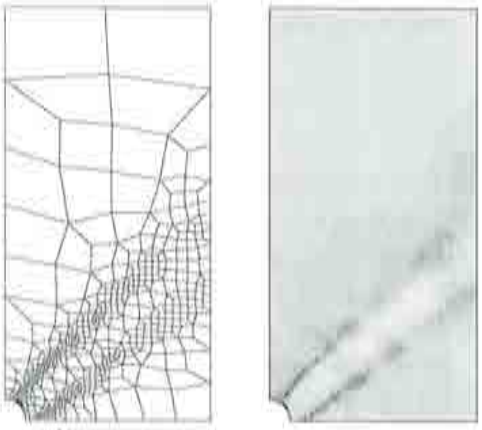

Li-Bettess final mesh and accuracy distribution
601 elements; global accuracy: 0.49%

Figure 4.3: Remeshing process using LO criterion and considering pollution errors for a prescribed accuracy of 0.5%: succession of meshes, accuracy distributions and comparison with LB final mesh

4.2.3 Influence of the pollution errors in the remeshing process

In the adaptive procedure, the error estimator must provide a good approximation of the actual error, but with a reduced computational cost. In the examples presented above, the pollution errors have been considered, so that the total estimate e_T is computed adding properly the local estimate e_L and the global estimate e_G, which accounts for the pollution errors and obviously increases the cost of the estimation (see chapter 2). According to the orthogonality of e_L and e_G, the norm of the total estimate can be computed easily from the norms of the local and the global estimates

$$\|e_T\|^2 = \|e_L\|^2 + \|e_G\|^2. \tag{4.8}$$

This equation is assumed to hold at the elementary level and $\|e_T\|_k$ is computed in the same fashion.

Thus, one question arises: is it important to take into account the pollution errors when adaptive remeshing is performed in localisation problems? Do they have a relevant influence on the meshes or the accuracy obtained? It seems obvious that if their contribution is hardly noticeable, the computational effort that the global estimation requires is not worth being done. The previous remeshing processes have been based on the distribution of $\|e_T\|_k$, and it would be desirable to simply use the distribution of $\|e_L\|_k$.

To answer this question, a coefficient r, expressed in percentage, is defined as the ratio beween the locally estimated error and the total error estimation in which the pollution errors are considered. This coefficient is defined both for the elements and the whole domain, and is expressed as follows

$$r_k = \frac{\|e_L\|_k}{\|e_T\|_k} \cdot 100\% \quad \text{and} \quad r = \frac{\|e_L\|}{\|e_T\|} \cdot 100\%. \tag{4.9}$$

This coefficient, which is obviously lower than 100, is representative of the influence of the pollution errors in the error estimate; the more close is its value to 100, the more negligible are the pollution errors, as remeshing according to $\|e_T\|$ or to $\|e_L\|$ is practically identical.

Figure 4.4 shows the elementary distribution of r_k as well as the global value r, in the succession of meshes presented in the beginning of the section (Li-Bettess criterion and a prescribed accuracy of 0.5% for the reference example). The same scale has been used in all the plots, and goes from the 87% (brighter) to the 100% (darker). First of all, it is remarkable that the global value, r, is almost constant for all the meshes, and takes values greater than 98%. Therefore, the global influence of the pollution errors in the estimation does not vary when the mesh is refined, and is very small. The distribution of r_k also brings interesting results. It can be noticed that in the first plots, the presence of bright grey is quite important. This means that in a considerable part of the specimen r_k is below 87%, and the influence of the pollution errors is noticeable. However, as the meshes are refined, the most part of the specimen is darker, which means that r_k is greater than 95% in practically all the domain. Thus, these results seem to indicate that the pollution errors become negligible as soon as the mesh is refined, which agrees with the theoretical results

reported in [32]. In conclusion, it seems that the computation of the pollution errors can be avoided in an adaptive process, which indeed refines the meshes. It is expectable to find little differences between the acceptable meshes considering pollution errors or not.

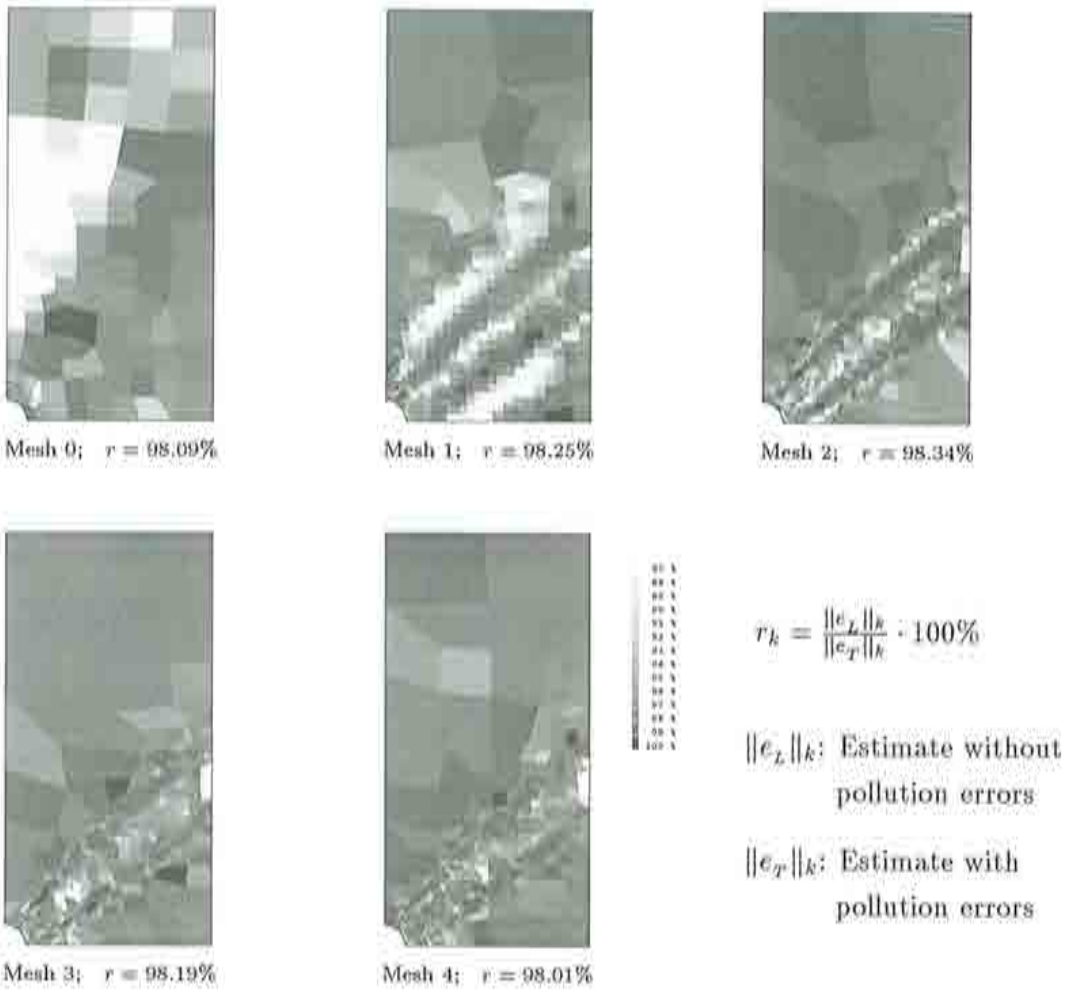

Figure 4.4: Influence the pollution errors: distribution of r_k for the succession of meshes with Li-Bettess criterion and considering pollution errors for a prescribed accuracy of 0.5%

To illustrate these conclusions, figure 4.5 shows the successive meshes of a remeshing process based on Li-Bettess criterion for a prescribed accuracy of 0.5%. In fact, the only difference between this example and the one showed in figure 4.1 is that now pollution errors are negliged. The final mesh obtained considering pollution errors is also presented to provide a better comparison. Note that the initial mesh provides a global accuracy of 3.99% in this case, while its accuracy considering pollution errors is of 4.07%. This disagreement can be readily understood recalling that, for this mesh, $r = 98\%$. So, negliging e_a implies

a very slight underestimation of the error.

In more general terms, the tendency of the remeshing process described in figure 4.1 is also noticed here, and the obtained meshes are very similar. Indeed, there are no major differences between the two final meshes, which are difficult to distinguish. Thus, in this kind of problems, the pollution errors can be negliged without affecting noticeably the resulting mesh or the level of accuracy of the final solution.

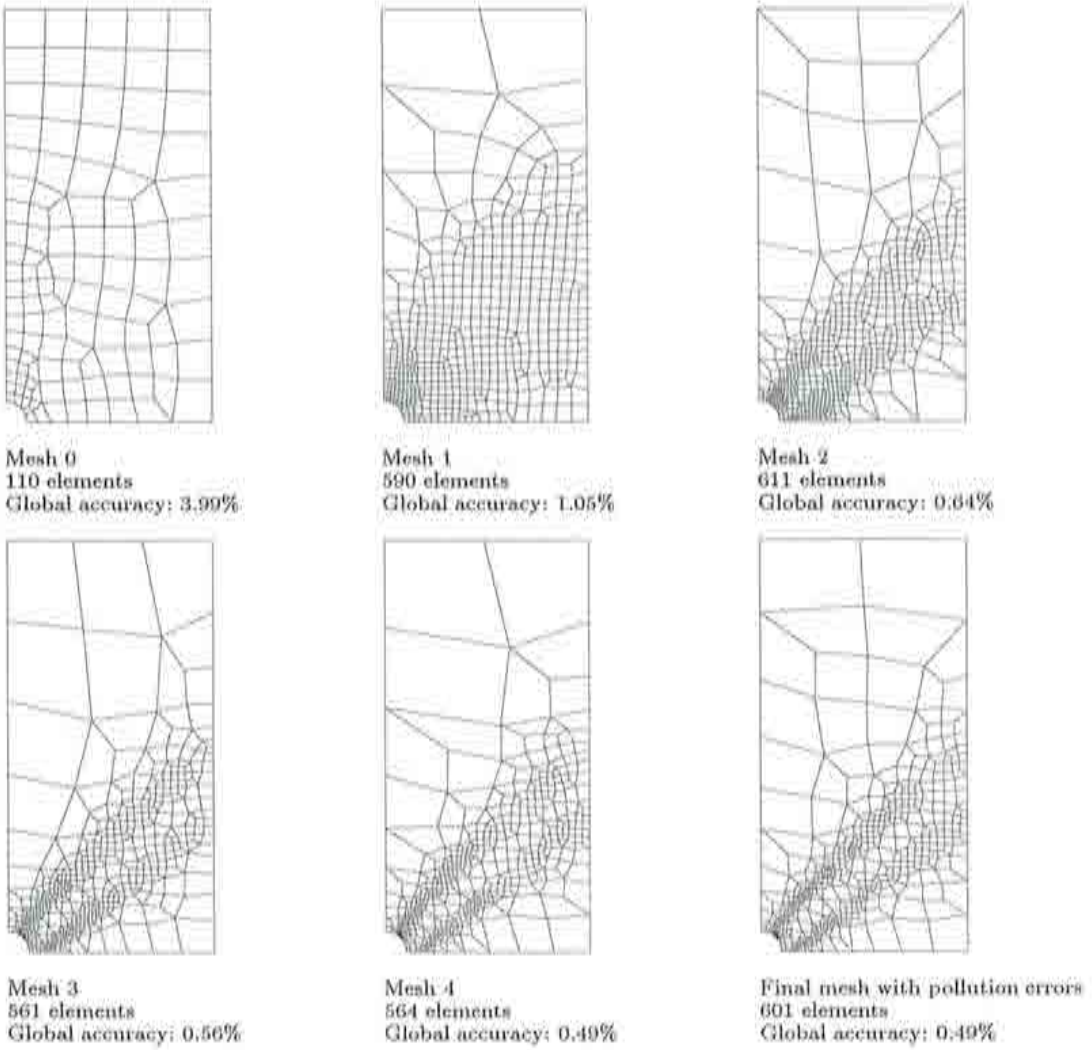

Figure 4.5: Remeshing process using Li-Bettess criterion, without pollution errors, for a prescribed accuracy of 0.5%

4.2.4 Test of error indicators

Once the adaptive procedure presented has furnished the final mesh, the element size distribution can be easily correlated to physical magnitudes of the problem, obtaining a posteriori qualitative information about the optimal discretisation. This information can be useful to deduce good error indicators for this kind of problem.

As it has been said in chapter 2, the error indicators constitute a cheap alternative to error estimators. However, these indicators often lack theoretical basis and are purely heuristic. References [39], [20], [6], [9], [19] and [24] provide a wide range of error indicators based on interpolation errors, on velocity variations, on the acoustic tensor, on internal variable variations, on L_2-projections of the stress or strain fields, etc.

In this context, the objective approach presented in this work can be useful to deduce, but also to test existing error indicators; their suitability (do they answer correctly to the question, where the elements must be?) and performance (do they put the correct density of elements?) can be studied from the results obtained with the presented adaptive procedure.

The results shown in figures 4.1 and 4.3 indicate that small elements concentrate along the edges of the shear band, instead of concentrating where the higher strains are reached, that is in the centre of the shear band. Therefore, it is natural to expect the small elements to concentrate where large variations of the inelastic strains occur, that is where the modulus of its gradient is high (note that the inelastic strain and the total strain are almost equal in the localised zone where the inelastic strain is very high). Figure 4.6 shows that, in effect, a correlation can be made between the element size and the inelastic strain gradient. The upper plot shows profiles of the internal energy, the inelastic strain and the inverse of the element size across the shear band. These profiles have been scaled adequately to be represented in the same plot. It is obvious from this plot that the internal energy and the inelastic strain distributions match almost exactly, and do not indicate where the elements must be. The lower plot represents the profile of the inverse of the element size, and the profile of the modulus of the gradient of the inelastic strain. This plot shows clearly that the elements are smaller where large variations of the inelastic strain occur. Thus, a fairly good correlation can be established between the element size and the derivate of the inelastic strain, and also the derivate of the internal energy. The colour plots show that the modulus of the gradient of these two physical variables describes very well the element sizes, bright grey corresponding to large elements and dark grey to small ones. As a matter of fact, the use of the variations of the internal variable of the problem (in this case, the equivalent inelastic strain) is used as the error indicator in [24], where Mazars nonlocal model is considered. Other authors also consider indicators based on the energy consumption (see [9]).

It is important to keep in mind that these correlations only apply for this particular problem. In addition, the computation of derivates of, say, the inelastic strain, which is a discontinuous field, shows very poor accuracy and depends stongly on the mesh size: a finer mesh gives higher values of the gradients. In [6], an error indicator based on an L_2-projection of the strains is presented, the Strain Projection (SP) indicator. According to [9], this indicator is an indirect measure of the strain gradients, and consequently, should

be a suitable error indicator for the problems studied here. The SP indicator measures the jumps of the strain field comparing the discontinuous finite element solution for the strains, ε^h, with a smoothed field, $\bar{\varepsilon}$

$$e_i^{SP} = \left[\left\{ \int_{\Omega_i} (\bar{\varepsilon} - \varepsilon^h)^T (\bar{\varepsilon} - \varepsilon^h) d\Omega \right\} / \Omega_i \right]^{1/2}. \tag{4.10}$$

$\bar{\varepsilon}$ is evaluated by an usual L_2-projection using a lumped mass matrix. In [6], this error indicator is taken as a magnitude that has to be set uniform in the adaptive process in a transient localisation problem regularised via viscoplasticity.

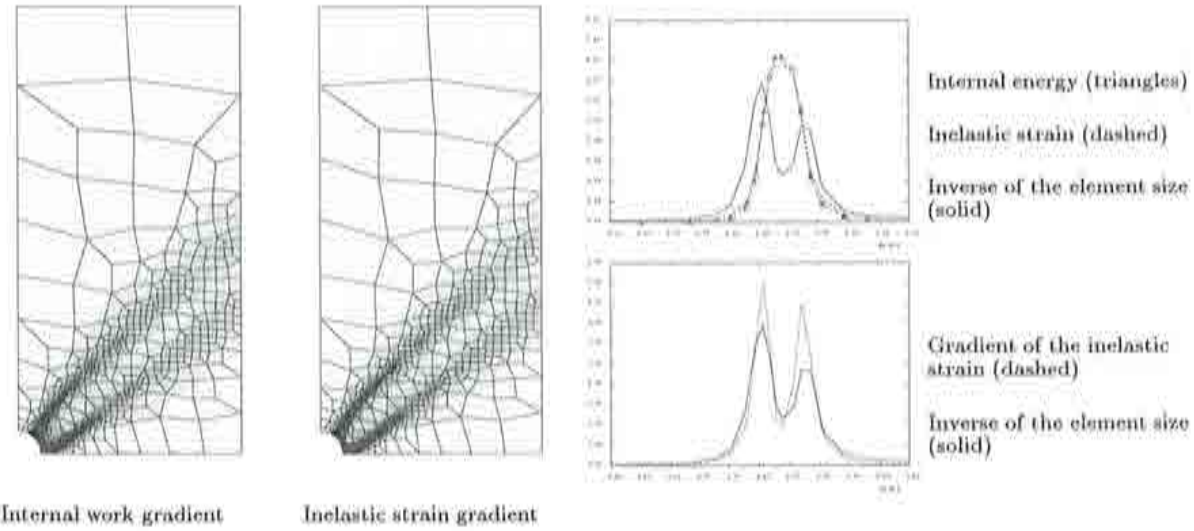

Figure 4.6: Correlations between physical magnitudes and the element size

To test the suitability and performance of the SP indicator in the quasi-static problems considered here, the estimated error and the indicator distributions have been represented as surfaces in meshes 1 and 4 of the Li-Bettess remeshing process presented in figure 4.1. These plots are shown in figure 4.7. It is clear that the error estimator detects large errors with mesh 1, which is quite uniform, along the two edges of the shear band, and the mesh is consequently refined in these zones. As expected, the error distribution in the final mesh, represented in the same scale, is quite uniform and much lower. The figure shows that the SP indicator also detects large errors along the shear band edges in mesh 1. However, this surface shows a very important peak near the opening, and indicates very large errors where the error estimator does not. In mesh 4, the SP indicator distribution is quite uniform and small over the domain, except near the opening where the indicator still shows very high values. In fact, this peak in the indicator, that measures indirectly the strain gradients, is in agreement with the inelastic strain gradient distribution plotted in figure 4.6; near the opening, between the two bands of small elements, very high gradients are computed (dark grey) whereas the elements are quite large.

Thus, it seems that an indicator measuring the variations of the strain field would put very small elements near the opening, where the strain gradient is very large. However, the actual error (the estimated error) is not very large in this zone, and larger elements are enough according to the objective approach. Therefore, the SP indicator would refine correctly in the edges of the shear band, but would also refine far too much near the opening, leading to very expensive meshes for a given accuracy. In conclusion, it can be said from these results that the SP indicator is suitable (the edges of the band are refined) but shows a poor performance (it refines too much near the opening).

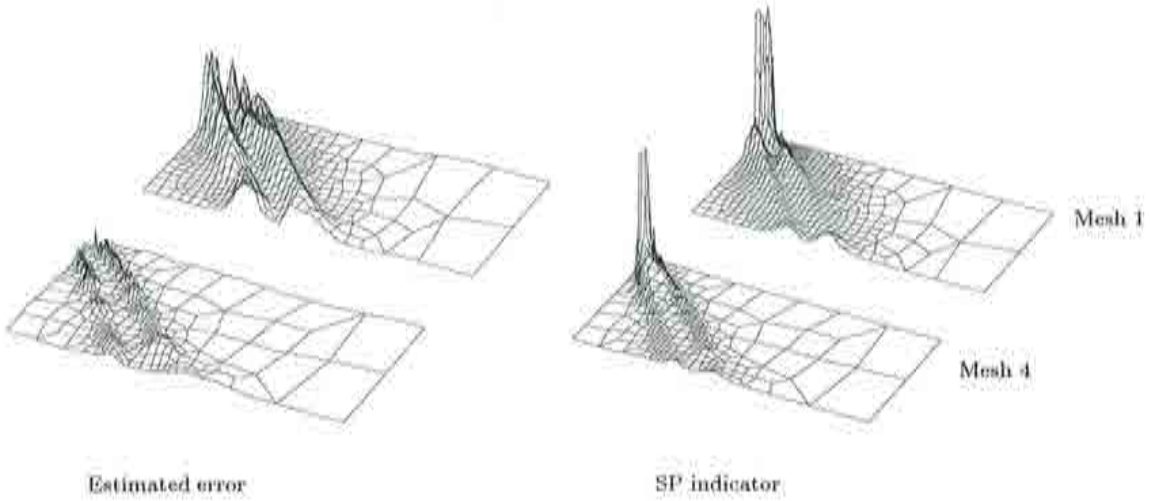

Figure 4.7: Surfaces of the estimated error and of the SP indicator in meshes 1 and 4 of the Li-Bettess remeshing process

Of course, the results presented here are not exhaustive and their aim is to present the objective error estimation analysis as a powerful tool in the study of error indicators. Further work can be carried out, studying other indicators, and the underlaying optimality criterion implicit in the indicators: here, the SP indicator has been studied using a Li-Bettess remeshing process, but the conclusions may be different if other optimality criteria are considered.

4.3 Example 2: two openings

The objective of this section is to make clear that the use of an adaptive technique is almost unavoidable in more complex and realistic localisation problems, providing accurate and cost-effective solutions. To do this, a more complex geometry with two circular openings is considered. Two slightly different specimens are brought to failure, and the results are analysed.

The aim here is not to study the different remeshing strategies or the error estimation, as has been done in section 4.2 with a simple problem. Therefore, in the two examples shown in the present section, the same optimality criterion (Li-Bettess) is used. This choice obeys to its computational optimality, as long as more than 6000 degrees of freedom are reached here. A solution is considered to be acceptable if the global relative error is below 1.5%. Finally, according to the conclusions reached in the previous section, the pollution errors are not considered.

4.3.1 Problem description

The only difference between the problems considered in the current section and the reference example decribed in figure 3.2, stems from the material parameters adopted, and from the imperfections introduced into the specimens. On one hand, the parameter set chosen is the one leading to narrow shear bands presented in figure 3.10, that is, $N = 3$ and $\gamma = 17000\text{s}^{-1}$. On the other hand, two smaller circular openings substitute the centred one on this occasion (see figure 4.8). It is worth remarking also that the maximum imposed displacement in the present examples is $\delta_{max} = 0.1$ mm.

Two slight variations of the geometry of the specimen are considered, depending on the horizontal separation of the openings, which are closer in example 2b. As can be seen in figure 4.8, the geometrical centre of the specimen is a centre of symmetry. Consequently, only one half of the domain is analysed, reducing the computational domain. The boundary condition to be imposed in the bottom of the computational domain is simply a linear constraint on the displacements of this part of the boundary, which must be symmetric with respect to the centre. In practice, this imposes a constraint also on the mesh: the nodes of this line must also be placed symmetrically, so that the boundary condition can be readily implemented. Of course, this has to be taken into account in the remeshing process.

It is worth noting that in all the figures of this section, the solution obtained in the computational domain is extended to the whole domain to make the plots more understanding. However, when the number of elements is given, only the computational mesh is accounted for.

4.3.2 Example 2a: two distant openings

The remeshing process carried out for example 2a is presented in figure 4.9. The successive computational meshes and their symmetric are shown, as well as the absolute error distribution, which is uniformised by Li-Bettess criterion. In this case, five remeshing steps are

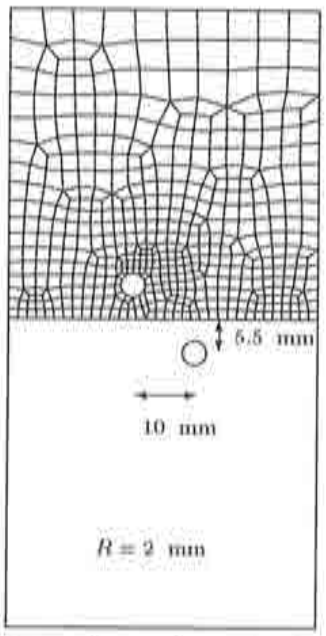

Example 2a: Specimen with two distant circular openings

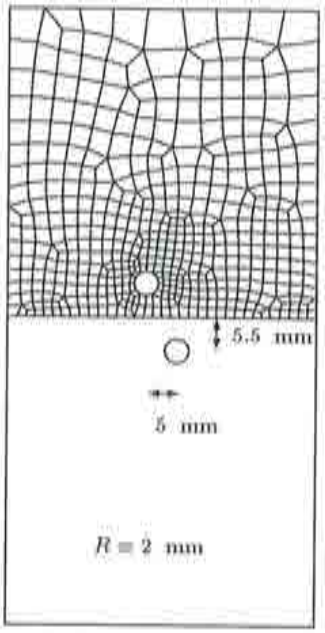

Example 2b: Specimen with two close circular openings

Figure 4.8: Description of the two openings example: geometry and computational domain

necessary to reach the prescribed accuracy. Even if mesh 0 is far too coarse to be acceptable (global accuracy of 6.75%), it detects a zone of intense error in which the shear band is located. In the following meshes, the localised region is detected in more detail by the error estimation, and is progressively refined. The global relative error decreases considerably in every step. At the end of the process, the error distribution is quite uniform, and although the shear band is very narrow, two bands of smaller elements covering its edges can be clearly distinguished.

This example illustrates perfectly the suitability of an adaptive procedure based on error estimation in localisation problems, as well as the good performance of the presented strategy. The remeshing process adapts the discretisation in order to capture the two different scales of this kind of problem, the specimen scale and the localisation scale, which become evident from mesh 5. Thus, the strategy represents an objective, accurate and cost-effective methodology for localisation problems. It seems obvious that the computational cost of a uniform mesh with the element size characteristic of mesh 5 (in the shear band zone) is unaffordable in practical engineering applications.

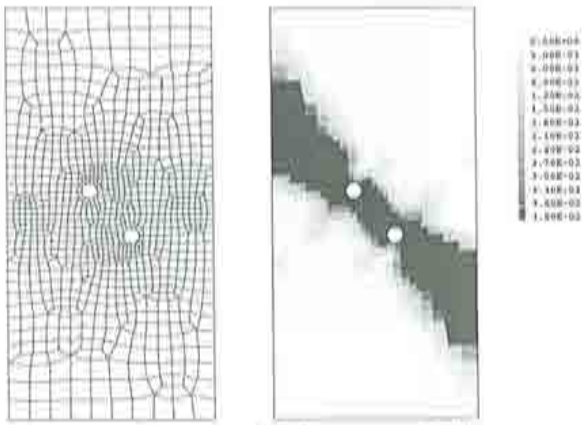

Mesh 0; 470 elements; global accuracy: 6.75%

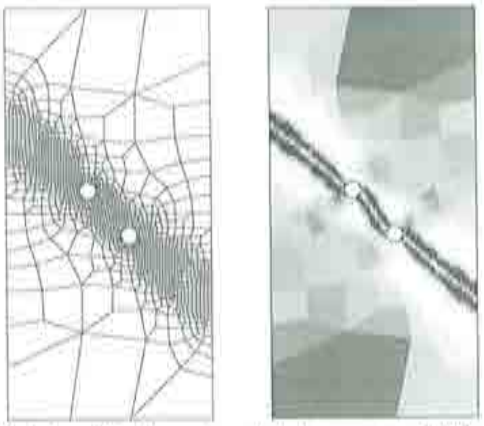

Mesh 1; 781 elements; global accuracy: 3.00%

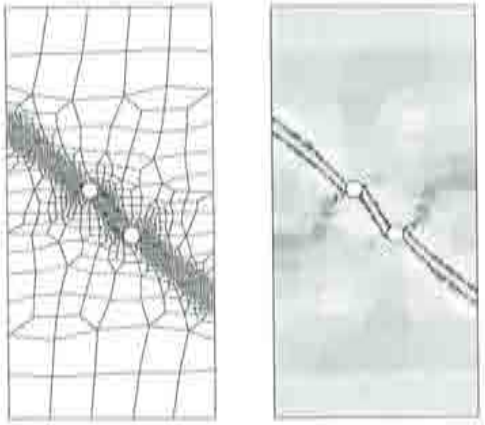

Mesh 2; 899 elements; global accuracy: 2.28%

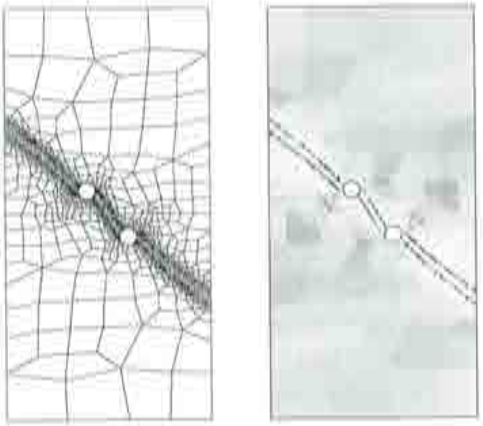

Mesh 3; 1274 elements; global accuracy: 1.97%

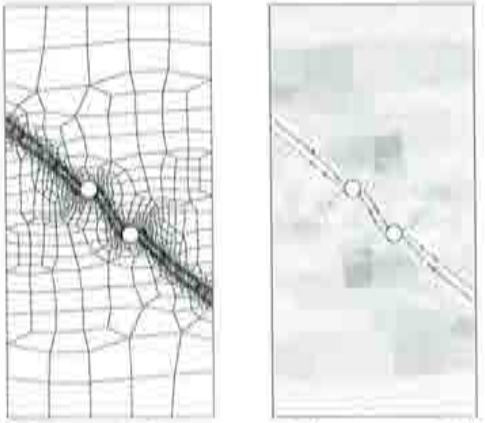

Mesh 4; 1660 elements; global accuracy: 1.62%

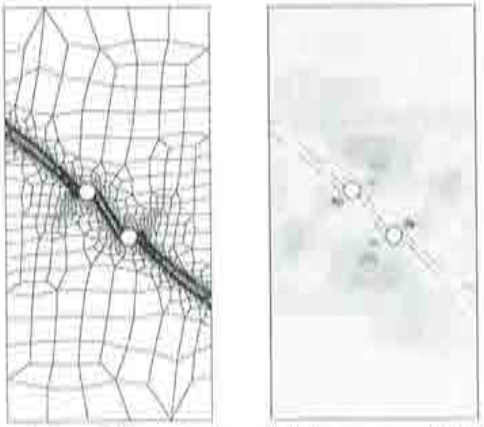

Mesh 5; 1888 elements; global accuracy: 1.35%

Figure 4.9: Remeshing process using Li-Bettess for a prescribed accuracy of 1.5%: succession of meshes and estimated error distributions

Figure 4.10 shows the numerical solution obtained for this problem: the reaction versus displacement curve, the mesh deformed and the equivalent inelastic contours for meshes 0 and 5. The failure mechanism obtained is quite expectable, since the two openings are almost aligned in the direction of the natural shear band orientation (see [30]). Therefore, the three shear bands obtained (from the left side of the specimen to one opening, between the two openings and from the second opening to the right side) constitute practically a unique surface along which the upper part of the specimen slides with respect to the lower part. Note that, although mesh 0 is very coarse and scarcely accurate, it describes the correct shear band pattern (see figure 4.10). Therefore, the remeshing process starts in the right direction, and the successive meshes develop the same failure mechanism with increasing accuracy. This aspect is relevant to analyse example 2b.

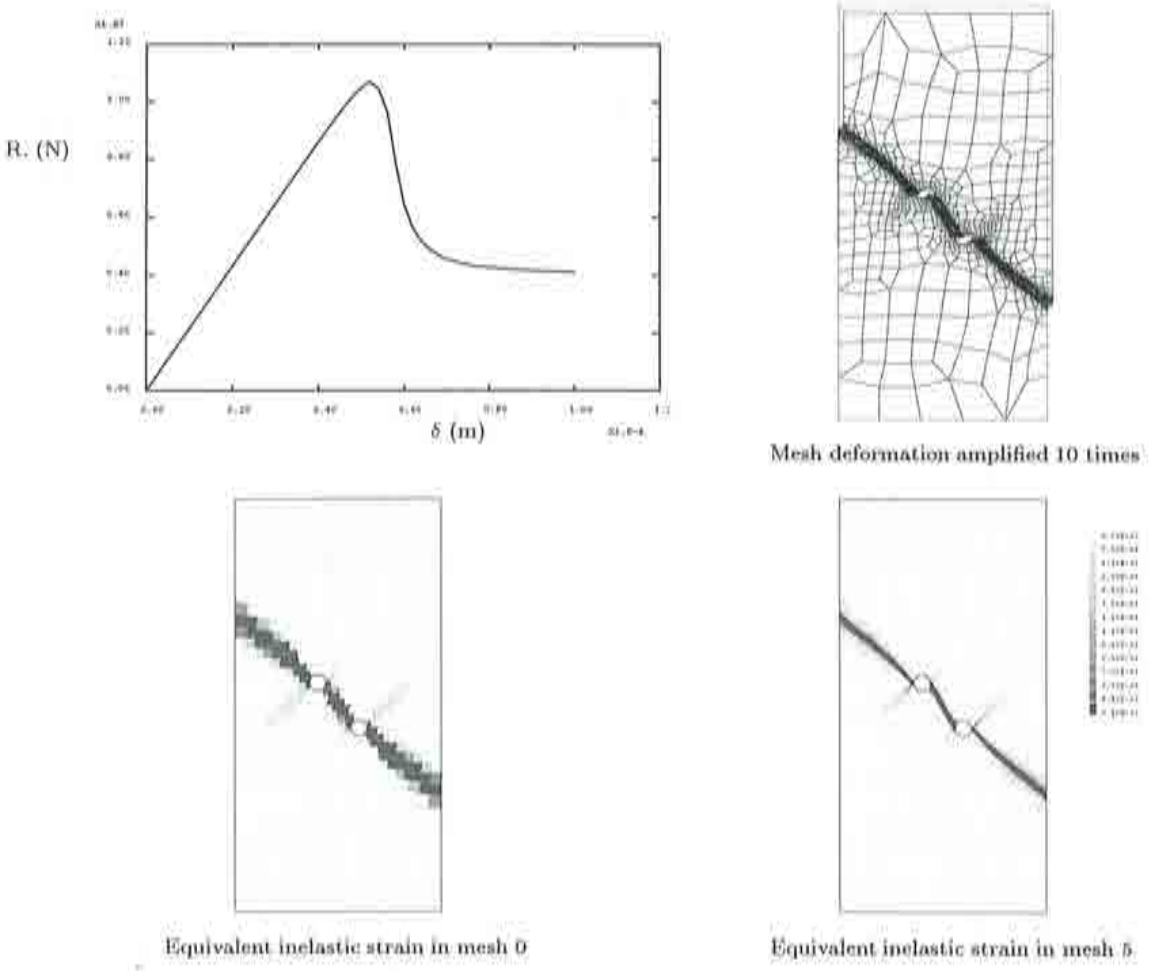

Figure 4.10: General solution for example 2a: Reaction versus imposed displacement, deformation of mesh 5 and inelastic strain contours for meshes 0 and 5

4.3.3 Example 2b: two close openings

Remeshing process

In this case, the remeshing process is performed for a slight different geometry to that of example 2a. Figure 4.11 presents the process. Again, six meshes are necessary. However, note that the global relative error is hardly reduced in the first two steps: it is of 4.99% in mesh 0, of 4.00% in mesh 1 and of 3.96% in mesh 2. Furthermore, meshes 1 and 2 detect high errors in zones where small errors are assessed with mesh 0. Recall that in example 2a the initial mesh captures the zone where remeshing is needed, despite its coarseness. In the present case, however, the error estimation obtained with the initial mesh fails to indicate where the elements must concentrate (see mesh 5).

To understand why this happens, figure 4.12 represents the mesh deformation, the inelastic strain contours and the reaction-displacement curve obtained at the end of the loading process, for meshes 0, 1, 2 and 3. Before the figure is commented, it is important to point out that a shear band is considered to be completely developed if its both ends are on the boundary of the specimen. Indeed, a shear band is not a sliding surface of the failure mechanism until it starts and ends on the boundary.

The figure shows clearly the shear band pattern obtained with mesh 0. Only two completely developed shear bands can be noticed. Two other secondary bands also appear (the shear band that goes from one opening to the other is not considered in the explanation for simplicity). Therefore, the failure mechanism leans mainly on two sliding surfaces. The reaction-displacement curve (in dark grey) shows a softening branch that tends to be horizontal. Very similar results are obtained with mesh 1 for the failure mechanism (see the deformed mesh). However, the secondary shear bands are more developed and almost reach the boundary. The medium grey curve shows that, despite the response for mesh 1 is similar to that of mesh 0, the final part suggests an increasingly sloped softening branch. Then, with mesh 2, a very different solution is obtained, showing four completely developed shear bands and a more complex failure mechanism with four sliding surfaces. Keep in mind that all these results are obtained for the same imposed displacement. The brighter curve exhibits also this different failure response with an intermediate stage in the softening branch, and shows that this solution has less energy than the previous ones (the area under this curve is smaller). In fact, there is a numerical bifurcation between meshes 1 and 2: at a certain point of the loading process, the solution with mesh 1 follows a different path that the solution with mesh 2 (the medium and the bright curves diverge). The results obtained with the meshes 2, 3, 4 and 5 are very similar and approximate properly the unique solution of the boundary problem (recall that viscoplastic regularisation guarantees the uniqueness of the solution). Thus it can be seen that the first two meshes are incapable of reproducing the phenomenon, leading to solutions qualitatively different to the most accurate one. Although the solution is qualitatively dependent on the mesh, the problem does not exhibit a pathological mesh dependence: once the mesh is fine enough, the right mechanism is correctly captured.

Going back to figure 4.11, it is easy now to understand the first steps: since the first

mesh leads to a wrong solution, the error estimation is also biased and the resulting mesh is not refined properly. Therefore, the resulting mesh, mesh 1, also fails to capture the correct response. However, the solution obtained is closer to the correct one, which is finally obtained with mesh 2. In plain words, it can be said that the remeshing process firstly captures the correct mechanism (from mesh 0 to mesh 2), and then converges to the prescribed accuracy (from mesh 3 to mesh 5). In the first phase, as the mesh is refined, new errors are detected, whereas in the second phase, the error distribution is reduced and equidistributed. Recall that in example 2a the shear band pattern is much simpler, and is described correctly by the first mesh.

Finally, note that, as long as the energy (and the norm) of the solution with mesh 2 is lower than the energy obtained with mesh 1, the norm of the error is divided by a smaller quantity when the global accuracy is computed. This can explain partially the fact that doubling the number of elements, the relative errors obtained are practically the same with meshes 1 and 2.

To sum up, this example not only shows that the adaptive procedure captures the two scales of the problem, but also that it locates the localisation zone, which is unknown a priori. In some cases, it is almost unpredictable; a slight difference in the initial geometry leads to completely different solutions in examples 2a and 2b. Furthermore, the adaptive process has shown to be capable of capturing complex mechanisms, even if the initial meshes lead to wrong solutions.

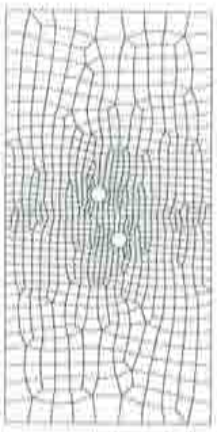

Mesh 0; 462 elements; global accuracy: 4.99%

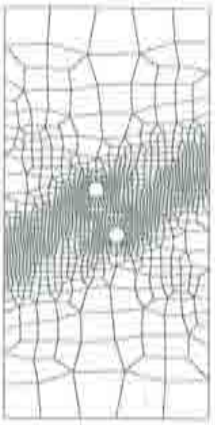


Mesh 1; 856 elements; global accuracy: 4.00%

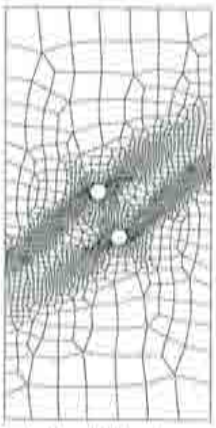
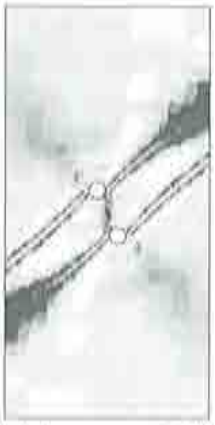

Mesh 2; 1641 elements; global accuracy: 3.96%

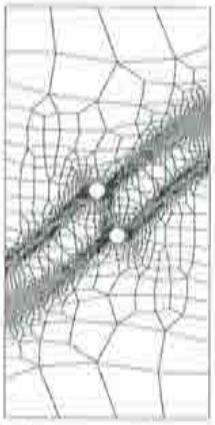


Mesh 3; 2235 elements; global accuracy: 2.31%

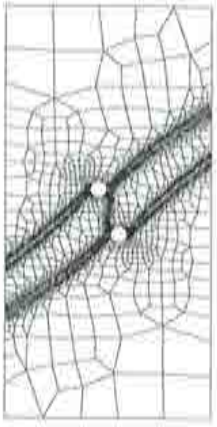


Mesh 4; 3200 elements; global accuracy: 1.73%

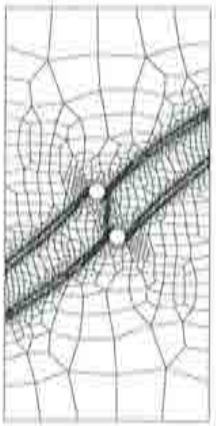


Mesh 5; 3307 elements; global accuracy: 1.49%

Figure 4.11: Remeshing process using Li-Bettess for a prescribed accuracy of 1.5%: succession of meshes and estimated error distributions

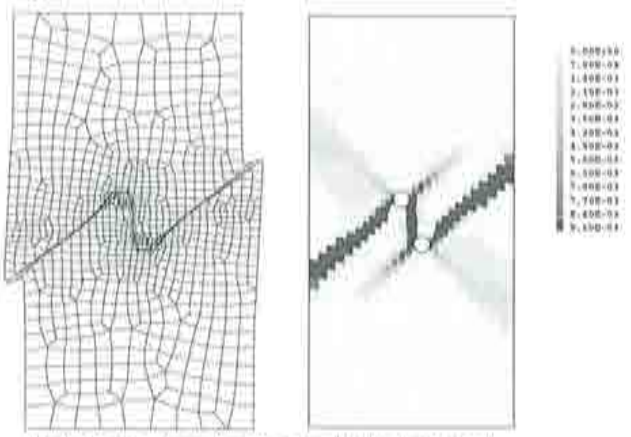

Mesh 0; two shear bands completely developed

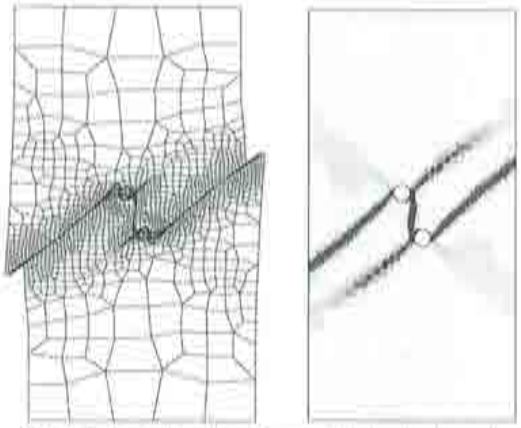

Mesh 1; two shear bands completely developed

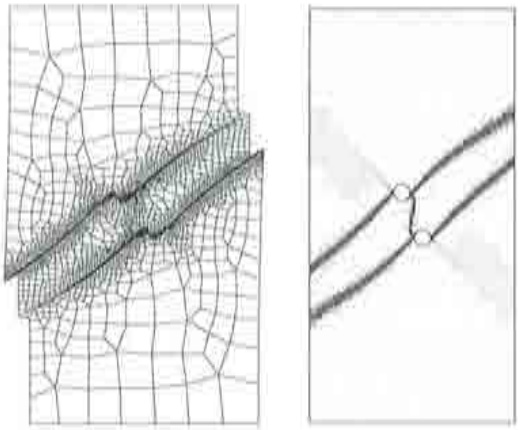

Mesh 2; four shear bands completely developed

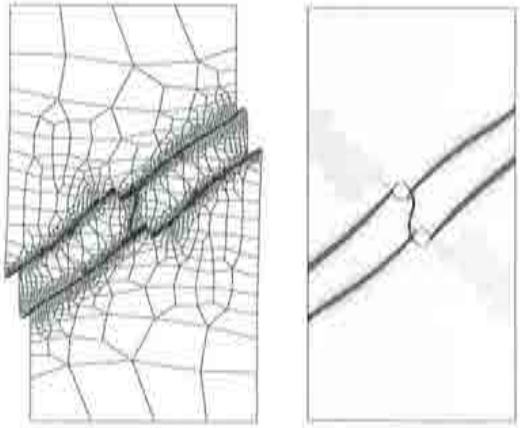

Mesh 3; four shear bands completely developed

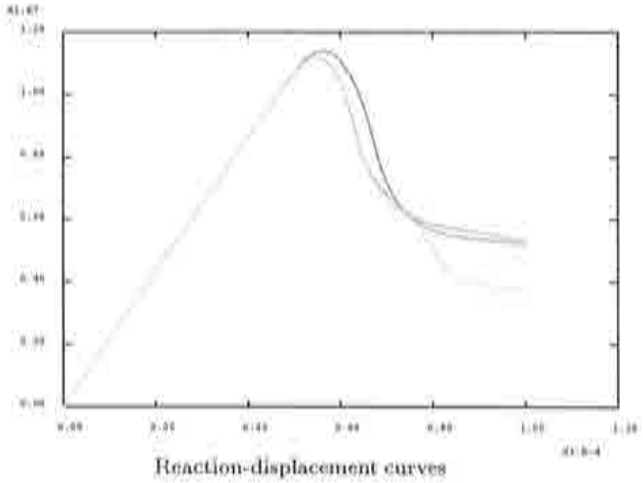

Dark curve: mesh 0

Medium curve: mesh 1

Bright curve: meshes 2 and 3

Reaction-displacement curves

Figure 4.12: Numerical bifurcation in the first meshes: mesh deformation amplified 40 times and equivalent inelastic strain contours

Physical phenomenon

The complexity of this example and its engineering interest justify a further analysis and explanation. Figure 4.13 presents the mesh deformation and the inelastic strain contours at two stages of the loading history for the final mesh. The first stage ($\delta = 0.07$ mm) belongs to the softening branch, and is located where the curvature of the reaction-displacement curve changes sign. At this point, only two shear bands are completely developed, and consequently, the upper part of the specimen slides with respect to the other part along only two surfaces. However, it is clear that this failure mechanism mobilised at this point is kinematically incompatible, and is not sufficient to absorbe the total imposed displacement. Then, as the loading process goes on, the secondary shear bands fully develop, and the final mechanism with four sliding surfaces is mobilised. This complex process is reflected in the reaction-displacement curve with a succesion of concavities and convexities. This example shows clearly the necessity of considering large strains and an updated Lagrangian formulation to capture correctly the phenomenon.

Finally, figure 4.14 presents the profiles of the inelastic strain at several moments of the loading process along two different lines. The profiles along (C-C') intercept two shear bands, the left one being one of the two bands that develop completely in the first place, and the right one being one of the secondary bands. The profiles show that in the first stages the one of the bands develops more, but at the end, the two have reached high ineleastic strains. On the other hand, the profiles along (D-D') show the little relevance of the shear band that develops between the two openings. It can be noticed that this band starts to show up at a certain moment of the loading history, and stops to develop after a while remaining unchanged in the last stages. Despite this local phenomenon is inactive at the end of the loading, when the error is estimated in the remeshing process, the refined meshes do concentrate elements in this zone. Thus, this shows that the adaptive strategy presented performs well in history dependent processes, capturing phenomena that have taken place in the 'past', before the error is estimated.

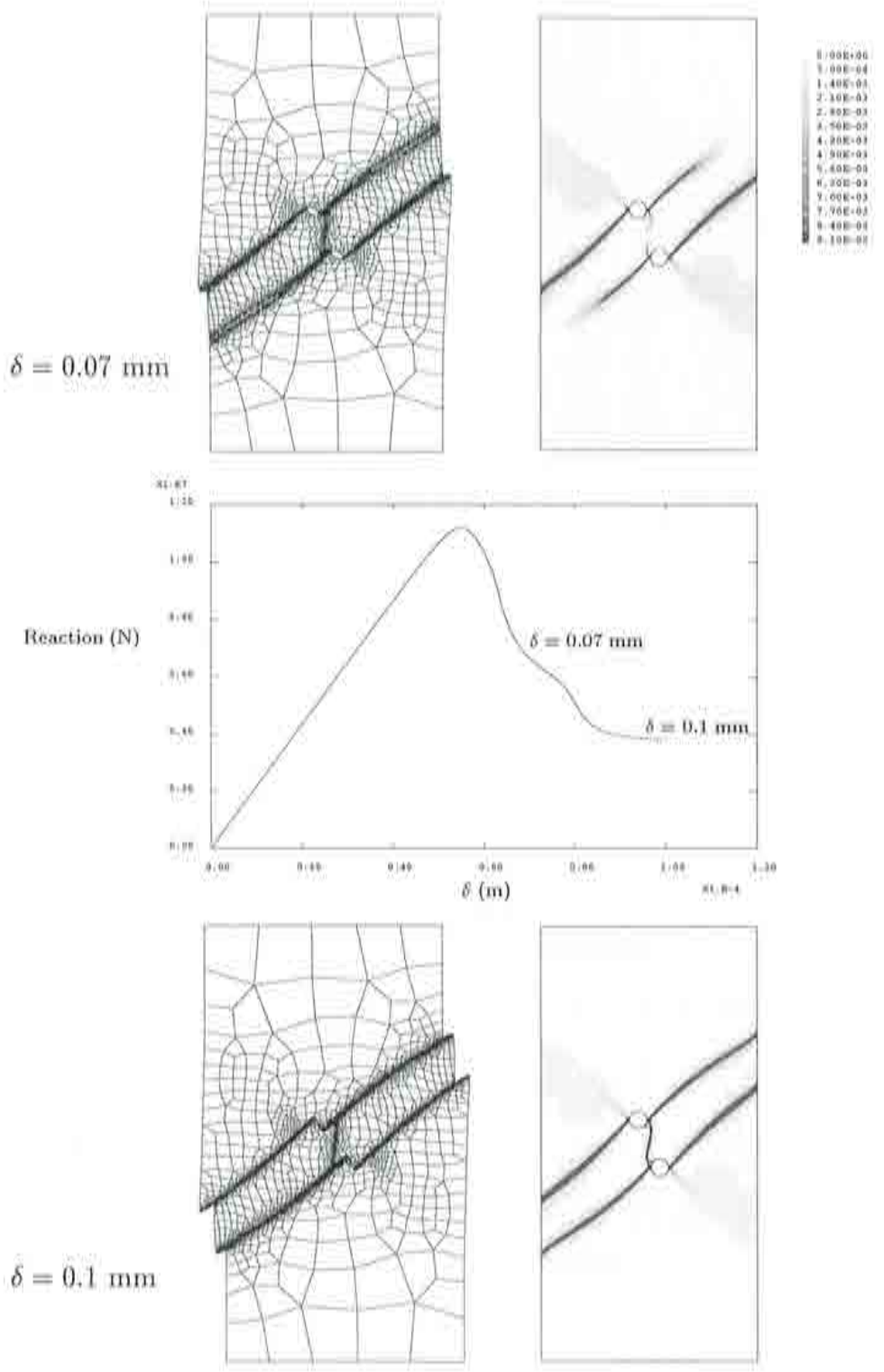

Figure 4.13: Two consecutive failure mechanisms for the final mesh: mesh deformation amplified 40 times and equivalent inelastic strain contours at two moments of the loading history

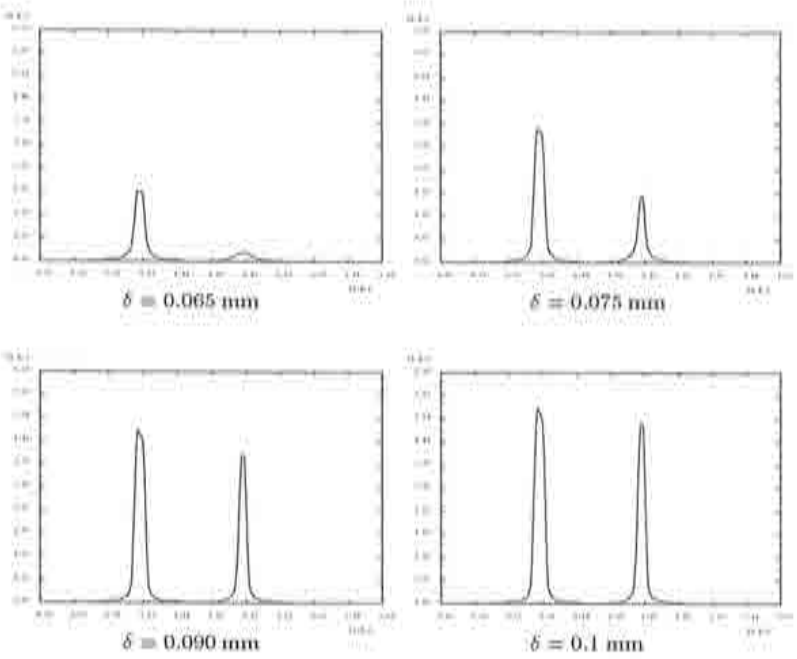

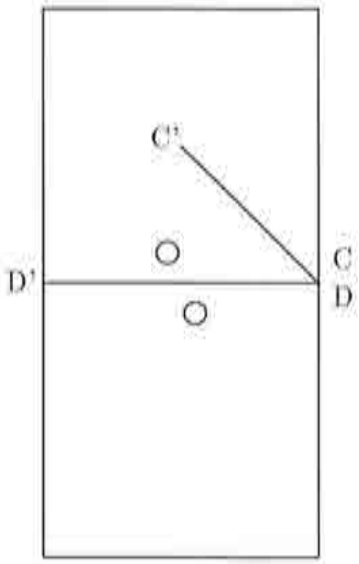

Profiles along (C-C')

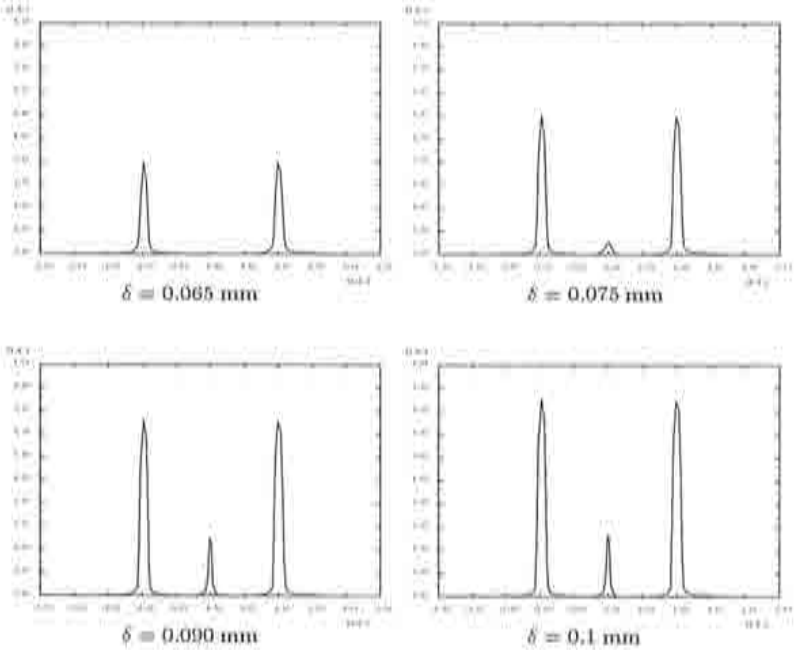

Profiles along (D-D')

Figure 4.14: Evolution of the equivalent inelastic strain profiles in the loading process

Chapter 5

CONCLUSIONS

5.1 Concluding remarks

This work has been mainly concerned with the Finite Element simulation of strain localisation problems in quasi-static problems, appearing as a consequence of the softening behaviour of certain materials. Recall from the introduction that this numerical simulation has to face two major difficulties: the need of a proper constitutive modelisation in order to obtain mathematically well-posed problems on one side, and the need of a cost-effective computational strategy capable of capturing the multi-scale nature of localisation problems accurately on the other side. In the present work, the former has been overcome using two well-known regularisation techniques: rate dependence has been used to regularise J_2 softening plasticity (via Perzyna viscoplasticity) presenting shear band localisation, and the Mazars damage model with nonlocal regularisation has been applied to simulate fracture localisation. On the other hand, adaptivity has been proposed as a natural solution to the computational difficulties caused by the existence of two scales in the problem.

The adaptive remeshing procedure presented in this work leans on a posteriori error estimation, and constitutes a theoretically sound alternative to the usual error indicator driven adaptive procedures proposed by other authors to solve strain localisation problems. The residual type error estimator presented in the current work can be applied to elliptic problems, ellipticity being guaranteed in quasi-static regularised problems.

The examples presented throughout the work show the good performance and suitability of the adaptive procedure in strain localisation problems, solving accurately complex problems whose non-adaptive resolution is out of reach for the available computational resources. Indeed, the intrinsic difficulties of localisation problems, that is the existence of two scales and the fact that the localisation pattern is unknown a priori, are successfully overcome by the presented adaptive methodology.

Apart from presenting a cost-effective and objective methodology to solve the multi-scale nature of localisation problems, other more specific conclusions have been obtained and are summarised below:

- The residual type error estimator presented is efficient and captures the pollution

errors. It can be used in general nonlinear problems, either in its fully nonlinear version or in its tangent version.

- Perzyna softening viscoplasticity leads to mesh objective numerical results in quasi-static shear band localisation problems.
- In the quasi-static case, the shear band width seems to depend on the whole boundary value problem, and in particular on the loading velocity. However, this width can be scaled conveniently without altering the viscous regularising effects, by changing the exponent N of Perzyna model. On the other hand, the imperfection size affects the shear band width when it is smaller than the natural width, and near the imperfection.
- The adaptive procedure can be used in shear band localisation problems, using Perzyna viscoplasticity and the tangent version of the nonlinear error estimator.
- The adaptive procedure based on error estimation answers objectively to the basic issues of adaptivity: where to put the elements, and how many elements are needed to obtain accurate solutions.
- This objective approach represents a powerful tool to investigate on error indicators, which are computationally cheaper than error estimators, but often lack theoretical basis.
- According to the problems studied here, the pollution errors can be negliged in the adaptive process.
- The adaptive remeshing procedure is capable of capturing complex failure mechanisms, which are missed when arbitrary meshes are used.
- The error estimator driven adaptive procedure can also be applied to fracture localisation problems in which Mazars damage model is used with nonlocal regularisation.

5.2 Contributions and future developments

According to what has been said before, the main contribution of the current work is the use of adaptivity based on error estimation in strain localisation problems with softening materials. Other contributions are related with the implementation of Perzyna model and the residual error estimator in an Object Oriented Code. In the implementation of the error estimator, the work has focused on the computational aspects. The Perzyna model qualitative behaviour has also been studied in detail, providing a good understanding of its principal characteristics. On the other hand, the shear band width has been studied for the quasi-static two dimensional case. Furthermore, the incidence of pollution error on the adaptive process has been investigated, concluding that they are negligible. Finally, it has been seen that the error estimation analysis presented can be very useful in research on error indicators.

When it comes to future developments, some have been suggested throughout the work. Indeed, two topics of very intense present research, adaptivity and strain localisation, have been treated here. Therefore, selecting a few particular aspects among many interesting topics of research represents a difficult task. Nevertheless, some stimulating future developments are naturally suggested by this work.

Firstly, as several authors suggest ([39], [19]), a procedure adapting the mesh all along the loading process seems more adequate for history dependent processes than an adaptive procedure remeshing at the end of the loading history as the one used in this work. Thus, a promising research could be carried out developping a mixed ALE-remeshing adaptive procedure based on error estimation, adapting the discretisation several times parallely to the incremental loading.

A subject of further research is also the introduction of modifications in the error estimators, maintaining its philosophy, in order to obtain a better performance. The research would be centred in the generation of the reference space in which the error is projected to find the estimate, using p-refinement for instance. On the other hand, the parallelisation of the estimation algorithm may result of great interest.

Another stimulating topic is the development of performant error indicators from the objective information supplied by adaptivity based on error estimation. The approach presented in the current work can also be used in the design of a methodology to evaluate existing error indicators.

Finally, other related problems, such as adaptivity based on error estimation in transient localisation problems or error estimation linked to different localisation limiters, also appear as promising research topics.

Appendix A

THE PERZYNA MODEL

When the modelling of the softening behaviour exhibited by certain materials is attempted using elastoplastic models, important mathematical and practical problems arise. They can be summarised in a change of type of the governing equations, leading to an ill-posed problem. As a consequence, when this problem is solved numerically with the finite element method, it shows a pathological mesh sensitivity.

This situation can be precluded using the so-called regularisation techniques. One of those techniques is the inclusion of material rate effects in the constitutive model via viscoplasticity. Perzyna model provides a viscoplastic model that can be used in order to obtain well-posed problems. It is especially well suited to model materials that show Mode-II localisation (shear-banding).

This model considers viscous effects during the inelastic flow, or in other words, the existence of additional stresses associated to the inelastic strain rate. A practical consequence is that the material takes time to deform when it is loaded, and also takes time to recover when it is unloaded. This does not happen in rate independent materials, that show instantaneous responses.

This appendix focuses on Perzyna viscoplasticity, including its formulation, phenomenology and the validation of the implementation of the model in the finite element Object Oriented Code CASTEM 2000. In section A.1, the constitutive equations of Perzyna model are presented. Then, in section A.2, the general equations are simplified to formulate simple tensile and shear problems in terms of ordinary differential equations. These ODE's can be easily solved numerically, providing examples that illustrate the qualitative behaviour of the model with respect to rate dependence. These examples are presented in section A.3, where the relationship between viscoplasticity, elastoplasticity and elasticity is also discussed. In section A.4, the viscous overstress is analysed and quantified for the shear case. This result is used in section A.5 to study the influence of the parameter N of the model. Finally, the validation tests of Perzyna model implementation are shown in section A.6. These tests consist on comparing the results obtained integrating the ODE's and those obtained solving a finite element problem which is theoretically equivalent to the original problem. Simple tensile and shear problems are tested, with positive results in both cases.

A.1 Formulation of Perzyna viscoplasticity

Before the constitutive equations are presented, let us comment how rate dependence is introduced into the model. Although this behaviour is the most relevant aspect of Perzyna viscoplasticity as a regularisation technique, the model is described by similar equations to those of rate independent plasticity, and rate dependence is not explicit in the formulation. Nevertheless, the Perzyna flow rule introduces implicitly this behaviour that appears clearly in the examples presented in the following sections.

Once this preliminar remark has been done, the constitutive equations of Perzyna viscoplasticity are presented (see [22], [33], [30]). The notation employed here is quite standard in continuum mechanics ([15]). Nevertheless, it is worth noting that tensors are denoted in bold, and dots denote rate quantities.

Stress and strain rate tensors

The small strain tensor $\boldsymbol{\varepsilon}$, defined as the symmetric part of the gradient of the displacement field u

$$\boldsymbol{\varepsilon} = \frac{1}{2}(\nabla u + (\nabla u)^T), \tag{A.1}$$

can be decomposed into an elastic strain tensor $\boldsymbol{\varepsilon}^e$ and an inelastic, in this case viscoplastic, strain tensor $\boldsymbol{\varepsilon}^{vp}$. Therefore, the following rate-form equation holds

$$\dot{\boldsymbol{\varepsilon}} = \dot{\boldsymbol{\varepsilon}}^e + \dot{\boldsymbol{\varepsilon}}^{vp}. \tag{A.2}$$

With such decomposition the stress rate tensor $\dot{\boldsymbol{\sigma}}$ can be written, following an hypoelastic law, as

$$\dot{\boldsymbol{\sigma}} = \mathbf{D}^e : (\dot{\boldsymbol{\varepsilon}} - \dot{\boldsymbol{\varepsilon}}^{vp}), \tag{A.3}$$

where $\mathbf{D}^e$ is the Hooke tensor.

Note that, although the formulation is given for small strains, the large strain case is easily obtained substituting the strain rate tensor $\dot{\boldsymbol{\varepsilon}}$ by the rate-of-deformation tensor $\mathbf{d}$, defined as

$$\mathbf{d} = \frac{1}{2}(\nabla v + (\nabla v)^T), \tag{A.4}$$

where v is the velocity field. In this case, the strains are obtained integrating $\mathbf{d}$, and in equation A.3, $\dot{\boldsymbol{\sigma}}$ must be substituted by an objective stress rate that accounts for rigid rotations.

The yield function

As in plasticity, a yield function f depending on the stress tensor $\boldsymbol{\sigma}$ and the equivalent inelastic strain κ must be defined. This equivalent inelastic strain is a scalar variable that parametrises the material level of plastification and depends on the strain history. Its rate is defined as

$$\dot{\kappa} = \sqrt{\frac{2}{3}\,\dot{\boldsymbol{\varepsilon}}^{vp} : \dot{\boldsymbol{\varepsilon}}^{vp}}. \tag{A.5}$$

One possible choice for the yield function $f(\boldsymbol{\sigma}, \kappa)$ is the one given by the Von Mises criterion

$$f(\boldsymbol{\sigma}, \kappa) = \sqrt{3\, J_2} - \bar{\sigma}(\kappa). \tag{A.6}$$

In this equation, J_2 stands for the second invariant of the deviatoric stress tensor $\boldsymbol{\sigma}_d$, which is defined as

$$\boldsymbol{\sigma}_d = \boldsymbol{\sigma} - \frac{I_1}{3}\mathbf{I}, \tag{A.7}$$

where I_1 is the first invariant (the trace) of the stress tensor and $\mathbf{I}$ the identity tensor. Thus, the second invariant J_2 can be written as

$$J_2 = \frac{1}{2}\boldsymbol{\sigma}_d : \boldsymbol{\sigma}_d. \tag{A.8}$$

In equation A.6 also appears the yield stress $\bar{\sigma}(\kappa)$ at a certain point of strain history, which must be positive and can be taken as a non-negative linear function of the equivalent viscoplastic strain κ

$$\bar{\sigma}(\kappa) = < \bar{\sigma}_0 + h\,\kappa >, \tag{A.9}$$

h being the hardening/softening modulus and $\bar{\sigma}_0$ the initial yield stress. The function $< \cdot >$ is defined as $< x >= \frac{1}{2}(|x| + x)$. Therefore, $\bar{\sigma}(\kappa) = \bar{\sigma}_0 + h\,\kappa$ if $\bar{\sigma}_0 + h\,\kappa > 0$ and $\bar{\sigma}(\kappa) = 0$ if $\bar{\sigma}_0 + h\,\kappa \leq 0$.

It is at this moment that strain softening behaviour can be introduced into the model, by setting h to a negative value. It is obvious that doing so, the yield stress $\bar{\sigma}$ decreases as viscoplastic strain κ grows, obtaining the desired behaviour.

Viscoplastic flow rule

Similarly to rate independent plastic theory, a viscoplastic potential g_{vp} is defined. Considering associative flow, the yield function and the viscoplastic potential are the same function $f = g_{vp}$. Consequently, the tensor $\mathbf{m}$ representing the direction of the viscoplastic flow, defined as the gradient of the viscoplastic potential g_{vp}, can be written as

$$\mathbf{m} = \frac{\partial f}{\partial \boldsymbol{\sigma}}. \tag{A.10}$$

Until here, there are no significant differences with rate independent plasticity. In fact, the only difference stems from the viscoplastic strain rate proposed by Perzyna (1966)

$$\dot{\boldsymbol{\varepsilon}}^{vp} = \gamma \left[\frac{< f >}{\bar{\sigma}_0}\right]^N \mathbf{m}, \tag{A.11}$$

in which γ is a fluidity parameter depending on the material viscosity, N is a constant and σ_0 is the initial yield stress. As before, the notation $< f >$ means that $< f >= 0$ if $f \leq 0$ and $< f >= f$ if $f > 0$.

At this point, having presented all the model equations, it is relevant to note one essential difference between viscoplasticity and rate independent plasticity. In rate independent plastic theory, stress states must always remain inside the yield surface. This condition is implicit in the very formulation of the model, with the plastic consistency condition that rules the plastic processes. On the contrary, in viscoplasticity, stress states outside the yield surface can exist. This is the reason why viscoplastic flow rules are often called overstress laws. Nevertheless, although in this case there is no condition forcing stress states to stay inside the yield surface, under constant loading conditions they tend to go back to it.

A.2 One dimensional representation of the model

The aim of the current section is to define simple mechanical problems whose governing equations can be simplified to scalar ordinary differential equations. To do this, some general equations are particularised to the case of plane stress, which is assumed. Then, one dimensional problems with uniform stress and strain fields are considered, in both the tensile and the shear cases. In those problems kinematics and equilibrium are trivial. Therefore, the resulting sets of ODE's are particular expressions of the general constitutive equations of the model. These simple problems, that can be easily solved numerically, are used in sections A.3 and A.5 to study the qualitative behaviour of the model, and in section A.6 to test Perzyna implementation in CASTEM. They are also used in section A.4 to obtain an expression of the viscoplastic overstress for the shear case. At the end of the present section, the model is illustrated using a simple rheologic scheme.

A.2.1 Basic equations in plane stress

The assumption of plane stress means that all the components related to the z axis are null

$$\sigma_{xz} = \sigma_{zy} = \sigma_{xz} = \sigma_{yz} = \sigma_{zz} = 0. \tag{A.12}$$

In this case, only 2×2 tensors can be considered

$$\boldsymbol{\varepsilon} = \begin{bmatrix} \varepsilon_{xx} & \varepsilon_{xy} \\ \varepsilon_{yx} & \varepsilon_{yy} \end{bmatrix} \quad \boldsymbol{\varepsilon}^{vp} = \begin{bmatrix} \varepsilon_{xx}^{vp} & \varepsilon_{xy}^{vp} \\ \varepsilon_{yx}^{vp} & \varepsilon_{yy}^{vp} \end{bmatrix} \quad \boldsymbol{\sigma} = \begin{bmatrix} \sigma_{xx} & \sigma_{xy} \\ \sigma_{yx} & \sigma_{yy} \end{bmatrix}. \tag{A.13}$$

In this plane stress situation and according to equations A.6, A.7 and A.8, the yield function can be expressed as

$$f(\boldsymbol{\sigma}, \kappa) = \sqrt{\sigma_{xx}^2 + \sigma_{yy}^2 - \sigma_{xx}\sigma_{yy} + \frac{3}{2}(\sigma_{xy}^2 + \sigma_{yx}^2)} - \bar{\sigma}(\kappa). \tag{A.14}$$

Therefore, derivating this expression as is shown in equation A.10, an expanded expression of the flow direction tensor $\mathbf{m}$ is obtained in the case of plane stress

$$\mathbf{m} = \frac{1}{2\sqrt{\sigma_{xx}^2 + \sigma_{yy}^2 - \sigma_{xx}\sigma_{yy} + \frac{3}{2}(\sigma_{xy}^2 + \sigma_{yx}^2)}} \begin{bmatrix} 2\sigma_{xx} - \sigma_{yy} & 3\sigma_{xy} \\ 3\sigma_{yx} & 2\sigma_{yy} - \sigma_{xx} \end{bmatrix}. \tag{A.15}$$

Note that, in the expression of the yield function of equation A.14, the symmetry of the stress tensor $\boldsymbol{\sigma}$ is not taken into account, and σ_{xy} and σ_{yx} are kept formally different. This is because the flow direction tensor $\mathbf{m}$ is the yield function derivate with respect to the stress tensor. Therefore, this condition must be imposed once the derivation has been done.

Apart from that, the Poisson ratio is set to zero in order to simplify the formulation. The condition $\nu = 0$ implies that

$$\mathbf{D}^e = E\,\mathbf{I}, \tag{A.16}$$

where $\mathbf{D}^e$ is the Hooke tensor, E Young's modulus and $\mathbf{I}$ the two dimension identity tensor. Therefore, equation A.3 can be rewritten as

$$\dot{\boldsymbol{\sigma}} = E\,(\dot{\boldsymbol{\varepsilon}} - \dot{\boldsymbol{\varepsilon}}^{vp}), \tag{A.17}$$

in which $\boldsymbol{\sigma}$, $\boldsymbol{\varepsilon}$ and $\boldsymbol{\varepsilon}^{vp}$ are the 2×2 tensors of equation A.13.

A.2.2 Simple tensile case

Let us consider now the problem shown in figure A.1. It is a slab of viscoplastic material subjected to an imposed displacement δ in the x direction. The loading conditions are considered quasi-static.

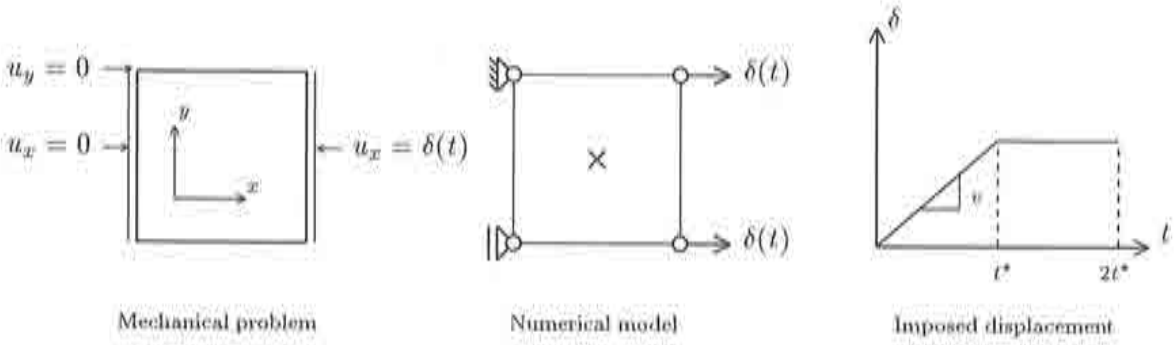

Figure A.1: Simple tensile test

Governing equations

It is obvious from the boundary conditions and quasi-static equilibrium, that in this case σ_{yy} and σ_{xy} are null, and the stress and the strain tensors are uniform fields. Therefore, according to equation A.17, the viscoplastic strain tensor is also uniform. Thus, the stress tensor can be written as

$$\boldsymbol{\sigma} = \begin{bmatrix} \sigma_{xx} & 0 \\ 0 & 0 \end{bmatrix}, \tag{A.18}$$

the yield function (see equation A.14) as

$$f = |\sigma_{xx}| - \bar{\sigma}(\kappa), \tag{A.19}$$

and, according to equation A.15, the flow direction tensor as

$$\mathbf{m} = \frac{1}{2\sqrt{\sigma_{xx}^2}} \begin{bmatrix} 2\sigma_{xx} & 0 \\ 0 & -\sigma_{xx} \end{bmatrix} = \operatorname{sign}(\sigma_{xx}) \begin{bmatrix} 1 & 0 \\ 0 & -\frac{1}{2} \end{bmatrix}. \tag{A.20}$$

Thus, considering equation A.11, the viscoplastic strain rate tensor is of the form

$$\dot{\varepsilon}^{vp} = \gamma \left[\frac{< f >}{\bar{\sigma}_0} \right]^N \begin{bmatrix} 1 & 0 \\ 0 & -\frac{1}{2} \end{bmatrix} \text{sign}(\sigma_{xx}), \tag{A.21}$$

and the equivalent viscoplastic strain rate can be written, according to equation A.5, as

$$\dot{\kappa} = \sqrt{\frac{5}{6}}\, \gamma \left[\frac{< f >}{\bar{\sigma}_0} \right]^N, \quad \text{or} \quad \dot{\kappa} = \sqrt{\frac{5}{6}}\, \dot{\varepsilon}^{vp}_{xx}. \tag{A.22}$$

Assuming that κ and ε^{vp}_{xx} initial values are identical, this rate-form equation can be rewritten as

$$\kappa = \sqrt{\frac{5}{6}}\, \varepsilon^{vp}_{xx}, \tag{A.23}$$

and the following expression is obtained for the yield stress (see equation A.9)

$$\bar{\sigma} = \bar{\sigma}_0 + \sqrt{\frac{5}{6}}\, h\, \varepsilon^{vp}_{xx}. \tag{A.24}$$

At this point, the basic equations of the model have been simplified for this particular case. Nevertheless, the aim of the current section is to obtain a one dimensional problem, and the equations still involve 2×2 tensors. To get to the simple tensile problem, attention must be paid to equation A.17. Since $\dot{\sigma}$ and $\dot{\varepsilon}^{vp}$ are diagonal tensors (see equations A.18 and A.21), this equation implies that $\dot{\varepsilon}$ is also a diagonal tensor. Therefore, the xx and the yy components are independent (the xy and yx components are zero), and the two dimensional problem can be decomposed into two uncoupled one dimensional problems. Thus, considering only the xx components of the tensors, the simple tensile one dimensional case is obtained.

To sum up, the governing equations of this one dimensional problem can be rewritten using A.19, A.21, A.17 and A.24, as follows

$$\begin{cases} f &= \sigma_{xx} - \bar{\sigma} \\ \dot{\varepsilon}^{vp}_{xx} &= \begin{cases} 0 & \text{if } f \leq 0 \\ \gamma [\frac{f}{\bar{\sigma}_0}]^N \text{sign}(\sigma_{xx}) & \text{if } f > 0 \end{cases} \\ \dot{\sigma}_{xx} &= E\,(\dot{\varepsilon}_{xx} - \dot{\varepsilon}^{vp}_{xx}) \\ \bar{\sigma} &= \bar{\sigma}_0 + \sqrt{\frac{5}{6}}\, h\, \varepsilon^{vp}_{xx} \end{cases} \tag{A.25}$$

In fact, this is a set of ODE's where the unknowns are ε^{vp}_{xx} and σ_{xx}. It can be solved by any standard ODE method, given the model parameters ($N, \gamma, \bar{\sigma}_0, E$ and h), and the total strain rate $\dot{\varepsilon}_{xx}$ as a function of time. This function is obtained for this tensile problem in the following paragraphs.

Prescribed total strain rate

The expression of the total strain rate imposed in the problem shown in figure A.1 is now derived from the imposed displacement δ. This displacement is characterised by a constant rate $\dot{\delta} = v$ in the first half of the test. In the second half, $\delta(t)$ remains constant, so that the viscoplastic overstress caused by the strain rate can vanish with time. So, $\delta(t)$ is defined as

$$\delta(t) = \begin{cases} v\,t & \text{if } t \in [0; t^*] \\ \delta^* & \text{if } t \in [t^*; 2t^*] \end{cases} \qquad \text{with } \delta^* = v\,t^* . \tag{A.26}$$

It is easy to see that this imposed displacement boundary condition causes a displacement field in the x direction of the form

$$u_x = \frac{\delta(t)}{l} x. \tag{A.27}$$

Then, considering small strains, the xx component of the total strain tensor is

$$\varepsilon_{xx} = \frac{\partial u_x}{\partial x} = \begin{cases} \frac{v}{l}\,t & \text{if } t \in [0; t^*] \\ \frac{\delta^*}{l} & \text{if } t \in [t^*; 2t^*] \end{cases} , \tag{A.28}$$

which is a uniform strain field. So, according to this equation, the total strain rate expression is finally obtained

$$\dot{\varepsilon}_{xx} = \begin{cases} \frac{v}{l} & \text{if } t \in [0; t^*] \\ 0 & \text{if } t \in [t^*; 2t^*] \end{cases} . \tag{A.29}$$

A.2.3 Simple shear test

The problem shown in figure A.2, similarly to the previous one, can be formulated as a one dimensional uniform problem. In this case, the slab of viscoplastic material is subjected to a quasi-static imposed displacement in the y direction, causing a simple shear strain state.

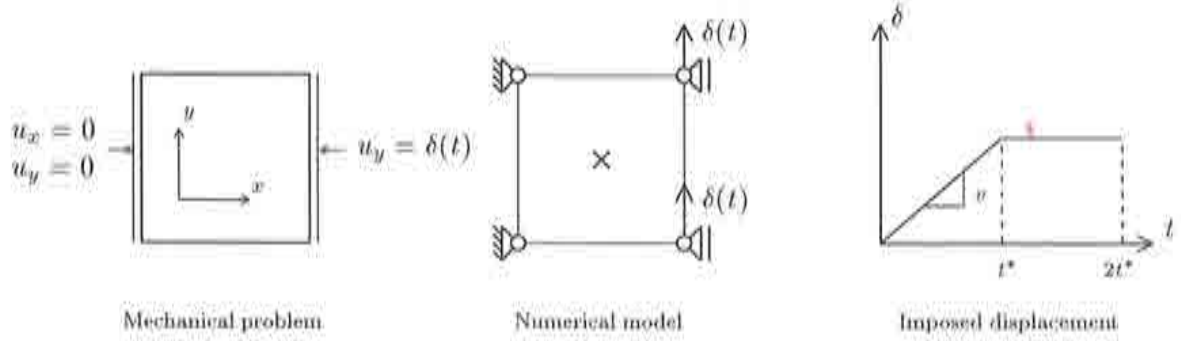

Figure A.2: Simple shear test

Governing equations

Similarly to the tensile case, this problem involves also uniform fields. In addition, only xy and yx stresses are non-null. Thus, as the stress tensor is symmeric, it can be written as

$$\boldsymbol{\sigma} = \begin{bmatrix} 0 & \sigma_{xy} \\ \sigma_{xy} & 0 \end{bmatrix}, \tag{A.30}$$

and the yield function, according to equation A.14, as

$$f = \sqrt{3}\,|\sigma_{xy}| - \bar{\sigma}(\kappa). \tag{A.31}$$

Using equation A.15, the flow direction can be written in this case as

$$\mathbf{m} = \frac{1}{2\sqrt{3}\,|\sigma_{xy}|}\begin{bmatrix} 0 & 3\sigma_{xy} \\ 3\sigma_{xy} & 0 \end{bmatrix} = \operatorname{sign}(\sigma_{xy})\begin{bmatrix} 0 & \frac{\sqrt{3}}{2} \\ \frac{\sqrt{3}}{2} & 0 \end{bmatrix}. \tag{A.32}$$

Therefore, using equation A.11, the viscoplastic strain rate can be written as

$$\dot{\boldsymbol{\varepsilon}}^{vp} = \gamma\left[\frac{< f >}{\bar{\sigma}_0}\right]^N \begin{bmatrix} 0 & \frac{\sqrt{3}}{2} \\ \frac{\sqrt{3}}{2} & 0 \end{bmatrix} \operatorname{sign}(\sigma_{xy}), \tag{A.33}$$

and the equivalent viscoplastic strain, similarly to the tensile case, as

$$\kappa = \frac{2}{\sqrt{3}}\varepsilon^{vp}_{xy}. \tag{A.34}$$

It is obvious that this problem is also one dimensional. As has been done for the simple tensile case, the governing equations of this simple shear problem can be summarised as follows

$$\begin{cases} f &= \sqrt{3}\,\sigma_{xy} - \bar{\sigma} \\ \dot{\varepsilon}^{vp}_{xy} &= \begin{cases} 0 & \text{if } f \le 0 \\ \frac{\sqrt{3}}{2}\,\gamma\left[\frac{f}{\bar{\sigma}_0}\right]^N \operatorname{sign}(\sigma_{xy}) & \text{if } f > 0 \end{cases} \\ \dot{\sigma}_{xy} &= E\,(\dot{\varepsilon}_{xy} - \dot{\varepsilon}^{vp}_{xy}) \\ \bar{\sigma} &= \bar{\sigma}_0 + \frac{2}{\sqrt{3}}\,h\,\varepsilon^{vp}_{xy} \end{cases} \tag{A.35}$$

Although this new set of ODE's is very similar to the previous one, it is useful to test CASTEM's implementation of Perzyna model for a shear problem.

Prescribed total strain rate

As in the tensile case, the total strain rate imposed is needed to solve the equations governing the simple shear problem. In this case, the expression of δ is identical to the previous case. It is easy to see that this imposed displacement boundary condition causes a displacement field such that only the y component is different to zero

$$u_y = \frac{\delta(t)}{l} x, \tag{A.36}$$

and considering as before small strains, the total strain can be written as

$$\varepsilon_{xy} = \frac{1}{2}\left(\frac{\partial u_x}{\partial y} + \frac{\partial u_y}{\partial x}\right) = \frac{\delta}{2l} = \begin{cases} \frac{v}{2l}\, t & \text{if } t \in [0; t^*] \\ \frac{\delta^*}{2l} & \text{if } t \in [t^*; 2t^*] \end{cases}. \tag{A.37}$$

Therefore, the following expression of the total strain rate is obtained

$$\dot{\varepsilon}_{xy} = \begin{cases} \frac{v}{2l} & \text{if } t \in [0; t^*] \\ 0 & \text{if } t \in [t^*; 2t^*] \end{cases}. \tag{A.38}$$

A.2.4 Rheologic representation of Perzyna model

First of all, the parameter γ of Perzyna model is going to be understood in terms of usual viscosity parameters. To do that, the simple tensile case with $N = 1$ is considered. Under these conditions, the viscoplastic flow rule can be written, according to equations A.25, as

$$\dot{\varepsilon}^{vp} = \gamma \frac{(\sigma - \bar{\sigma})}{\bar{\sigma}_0} = \frac{\gamma}{\bar{\sigma}_0}(\sigma - \bar{\sigma}). \tag{A.39}$$

Defining the parameter η as

$$\eta = \frac{\bar{\sigma}_0}{\gamma}, \tag{A.40}$$

equation A.39 can be written as follows

$$\sigma - \bar{\sigma} = \eta\, \dot{\varepsilon}^{vp}. \tag{A.41}$$

Paying attention to this expression, it is easy to identify η as a classical viscosity parameter, in other words, the ratio between a stress and a strain rate. Thus, recalling equation A.40, it is clear that γ can be seen as a fluidity parameter, thinking of fluidity and viscosity as opposite concepts.

In figure A.3 is shown a graphic representation of Perzyna model in the simple tensile case with $N = 1$. It illustrates the behaviour of the model with simple rheologic elements such as springs and dashpots. This figure is helpful to understand the examples presented in the following sections.

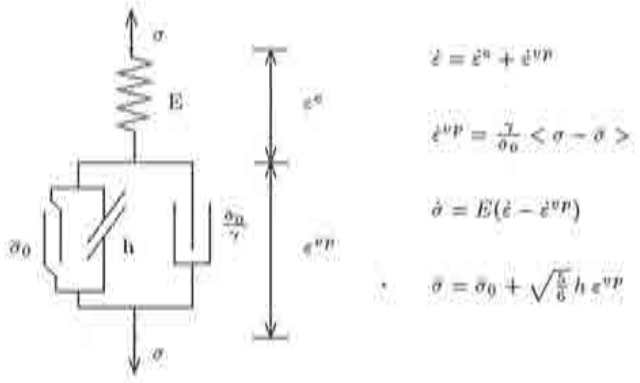

Figure A.3: One dimensional rheologic scheme of Perzyna type viscoplastic model ($N = 1$).

A.3 General and limit behaviour of the model

In order to analyse the Perzyna model qualitative behaviour, the simple shear problem described in figure A.2 is solved with several parameter sets. The results of simple tensile examples are very similar and do not bring additional information.

In first place, a reference example is presented to illustrate the general behaviour of the model. Then, enhancing rate effects, the elastic model is reached as a limit of Perzyna viscoplasticity. Finally, the rate independent limit of Perzyna model is discussed.

In these examples, a fourth order Runge-Kutta method is employed to integrate the set of ODE's. The integration step is selected depending on the parameter set, particularly on γ and v values. At the end of the current section, it can be seen as, for certain values of these parameters, numerical convergence problems are encountered, and smaller integration steps are required.

Reference example

It is easy to see from the governing equations of the shear case (see equations A.35) and from the expression of the total strain rate imposed (see equation A.38), that a set of eight parameters defines completely a problem. These parameters are the model parameters ($N, \gamma, \bar{\sigma}_0, E$ and h), and the three additional parameters (v, l and δ^*). The reference example, that can be used to compare the results with other examples, is defined by the parameters $N = 1$, $E = 200000$, $\sigma_0 = 200$, $h = -10000$, $\delta^* = 0.1$, $l = 10$, $\gamma = 400$ and $v = 1000$.

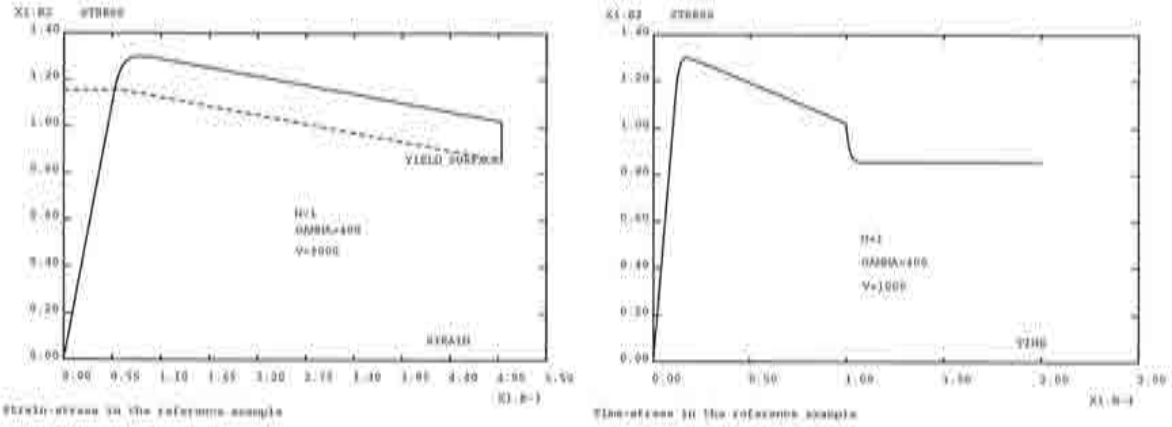

Figure A.4: Strain-stress and time-stress relations for the reference example

In figure A.4, the results obtained by numerical integration are presented. In the first plot, the strain-stress ($\sigma_{xy} - \varepsilon_{xy}$) evolution during the test is plotted in solid line. The yield surface is plotted in dashed line. It is the graphic representation of the function $Y_s = \frac{\sigma}{\sqrt{3}}$

($\bar{\sigma}$ is parametrised by ε_{xy}). It represents the points of the space $\sigma_{xy} - \varepsilon_{xy}$ that verify the condition $f = 0$.

It can be noticed that in the elastic zone (before the first intersection between the two curves), the yield stress remains constant. When the two curves meet, the viscoplastic domain is reached. From this moment on, the stress state remains outside the yield surface, as it has been said, because of the viscoplastic overstress. This overstress, caused by the strain rate, reaches a maximum, and the total stress decreases as long as the yield stress does so. Thus the softening behaviour that forces the yield stress to decrease during the viscoplastic flow can be noticed. Finally, when the maximum total strain is reached and remains constant, the viscoplastic overstress vanishes and the stress state goes back to the yield surface.

In the second plot the time-stress evolution during the test is plotted. The loading zone and the relaxation zone can be clearly recognized. In the loading zone, an elastic and a softening viscoplastic zone can be distinguished. It is easy to see that the viscoplastic overstress decreases with time in a negative exponential way.

Increasing rate effects

As has been said before, the test proposed is defined by eight parameters, five concerning the model and three the loading conditions. But, as long as the aim of the present section is to study the rate effects, the attention can be focused mainly on two parameters, γ (the fluidity parameter), and v (the loading velocity).

Figure A.3 illustrates how rate effects increase when either the velocity increases or the fluidity decreases, which according to equation A.40, is equivalent to a viscosity rise. Therefore, two possibilities appear to study the increasing rate effects.

In figure A.5 a succession of examples is presented, in which rate effects are enhanced by decreasing the value of γ. Similar results are obtained increasing v.

In example 1 ($\gamma = 80$), the problem presents larger viscoplastic overstresses than the reference example. In addition, more time is taken by the overstresses to stabilise and to vanish when we stop loading. Apart from that, the qualitative behaviour is similar to the reference example.

It is also simple to jump from example 1 to example 2 ($\gamma = 10$). The overstresses are now even bigger, and moreover, they are not completely relaxed relaxed at the end of the analysis. It can be seen in this figure that, at the end of the test, the stress states are still outside the yield surface.

Finally, in example 3, an elastic behaviour is reached, as a limit of Perzyna viscoplasticity. An infinite viscosity ($\gamma = 0$) is taken, which means that the dashpot of figure A.3 is blocked. Therefore, viscoplastic strains are zero and only the elastic part of the model is active. This is confirmed by the results shown in figure A.5, where the elastic behaviour is clearly recognized.

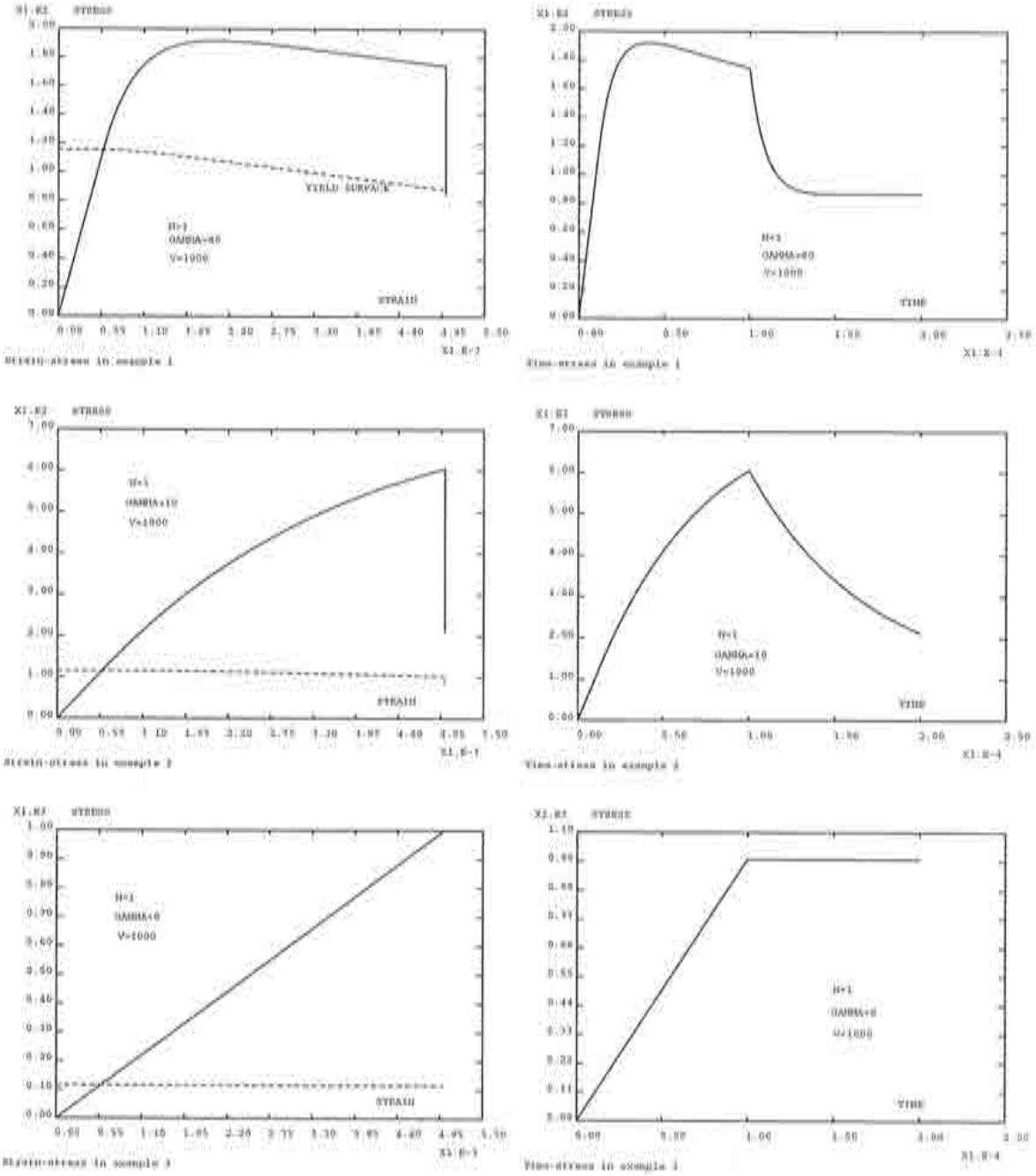

Figure A.5: Towards an elastic model

Decreasing rate effects

Again, two options arise to decrease rate effects. In this case, the reference example is modified by decreasing the value of the loading velocity, $v = 50$.

It is easy to observe that as the loading velocity decreases, the prescribed strain rate decreases (thus the viscoplastic strain rate, $\dot{\varepsilon}^{vp}$, decreases) and, consequently (see equation A.41) the overstresses decreases as well. Therefore, the dashpot in figure A.3 resists almost zero stresses, and the rheologic model resulting is a rate independent plastic model with softening. This behaviour can be seen in example 4 of figure A.6. It can be noticed that, during the viscoplastic flow, the stress states remain almost on the yield surface, with very small overstresses.

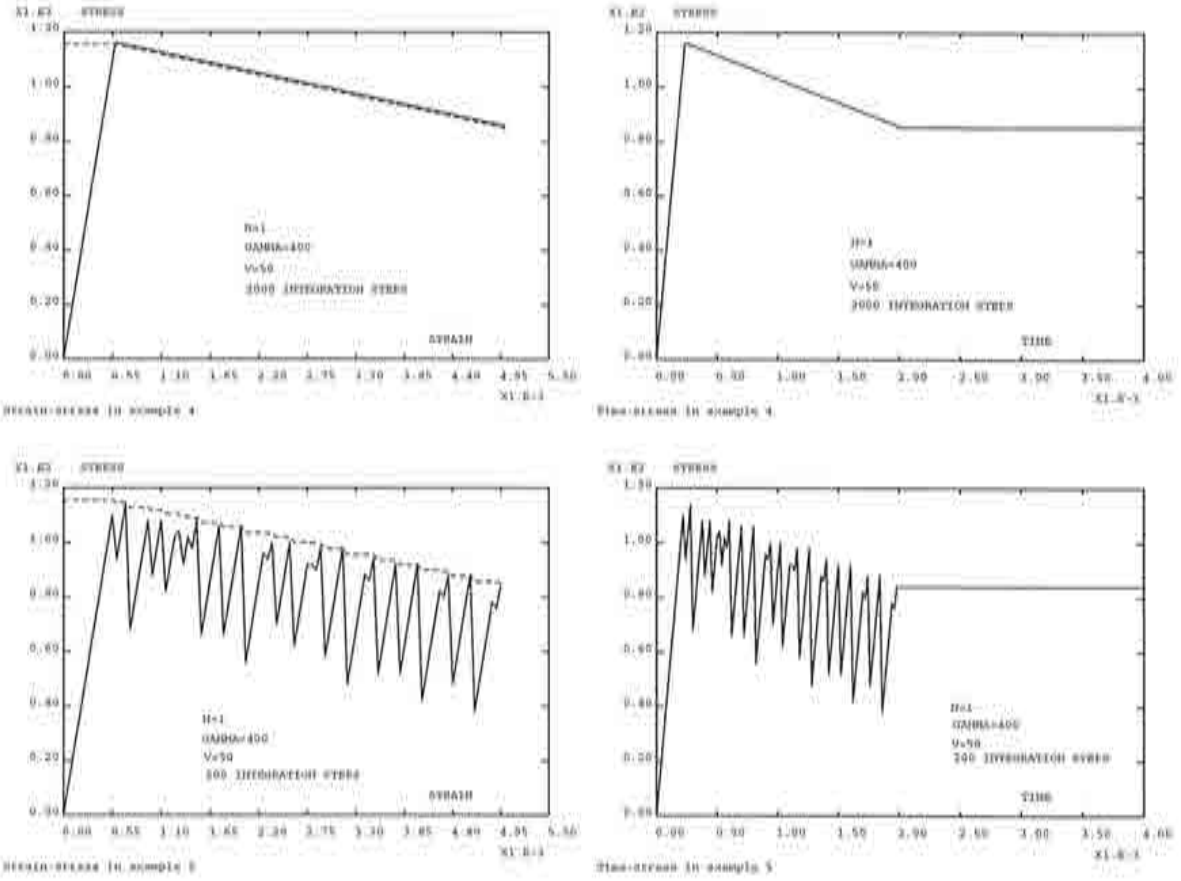

Figure A.6: The elastoplastic limit of viscoplasticity

Another important aspect of this rate independent limit of Perzyna viscoplasticity, is that the set of ODE's is more and more difficult to solve numerically as the limit is reached. Convergence problems appear, and smaller integration steps are required to obtain accept-

able solutions. For instance, in example 4, 2000 time steps have been necessary to obtain a smooth solution. Example 5 illustrates these numerical problems when the set of ODE's is integrated, with $v = 50$ and 200 integration steps, which are more than enough steps to integrate properly the reference example. Very important oscillations are observed in the solution during the viscoplastic softening flow, which disappear as smaller time steps are taken.

A.4 The viscoplastic overstress in the shear case

A.4.1 Relevance of the viscoplastic overstress

As it can be seen in section A.3, the viscoplastic overstress is one of the most relevant aspects of Perzyna viscoplasticity. This overstress can be defined as the difference of the actual stress level and the actual yield stress. In fact, they are represented by the yield function f. The examples of this section show how, under constant strain rate, the overstress stabilises and remains constant. Then, if strain rate becomes null, it vanishes with time.

This overstress may appear as an abstract concept that, being defined from the yield stress, has no practical relevance by itself. Nevertheless, it sometimes plays an important role, for instance, in softening localisation phenomena. When a shear band develops under a constant shear rate, very high viscoplastic strains are reached and consequently, according to equation A.9, the yield stress becomes null. This means that the resistance offered by the material in the localisation zone is only due to the viscous effects. In other words, a viscous flow takes place in the shear band. Therefore, in this situation the viscoplastic overstress rules the residual resistance of the body reaching failure.

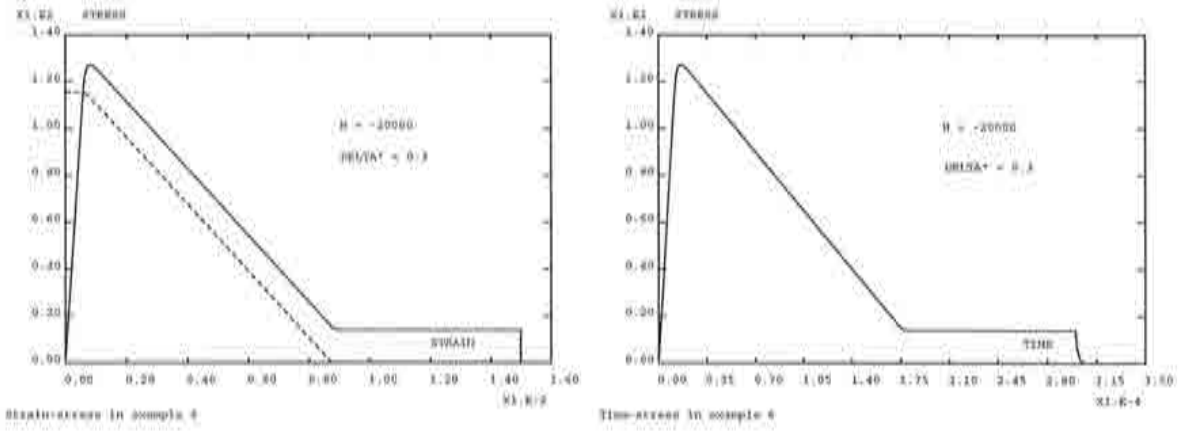

Figure A.7: Reaching failure

Figure A.7 illustrates the behaviour of the model in the shear case. The set of parameters of the reference example have been modified with $h = -20000$ and $\delta^* = 0.3$. The overstress can be seen graphically in the first plot as the vertical distance between the actual stress representation (solid line) and the yield stress representation (dashed line). It can be seen that, when the yield stress becomes null, the only stress that the material resists is the viscoplastic overstress, that vanishes when the load conditions become stationary.

A.4.2 Estimation of the overstress in the shear case

The governing equations of the simple shear case can be easily extended to the case in which the Poisson ratio ν is not zero. The shear problem remains uncoupled in this case. The resulting set of ODE's is identical to the set of equations A.35, except for the elastic coefficient that relates stress rates and elastic strain rates,

$$\dot{\sigma}_{xy} = \frac{E}{1+\nu}\left(\dot{\varepsilon}_{xy} - \dot{\varepsilon}^{vp}_{xy}\right) \tag{A.42}$$

It is also easy to see that these equations deduced for the plane stress case, also hold in the plane strain case. This is because the shear problem is uncoupled with the tensile response in the z direction.

The aim of this subsection is to obtain the expression of the overstress f in the softening branch and in the failure branch when the yield stress is null. The loading conditions assumed are an imposed displacement $\delta(t) = v\,t$ (see figure A.7), so that the strain rate is constant,

$$\dot{\varepsilon}_{xy} = \frac{v}{2l} \tag{A.43}$$

For the sake of simplicity, in the following paragraphs, the $_{xy}$ notation will be ommited, and the elastic coefficient will be denoted as K

$$K = \frac{E}{1+\nu} \tag{A.44}$$

Overstress in the softening branch

It has been said that, under constant strain rate imposed, the overstress stabilises in the softening branch (see figure A.4), so that the slope of the function $\sigma - \varepsilon$ remains constant. The mathematical expression of this condition can be written as follows,

$$\frac{d}{dt}\left(\frac{\dot{\sigma}}{\dot{\varepsilon}}\right) = 0 \quad \text{or} \quad \frac{\ddot{\sigma}\dot{\varepsilon} - \dot{\sigma}\ddot{\varepsilon}}{\dot{\varepsilon}^2} = 0. \tag{A.45}$$

But, according to equation A.43, $\dot{\varepsilon} \neq 0$ and $\ddot{\varepsilon} = 0$. Therefore, the following expression is obtained

$$\ddot{\sigma} = 0 \quad \text{or} \quad K\left(\ddot{\varepsilon} - \ddot{\varepsilon}^{vp}\right) = 0. \tag{A.46}$$

Again, as long as $\ddot{\varepsilon} = 0$, this equation is equivalent to

$$\ddot{\varepsilon}^{vp} = 0, \quad \text{or} \quad \left(\dot{f}^N\right)^{\cdot} = N\,\dot{f}\,f^{N-1} = 0. \tag{A.47}$$

Obviously, the overstress f is not null, and consequently the previous equation is equivalent to

$$\dot{f} = \sqrt{3}\,\dot{\sigma} - \dot{\bar{\sigma}} = 0. \tag{A.48}$$

According to equation A.35, $\dot{\bar{\sigma}}$ can be written in terms of the viscoplastic strain rate, and the following expression holds

$$3\dot{\bar{\sigma}} = 2h\dot{\varepsilon}^{vp}, \qquad \text{or} \qquad 3K(\dot{\varepsilon} - \dot{\varepsilon}^{vp}) = 2h\dot{\varepsilon}^{vp}. \tag{A.49}$$

Finally, substituting in this equation the expression of the viscoplastic strain rate $\dot{\varepsilon}^{vp}$ of equation A.35, and the expression of the total strain rate (see equation A.43, the following expression of the overstress is obtained

$$f = \bar{\sigma}_0 \left[\left(\frac{3K}{3K + 2h} \right) \frac{v}{\sqrt{3}\,\gamma\, l} \right]^{\frac{1}{N}} . \tag{A.50}$$

In addition, it is easy to obtain the slope of the function in the softening branch $\sigma - \varepsilon$

$$\frac{\dot{\sigma}}{\dot{\varepsilon}} = \frac{2h}{3 + \frac{2h}{K}} . \tag{A.51}$$

Overstress in the failure branch

When the yield stress becomes null and the material has failed, the slope of the function $\sigma - \varepsilon$ is also null, which can be expressed as

$$\frac{\dot{\sigma}}{\dot{\varepsilon}} = 0 . \tag{A.52}$$

This means that the total strain rate is equal to the viscoplastic strain rate. Therefore, similarly to the previous case, the following expression of the overstress f is obtained

$$f = \bar{\sigma}_0 \left[\frac{v}{\sqrt{6}\,\gamma\, l} \right]^{\frac{1}{N}} . \tag{A.53}$$

A.5 Influence of the parameter N

The parameter N of Perzyna viscoplasticity is important to adjust the model to the real behaviour of certain materials. For instance, it is useful to obtain narrow shear bands without decreasing the rate effects and the viscous overstress. If this parameter is to be modified, one question arises. How should other parameters be changed to obtain a different but comparable behaviour? One possible criterion is to consider that two sets of parameters are comparable if they show similar viscous overstress under certain loading conditions.

To investigate the influence of the parameter N, the reference example (with $N = 1$) is considered, and compared to another example taking $N = 6$. In this second example, all the parameters have been set to the reference values, except N, of course, and γ. The value of γ has been chosen so that the overstress in the softening branch is the same one to that of the reference example, using expression A.53. It results a value of $\gamma = 5.46 \cdot 10^6$.

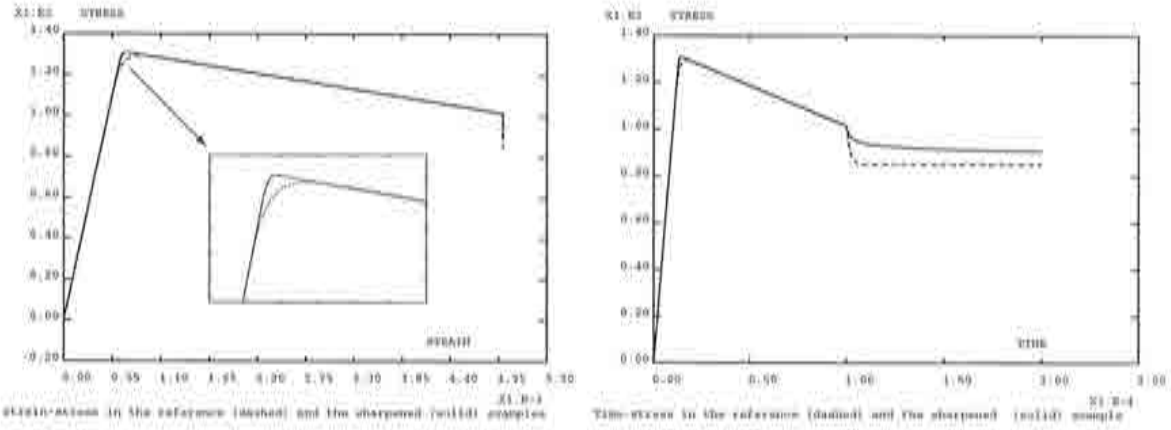

Figure A.8: Effect of N

The results of the reference example (dashed line) and the modified one (solid line) are plotted in figure A.8. The figure shows how both parameter sets present the same overstress, and are then comparable. Apart from that, the influence of taking $N = 6$ instead of $N = 1$ can be summarised in two aspects. Firstly, when the material begins to yield, the transition between the increasing branch and the softening branch is much sharper in the new example. On the other hand, the viscous overstress relax more slowly when the load remains stationnary. Although the right hand side of figure A.8 seems to indicate that the residual stress is different, in fact, they both tend to the same limit.

A.6 Validation tests of CASTEM implementation

To test the implementation of Perzyna model in CASTEM, a comparison is carried out between the results obtained integrating the sets of ODE's derived in the previous sections, and solving an equivalent finite element problem. These tests are performed for both the simple tensile and the simple shear cases.

Figures A.1 and A.2 represent the physical and the numerical models for the tensile and the shear tests. The numerical models are finite element discretisations of the problem, with only one linear finite element of four nodes.

It is obvious that the shape functions associated to this discretisation decribe exactly the linear displacement field to which the slab is subjected in both cases (see equations A.27 and A.36). In addition, the uniform stress state that takes place in these problems is also described exactly. On the other hand, the boundary conditions of the numerical models assure the one dimensional behaviour in stresses. Thus it can be seen that, with an exact time integration, the finite element discretisation of the mechanical problem is capable of reproducing the exact solution.

So, if we assume that the time integration errors are small, approximately the same solution should be obtained solving the set of ODE's or the finite element problem.

Simple tensile test

The parameters that define the present problem are $N = 1$, $E = 200000$, $\sigma_0 = 200$, $h = -10000$, $\delta^* = 0.1$, $l = 10$, $\gamma = 200$ and $v = 1000$.

Figure A.9 shows that practically identical results are obtained either integrating numerically the ODE's governing the mechanical problem or solving the equivalent finite element problem.

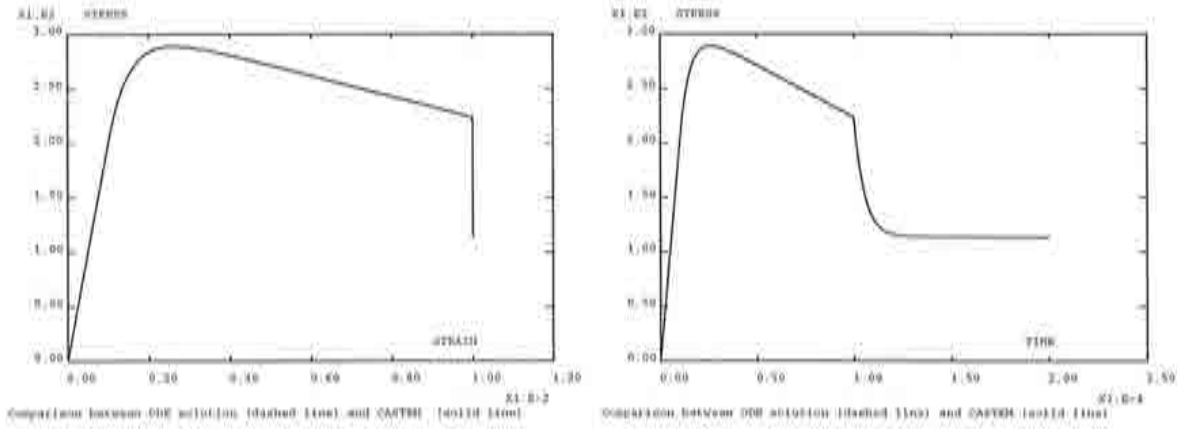

Figure A.9: Tensile validation test of Perzyna implementation

Thus, it can be seen that CASTEM's implementation of the model solves correctly this

tensile case.

Simple shear test

In this case, the problem presented is defined by the parameters $N = 3$, $E = 200000$, $\sigma_0 = 200$, $h = -2000$, $\delta^* = 0.1$, $l = 10$, $\gamma = 500$ and $v = 1000$. Figure A.10 shows the results obtained for this example. As before, the two solutions are practically identical, making it difficult to distinguish between the two curves.

Thus, the model implementation reproduces correctly the shear problem.

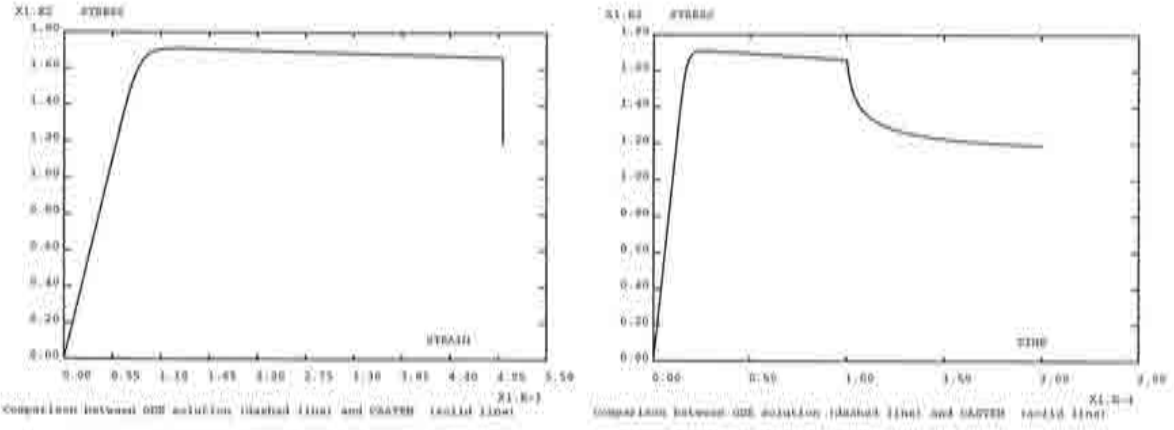

Figure A.10: Shear validation test of Perzyna implementation

Appendix B

ADAPTIVITY WITH MAZARS NONLOCAL DAMAGE

The aim of the present appendix is to illustrate that the error estimator driven adaptive procedure presented in this work can also be applied to fracture localisation problems with nonlocal regularisation. To do this, Mazars damage model is considered, and a remeshing process is applied to a simple example.

B.1 Generalities about damage models and nonlocal regularisation

When the modelling of cracking materials is attempted in continuum mechanics, a very natural way of considering the lack of material in the cracked zones is to introduce the concept of continuum damage, as a degradation of the Young modulus. Damage models take the mechanical effect of cracking into account by means of internal variables that affect the elastic stiffness of the material. There are different damage models, depending on the mathematical nature of the damage variable (scalar of tensorial) and on the damage evolution law. These models have been applied basically to quasi-brittle materials, such as concrete, in which mode-I localisation (fracture) is predominant (see [21], [23] and [27]).

A predictible feature of these models is that they present strain-softening. In effect, as the void density grows, the material becomes more damaged and its resistance decreases. Unfortunately, this softening behaviour leads to serious difficulties due to the ill-posedness of the boundary value problem in statics, or the initial value problem in dynamics. In the zone where strain localises, the governing equations of the static case lose ellipticity. The numerical consequence is a pathological mesh dependency: localisation zones tend to be indefinitely narrow as the mesh is refined, and energy dissipation during failure tends to zero. What is more, the scale of the damage distribution becomes smaller than the size of the material heterogeneites, which has no physical meaning.

To remedy this situation, several methods have been proposed as localisation limiters,

incorporating some physical length in the constitutive equations. One of these techniques is nonlocal regularisation. The nonlocal damage models lead to well-posed problems by averaging the variable that controls the softening behaviour over a neighbourhood of each point. The size of this neighbourhood is related to the size of the material heterogeneites, and characterises the minimum size of localisation zones. Because of the existence of two scales, the scale of material heterogeneites and the scale in which the material is homogeneous, this nonlocal averaging is also known as a multiscale approach. Using this technique, the results obtained using the finite element method are mesh objective, provided that the size of the elements is smaller that the material length in the localisation zone.

Mazars local damage model, presented in section B.2, considers isotropic continuum damage using a scalar damage variable D. This damage variable is a function of the state of tension, which is described by an equivalent strain $\bar{\varepsilon}$. As the model has been developped for concrete, which shows an asymmetric tensile response, it has different damage laws for tension and for compression. Its nonlocal formulation is described in section B.3. It considers a nonlocal equivalent strain by averaging the local quantity over a domain characterised by a length l_c.

B.2 Mazars damage model

B.2.1 Local formulation

As it has been said, the damage variable D represents a degradation of the elastic stiffness of the material, and ranges from zero (non-damaged material) to one (completely damaged material). Therefore, the strain-stress relation of the damaged material is of the form

$$\boldsymbol{\sigma} = (1 - D)\mathbf{D}_e : \boldsymbol{\varepsilon} \,, \qquad \text{with} \qquad 0 \leq D \leq 1 \,, \tag{B.1}$$

being $\mathbf{D}_e$ the Hooke tensor, $\boldsymbol{\sigma}$ the Cauchy stress tensor and $\boldsymbol{\varepsilon}$ the small strain tensor. It can be easily seen that, according to equation B.1, the stress tensor $\boldsymbol{\sigma}$ and the strain tensor $\boldsymbol{\varepsilon}$ have the same principal directions. Therefore, the two tensors are expressed in terms of their principal values, σ_i and ε_i, in the same base.

The evolution of the damage variable is described by an equivalent strain $\bar{\varepsilon}$, which is a norm of the positive strain tensor. This means that it measures only the extensions, that is the positive strains

$$\bar{\varepsilon} = \sqrt{\sum_i (\varepsilon_i^+)^2} \qquad \text{with} \qquad \varepsilon_i^+ = < \varepsilon_i > \,. \tag{B.2}$$

The function $< \cdot >$ is defined as $< x >= \frac{1}{2}(|x| + x)$. Therefore, ε_i^+ equals to ε_i if it is a tension (positive) strain and to zero if it is a compression (negative) strain.

This equivalent strain $\bar{\varepsilon}$ is modified by the parameter γ, which modules the response in the case of multiaxial compression. In fact, the damage variable depends on the product

$\gamma\tilde{\varepsilon}$. This parameter is defined as

$$\gamma = \frac{\sqrt{\sum_i (\sigma_i^-)^2}}{\sum_i \sigma_i^-} \quad \text{with} \quad \sigma_i^- =< -\sigma_i > , \tag{B.3}$$

In this case, σ_i^- equals to the absolute value of σ_i if it is a compression stress, and to zero if it is a tension stress.

The damage variable D is a combination of a tension damage D_t and a compression damage D_c, and its evolution is such that it cannot decrease

$$D = \alpha_t^\beta D_t + \alpha_c^\beta D_c \quad \text{with} \quad \alpha_t + \alpha_c = 1, \quad \text{and} \quad \dot{D} \geq 0. \tag{B.4}$$

The parameter β improves the model response to shear dominated situations.

The damage functions for tension and compression D_t and D_c, are characterised by the parameters A_t, B_t, A_c and B_c, and have the following expression

$$D_j = \begin{cases} 0 & \text{if } \gamma\tilde{\varepsilon} \leq \varepsilon_{d0} \\ 1 - \frac{\varepsilon_{d0}(1-A_j)}{\gamma\tilde{\varepsilon}} - A_j \exp[B_j(\varepsilon_{d0} - \gamma\tilde{\varepsilon})] & \text{if } \gamma\tilde{\varepsilon} > \varepsilon_{d0} \end{cases} \qquad j = t, c \quad , \tag{B.5}$$

where ε_{d0} is the threshold strain above which damage occurs.

Finally, the tension balancing coefficient α_t is a ratio between a measure of the extension (positive) strains due to the tension (positive) stresses (the tension strains not due to Poisson's effect) and the equivalent strain

$$\alpha_t = \frac{\sum_i (\varepsilon_i^\dagger \varepsilon_i^{\dagger+})}{\sum_i (\varepsilon_i^\dagger)^2} \quad \text{with} \quad \varepsilon_i^{\dagger+} = \left\langle \frac{\mathbf{D}_e^{-1}}{(1-D)} :< \boldsymbol{\sigma} > \right\rangle, \tag{B.6}$$

where the stress tensor $\boldsymbol{\sigma}$ is expressed in its principal directions. The coefficient α_c is deduced from equation B.4.

The qualitative response of the model in the tension and the compression cases is presented in figure B.1. The figure shows clearly the asymmetry of the response on one side, and the unloading response of the model with no remanent strains on the other side.

B.2.2 Nonlocal formulation

The nonlocal regularisation can be applied to Mazars damage model. To do this, instead of taking $\tilde{\varepsilon}$ as the internal variable that controls damage evolution, a nonlocal quantity is considered. This nonlocal variable is an averaged equivalent strain $\bar{\varepsilon}(\mathbf{x})$ defined as

$$\bar{\varepsilon}(\mathbf{x}) = \frac{\int_\Omega \alpha(\|\mathbf{x}-\mathbf{y}\|)\ \tilde{\varepsilon}(\mathbf{y})\ d\Omega(\mathbf{y})}{\int_\Omega \alpha(\|\mathbf{x}-\mathbf{y}\|)\ d\Omega(\mathbf{y})}, \tag{B.7}$$

where Ω is the whole domain and α is a weighting function, in order to take into account a neighbourhood of the point $\mathbf{x}$. A Gaussian distribution can be taken as weighting function

$$\alpha(d) = \exp\left(-\left(\frac{2d}{l_c}\right)^2\right). \tag{B.8}$$

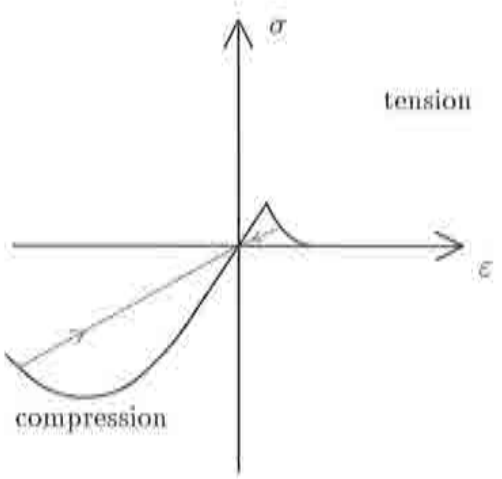

Figure B.1: Tension and compression response, and unloading branches

The length parameter l_c determines the size of the smallest region over which damage can localise. It can be chosen as a physical characteristic of the material (e.g. the size of heterogeneities in concrete), or as a purely numerical parameter.

B.3 Numerical examples

This section presents an adaptive process applied to a standard example (a three-point bending test on a notched beam, see [27]), using Mazars damage model with nonlocal regularisation. Figure B.2 defines the numerical experiment, indicating the beam geometry and the material parameters considered. The beam is simply supported.

The computations are made according to the plane stress assumptions. On the other hand, the load is applied by means of a distributed pressure, and an arc-length controlled nonlinear solver is employed in order to capture the softening behaviour. The fully nonlinear version of the error estimator is used, since tangent stiffness matrices are not readily available with the Mazars nonlocal damage model.

As expected, nonlocal regularisation leads to mesh objective numerical results. Figure B.3 shows a numerical solution, illustrating the failure response of the notched beam. The damage distribution, plotted in a uniform scale going from zero (bright grey) to one (dark grey), shows clearly the localised region, where the material is highly weakened. Consequently, the most part of the deformation concentrates in the notched section. The localised high tensile deformations correspond to the physical phenomenon of fracture. The boundary deformation illustrates this concentration, as well as the fact that the deflection of the beam is not distributed over its length. Finally, the load versus vertical displacement curve shows the softening response of the beam.

Figure B.4 presents an adaptive remeshing process considering Li-Bettess optimality

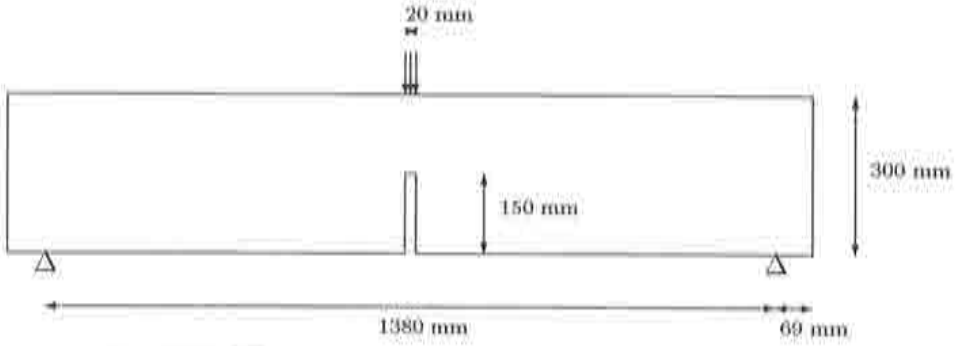

Material parameters: $E = 32300$ MPa $\nu = 0.2$ $A_t = 0.6$
$B_t = 3700$ $A_c = 1.1$ $B_c = 1000$
$\varepsilon_{d0} = 3 \cdot 10^{-5}$ $\beta = 1$ $l_c = 12$ mm

Figure B.2: Description of the numerical example: three point bending test on notched beam of 100 mm width, with maximum deflection of 0.3 mm

criterion and an acceptability criterion of 0.5%. On this occasion, point supports are considered. In the two first remeshing steps the elements concentrate in the damaged region, as expected, and the global error is considerably reduced. Thus, the process seems to run reasonably well. However, from this point on, the error is no longer reduced (it remains above 0.9%) despite the number of elements is importantly increased. Furthermore, very small elements appear in the neighbourhood of the supports. In fact, the process cannot converge to an acceptable error because of the singularities introduced by the point supports. In these points, where infinite stresses are found theoretically, large errors are detected. As a consequence, the mesh is refined and the numerical solution captures better the singular so-

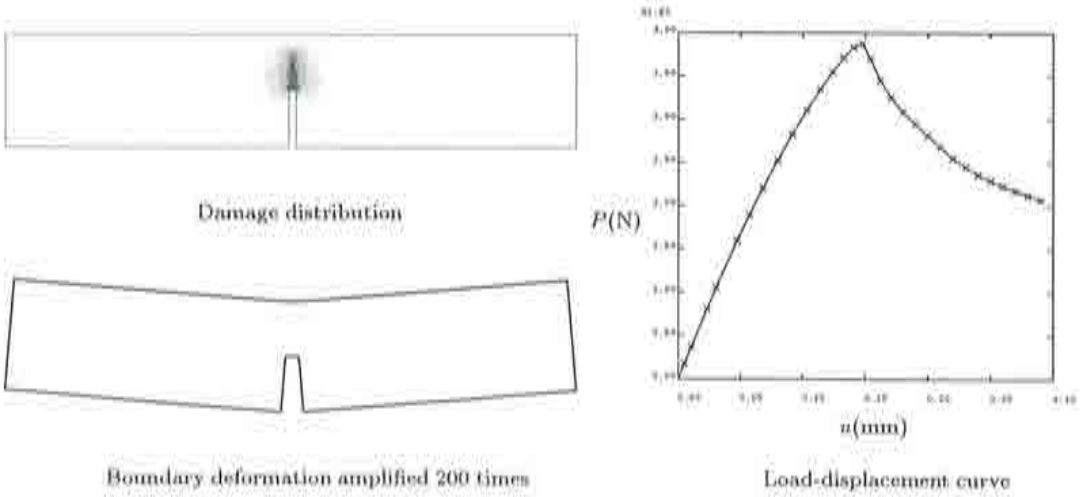

Figure B.3: Numerical solution of the problem

lution. However, the finer mesh also detects new errors, and the mesh is refined indefinitely without reducing significantly the estimated error.

Thus, the adaptive remeshing requires a more realistic modellisation of the problem in which no singularities appear. To do this, flexible supports distributed over 20 mm are considered in the remeshing process shown in figure B.5. In this case, two steps are enough to reach an acceptable approximation. The final mesh presents small elements in the damaged zone, but also in the neighbourhood of the supports. These zones are not damaged, but still present a certain concentration of stresses whose accurate approximation requires a rich discretisation. This also happens in the zone where the load is imposed.

In conclusion, the adaptive procedure based on error estimation can be applied to fracture localisation problems using Mazars nonlocal damage model. However, modellisations of the problem causing singularities in the solution can prevent the procedure from converging to an acceptable solution, and should consequently be avoided.

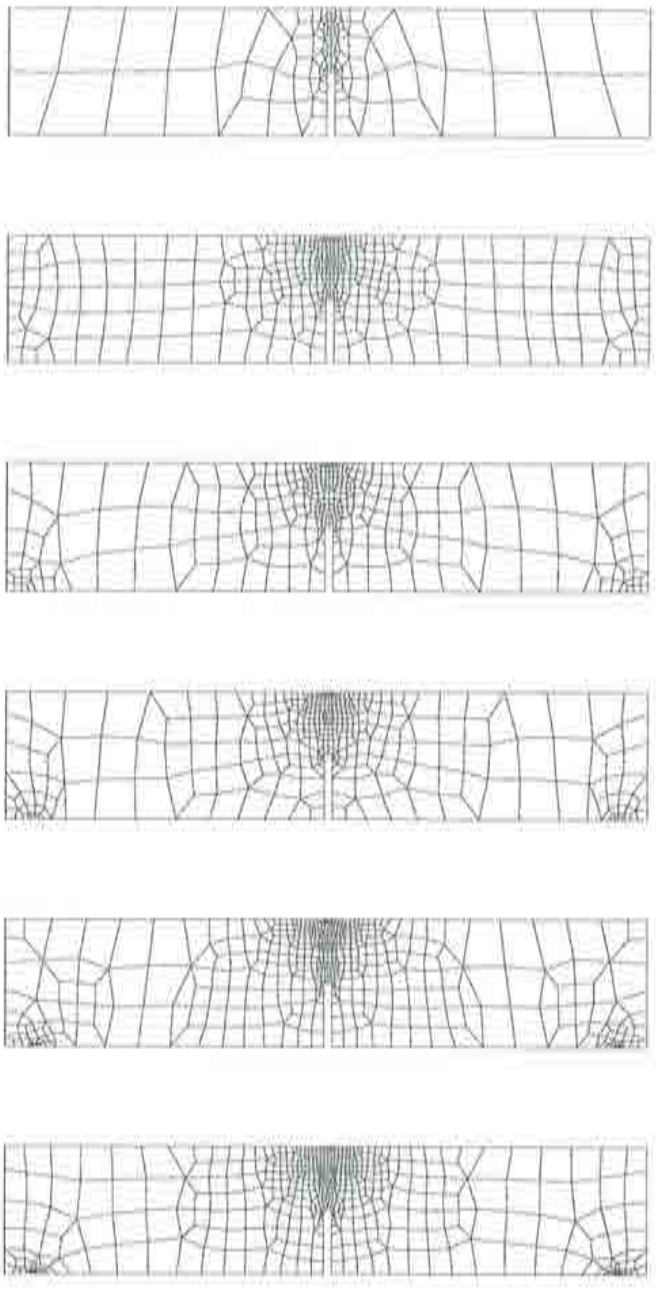

Figure B.4: Adaptive remeshing sequence in a problem with singularities

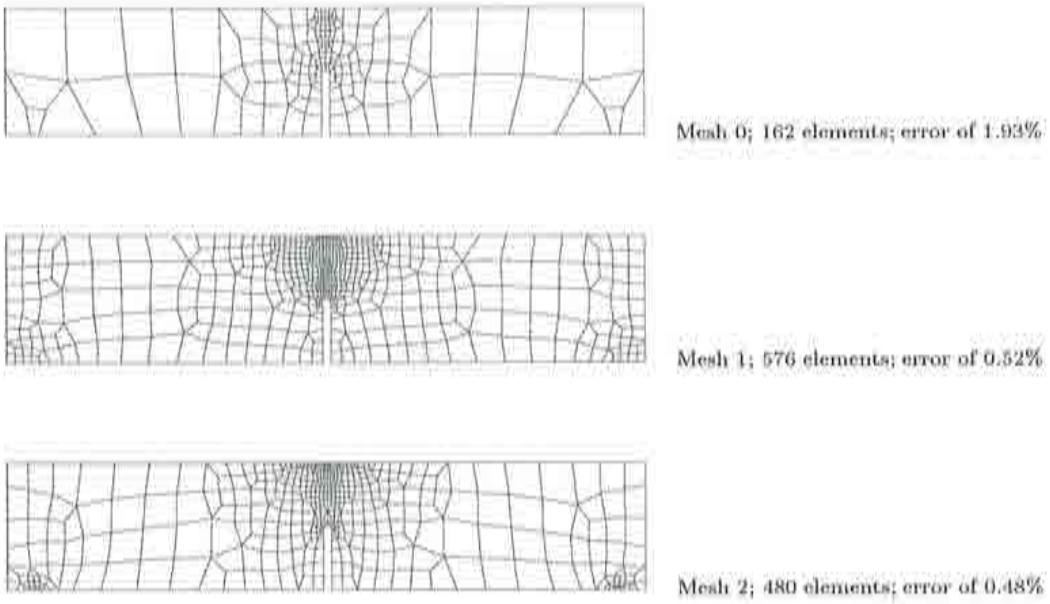

Figure B.5: Adaptive remeshing sequence in a problem without singularities

Bibliography

[1] M. Ainsworth and J.T. Oden (1993), 'A unified approach to a posteriori error estimation using element residual methods', *Numerische Mathematik*, **65**, 23-50.

[2] I. Babuška and C. Rheinboldt (1978), 'A-posteriori error estimates for the finite element method', *International Journal for Numerical Methods in Engineering*, **12**, 1597-1615.

[3] R.E. Bank and A. Weiser (1985), 'Some a posteriori error estimators for elliptic partial differential equations', *Mathematics of Computation*, **44**, 283-301.

[4] Z.P. Bažant and G. Pijaudier-Cabot (1988), 'Nonlocal continuum damage, localization instability and convergence', *Journal of Applied Mechanics*, **55**, 287-293.

[5] T. Belytschko, B. Moran and M. Kulkarni (1991), 'On the crucial role of imperfections in quasi-static viscoplastic solutions', *Journal of Applied Mechanics ASME*, **58**, 658-665.

[6] T. Belytschko and M. Tabbara (1993), 'H-adaptive finite element methods for dynamic problems, with emphasis on localization', *International Journal for Numerical Methods in Engineering*, **36**, 4245-4265.

[7] P.G. Ciarlet (1983), *Introduction à l'analyse numérique matricielle et à l'optimisation*, Masson, París.

[8] P. Díez (1996), *Un nuevo estimador de error para el método de los elementos finitos*, Doctoral Thesis, Universitat Politècnica de Catalunya, Barcelona.

[9] A. Deb, J. H. Prevost and B. Loret (1996), 'Adaptive meshing for dynamic strain localization', *Computer Methods in Applied Mechanics and Engineering*, **137**, 285-306.

[10] R. De Borst, H.B. Muhlhaus, J. Pamin and L.J. Sluys (1992), 'Computational modelling of localization of deformation', *Computational plasticity*, Eds. Owen, D.R.J. et al., Pineridge press, Part 1, 483-508.

[11] N. Higham (1996), *Accuracy and stability of numerical algorithms*, Society for Industrial and Applied Mathematics (SIAM), Philadelphia.

[12] P. Ladevèze, J.P. Pelle and Ph. Rougeot (1991), 'Error estimation and mesh optimization for classical finite elements', *Engineering Computations*, **8**, 69-80.

[13] D. Lasry and T. Belytschko (1988), 'Localization limiters in transient problems', *International Journal of Solids and Structures*, **24**(6), 581-597.

[14] L.Y. Li and P. Bettess (1995), 'Notes on mesh optimal criteria in adaptive finite element computations', *Communications in numerical methods in engineering*, **11**, 911-915.

[15] L.W. Malvern (1969), *Introduction to the Mechanics of a Continuous Medium*, Prentice-Hall Series in Engineering of the Physical Sciences, Englewood Cliffs, New Jersey, USA.

[16] A. Needleman (1988), 'Material rate dependence and mesh sensitivity in localization problems', *Computer Methods in Applied Mechanics and Engineering*, **67**, 69-85.

[17] J.T. Oden, L. Demkowicz, W. Rachowicz and T.A. Westermann (1989), 'Toward a universal *h-p* adaptive finite element strategy, part 2. A posteriori error estimation', *Computer Methods in Applied Mechanics and Engineering*, **77**, 113-180.

[18] E. Oñate and G. Bugeda (1993), 'A study of mesh optimality criteria in adaptive finite element analysis', *Engineering Computations*, **10**, 307-321.

[19] M. Ortiz and J.J. Quigley, IV (1991), 'Adaptive mesh refinement in strain localization problems', *Computer Methods in Applied Mechanics and Engineering*, **90**, 781-804.

[20] M. Pastor, J. Peraire and O. C. Zienkiewicz (1991), 'Adaptive remeshing for shear band localization problems', *Archives in Applied Mechanics*, **61**, 30-39.

[21] P. Pegon and A. Anthoine (1994), 'Numerical strategies for solving damage problems involving softening: application to the homogenization of masonry', Second International Conference on Computational Structures Technology, Athens.

[22] P. Perzyna (1966), 'Fundamental problems in viscoplasticity', *Recent Advances in Applied Mechanics*, Academic Press, New York, **9**, 243-377.

[23] G. Pijaudier-Cabot (1995), 'Non local damage', *Continuum models for materials with microstructure*, Edited by H.-B. Muhlhaus, John Wiley & Sons Ltd., 105-143.

[24] G. Pijaudier-Cabot, L. Bodé and A. Huerta (1995), 'Arbitrary Lagrangian-Eulerian finite element analysis of strain localization in transient problems', *International Journal for Numerical Methods in Engineering*, **38**, 4171-4191.

[25] P.M. Pinsky, M. Ortiz, and K.S. Pister (1983), 'Numerical Integration of Rate Constitutive Equations in Finite Deformation Analysis', *Computer Methods in Applied Mechanics and Engineering*, **40**, 137-158.

[26] J. R. Rice (1976), 'The localization of deformation', *Theoretical and Applied Mechanics*, W. T. Koiter, ed., North Holland Publishing Co., Amsterdam, The Netherlands.

[27] C. Saouridis and J. Mazars (1988), 'A multiscale approach to distributed damage and its usefulness for capturing structural size effect', CNRS-NSF Workshop *Strain localization and size effect due to cracking and damage*, E.N.S. Cachan, France.

[28] J. Sarrate (1996), *Modelización numérica de la interacción fluido-sólido rígido: desarrollo de algoritmos, generación de mallas y adaptividad*, Doctoral Thesis, Universitat Politècnica de Catalunya, Barcelona.

[29] J. C. Simó, J. Oliver and F. Armero (1993), 'An analysis of strong discontinuities induced by strain-softening in rate-independent inelastic solids', *Computational Mechanics*, **12**, 277-296.

[30] L.J. Sluys (1992), *Wave propagation, localisation and dispersion in softening solids*, Doctoral Thesis, Delft University of Technology.

[31] C. Truesdell (1953), Corrections and Additions to 'The Mechanical Foundations of Elasticity and Fluid Dynamics', *Journal of Rational Mechanics and Analysis*, **2**, 505-616.

[32] L.B. Wahlbin (1991), 'Local behavior in finite element methods' in P.G. Ciarlet & J.L. Lions (eds.) *Handbook of numerical analysis*, Vol. II, North-Holland, Amsterdam, 357-522.

[33] W.M. Wang, L.J. Sluys and R. De Borst (1996), 'Interaction between material length scale and imperfection size for localization phenomena in viscoplastic media', *European Journal of Mechanics, A/Solids*, **15**(3), 447-464.

[34] O.C. Zienkiewicz, and J.Z. Zhu (1987), 'A simple error estimator and adaptive procedure for practical engineering analysis', *International Journal for Numerical Methods in Engineering*, **24**, 337-357.

[35] O. C. Zienkiewicz and J.Z. Zhu (1987), 'A simple error estimator and adaptive procedure for practical engineering analysis', *International Journal for Numerical Methods in Engineering*, **24**, 337-357.

[36] O. C. Zienkiewicz and R. L. Taylor (1988), *The Finite Element Method*, **2**, McGraw-Hill Book Company, London, United Kingdom.

[37] O. C. Zienkiewicz and M. Huang (1990), 'A note on localization phenomena and adaptive Finite-Element analysis in forming processes', *Communications in Applied Numererical Methods*, **6**, 71-76.

[38] O. C. Zienkiewicz and J.Z. Zhu (1992), 'The superconvergent patch recovery (SPR) and adaptive finite element refinement', *Computer Methods in Applied Mechanics and Engineering*, **101**, 207-224.

[39] O. C. Zienkiewicz, M. Huang and M. Pastor (1995), 'Localization problems in plasticity using Finite Elements with adaptative remeshing', *International Journal of Numerical and Analytical Methods in Geomechanics*, **19**, 127-148.